UNIVERSIDAD DE GUANAJUATO

CAMPUS IRAPUATO - SALAMANCA
DIVISION DE INGENIERIAS

Experimental and numerical study of molten carbonate fuel cells working in reversible mode

THESIS

TO OBTAIN THE DEGREE OF:

DOCTOR IN MECHANICAL ENGINEERING

BY:

JUAN PEDRO PÉREZ TRUJILLO

DIRECTORS:

PhD FRANCISCO ELIZALDE BLANCAS
PhD STEPHEN JOHN MCPHAIL

SALAMANCA, GTO SEPTEMBER 2019

Experimental and numerical study of molten carbonate fuel cells working in reversible mode

by

Juan Pedro Pérez Trujillo

Commitee Members

1. **PhD Francisco Elizalde Blancas**, Supervisor (Mechanical Engineering Department, Universidad de Guanajuato)
2. **PhD Stephen J. McPhail**, Supervisor (DTE-PCU-SPCT, ENEA R.C. Casaccia, Italy)
3. **PhD María del Rosario Galindo González**, University Member (Chemical Engineering Department, Universidad de Guanajuato)
4. **PhD Massimiliano Della Pietra**, External Member (DTE-PCU-SPCT, ENEA R.C. Casaccia, Italy)
5. **PhD Sergio Cano Andrade**, University Member (Mechanical Engineering Department, Universidad de Guanajuato)
6. **PhD Alejandro Alatorre Ordaz**, University Member (Chemical Department, Universidad de Guanajuato)

ABSTRACT

Molten Carbonate Fuel Cells (MCFCs) have a great potential to help facing the global warming problem caused mainly by the increase in carbon dioxide. MCFCs have the characteristics that can be used as a fuel cell to produce electricity, can be used as a carbon capture and sequestration device helping to manage the carbon dioxide emissions, as well as an electrolyzer to produce hydrogen or synthesis gas using carbon dioxide and water as fuels.

The scope of this thesis is to test experimentally and predict numerically the performance of a single Molten Carbonate Fuel Cell working in reversible mode, i.e., the cell operates switching between fuel cell mode (Molten Carbonate Fuel Cell, MCFC) and electrolysis mode (Molten Carbonate Electrolysis Cell, MCEC), in order to obtain more knowledge for the conditions that increase the electrical power or hydrogen production, respectively.

Therefore, three experimental campaigns were carried out in order to study the performance of a single cell operating: 1) in fuel cell mode, 2) in reversible mode, switching between fuel cell and electrolysis mode, and 3) in electrolysis mode through a long-term test. The single cell tested has an electrode-electrolyte interface area of $80\,\mathrm{cm}^2$. The electrolyte used was an eutectic mixture of $(\mathrm{Li/K})_2\mathrm{CO}_3$ ($62/38\,\mathrm{mol}\,\%$).

In the first experimental campaign, the hydrogen content in the fuel electrode, the carbon dioxide content in the oxygen electrode and the cell temperature were varied to collect data, which help to compare the cell performance with five different zero-dimensional models. Then, one model was selected in order to fit with the experimental data in fuel cell mode.

During the second experimental campaign, the composition in the fuel electrode, the composition in the oxygen electrode, the electrodes flow ratio and the cell temperature were varied in reversible mode to collect data in both operative modes. The fitted model was then compared in electrolysis mode with the data acquired on the cell running in reversible mode. Some equations that determine the concentration overpotentials were included in order to improve the prediction of the limiting current density in electrolysis mode. The program code was written in Anaconda Python 3.7.

Finally, in the third experimental campaign, the cell was tested in electrolysis mode for almost 1000 h with the aim of studying the potential to operate the single cell as an electrolyzer.

”Strength does not come from winning. Your struggles develop your strengths. When you go through hardships and decide not to surrender, that is strength.”

—Mahatma Gandhi

ACKNOWLEDGMENTS

I would like to thank my advisor Dr. Francisco Elizalde Blancas and my co-advisor Dr. Stephen J. McPhail for trust on me, for their professional and personal advices and for giving me the opportunity to work with them and let me explode my capabilities enjoying this experience.

A very special thank to my mentor and friend Massimiliano Della Pietra, for his time and patience teaching and sharing me his knowledge on the lab. His invaluable support has been essential for the accomplishment of this work.

I also would like to thank all the hotlab members: Francesca Santoni, Davide Pumiglia, Carlos Boiguez Muñoz, Marco Graziadio and Andi Mehmeti for their warm welcoming since my first day in ENEA, their time, friendship and professional advices.

Special thanks to my committee members for their time dedicated on reviewing this thesis, which comments helped to improve the quality of this work.

I would like to express my most sincere gratitude to UG, CONACYT and ENEA for providing the financial support and the facilities that made possible the achievement of this research.

I would like to dedicate this thesis to my lovely wife Dulce Maria Silva Mosqueda, who always gives me her unconditional love and encourages me to improve constantly. Being my daily inspiration and support that makes possible reaching my goals. Thank you so much my sweetheart!

An last but not least, I would like to thank my friends and all my family with a special mention to my mom Juana Paz, for her great love and support towards the completion of this work.

Contents

List of Figures

List of Tables

1

Introduction

1.1. Global warming and future scenarios

Our planet is going through important alterations caused by the big increase in greenhouse gas (GHG) emissions produced by the increase in population as well as the excessive use of fossil fuels to maintain our current lifestyle. Carbon dioxide (CO_2) represents about 95 % of the energy-related emissions, and around 80 % of global anthropogenic GHG emissions [1]. CO_2 concentration has been increasing compared to the rather steady level of the pre-industrial era (about 280 ppm) up to concentrations of 413.5 ppm in 2019 [1, 2], as Figure 1.1 shows. One of the most evident effects of this CO_2 rise in the atmosphere is the global temperature anomaly (GTA) in comparison to the pre-industrial era, which nowadays GTA is 0.93 °C [2, 3]. Figure 1.2 shows the trend in GTA since pre-industrial era. GTA affects tremendously the equilibrium in our planet and it is related with diverse projected risks like forest fires, heat-related health impacts and extreme weather events [4].

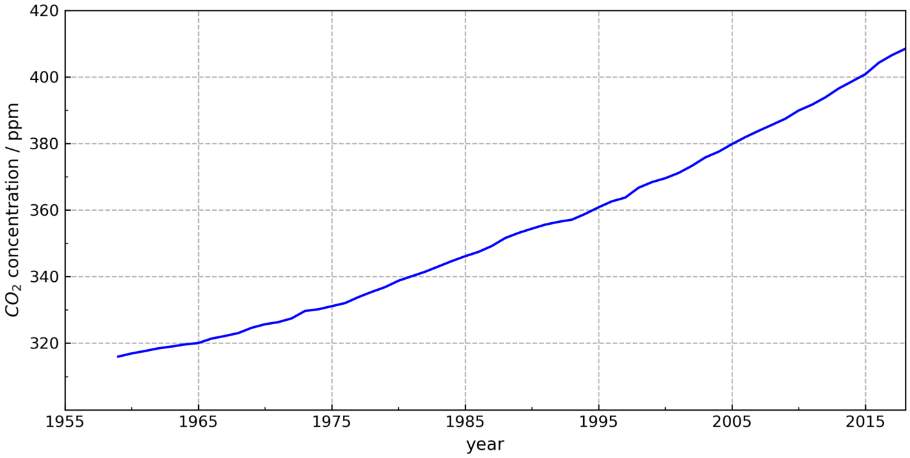

Figure 1.1. Carbon dioxide concentration in the atmosphere [2, 5].

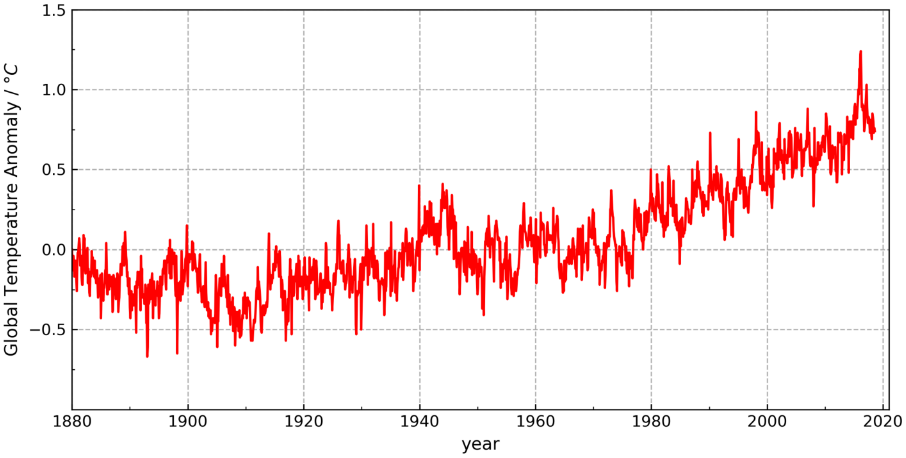

Figure 1.2. Global Temperature Anomaly [2,3].

Four projections of the GTA are shown in Figure 1.3 and described below:

a) without any plan following the actual trend with a final GTA of 4.2 °C.
b) with the implementation of the national plans agreed in the Paris 2015 Agreement and the Sustainable Development Goals with a final GTA of 3.3 °C.
c) new strategies to decrease the GHG emissions with a final GTA of 1.8 °C.
d) the most favorable scenario with a total decrease of the GHG emissions with a final GTA of 1.5 °C.

Nonetheless, it is still time to face this global ploblem mainly by the decrease of the global GHG emissions which will help to mitigate global warming by achieving large-scale reforestation, enhance energy efficiency, use of renewable energies, reduce industrial and agricultural emissions, and compensate the continuous CO_2 emissions by the development and implementation of economical CO_2 capture and storage technologies [6,7].

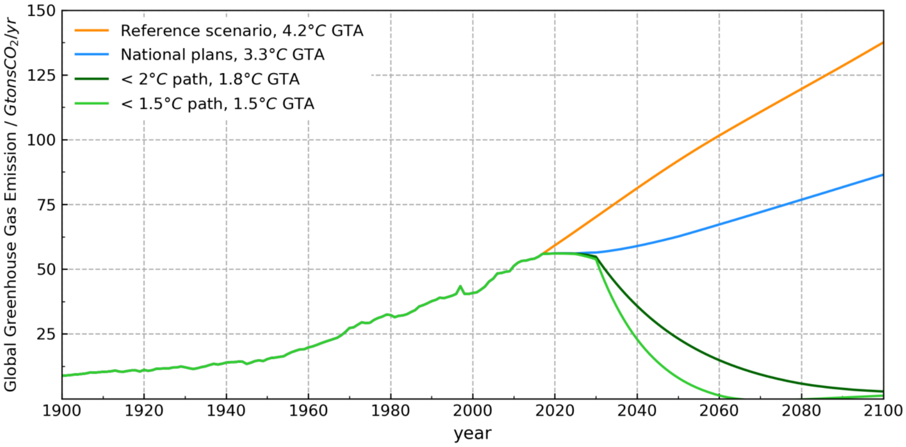

Figure 1.3. National Climate Plans and Additional Scenarios [2,8].

Most of these features can be integrated in smart or future energy networks that allow higher levels of interactions between the electrical, thermal and fuel grid. Besides, it is expected that the energy carrier for fuel grid in the future energy network is going to be hydrogen, which is produced from water via electrolyzers by consuming electricity. The electricity is supplied using renewable energy sources, however, it is difficult to integrate these in the electrical grid due to the intermittence and fluctuation of renewable energy resources, e.g. solar and wind [9]. Figure 1.4 shows a possible solution where an electrolyzer is used between the electrical grid and fuel grid to balance the demand and generation of electricity. The electricity from the renewable sources is sent to electrolyze water into hydrogen and oxygen [9].

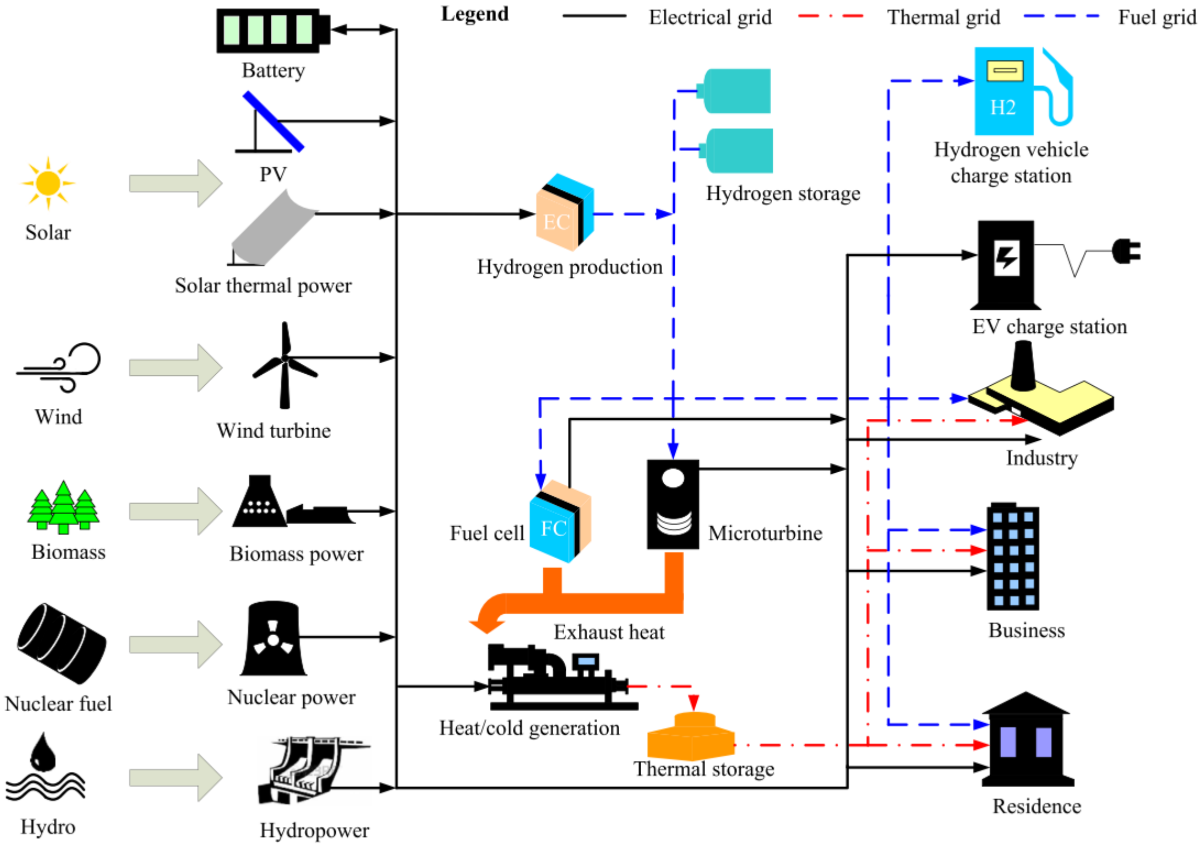

Figure 1.4. The electrical, thermal and fuel grid for future energy network (taken from [9]).

Alternatively, Carbon Capture and Sequestration/Storage (CCS) technologies represent an alternative to control the high CO_2 levels in the atmosphere. CCS technologies capture the CO_2 from large point sources, such as power plants, and it can be injected into geologic formations, such as depleted oil and gas fields, saline formations, and unmineable coal seams. This approach would lock up (sequester) the CO_2 for thousands of years [10,11]. Nonetheless, CO_2 can be utilized in a methanation process to produce CH_4 that can be utilized further for thermal and power applications [12,13] as Figure 1.4 and Figure 1.5 show. In this sense, fuel cells and electrolyzers are an important part in the design of future networks.

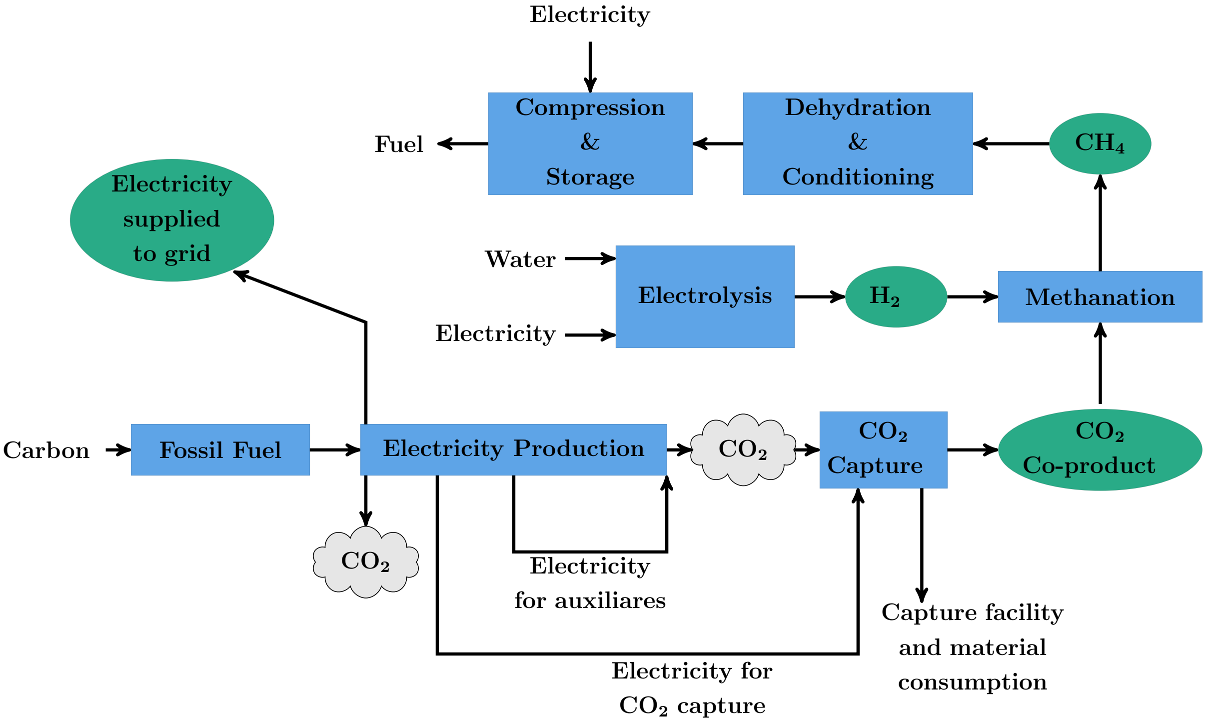

Figure 1.5. Power-to-Gas system with CO_2 from electricity production with CO_2 capture (adapted from [13]).

1.2. Fuel cell technology

The fuel cell was invented in 1839 by William Grove. Since Grove's invention, scientist, engineers, and businessmen have been working together to convert fuel cells into an affordable, low cost and clean energy device. However, the development of other technologies has delayed its market introduction, e.g. the internal combustion engine whose development attracts scientific interest. The first fuel cell used in a practical application was the alkaline fuel cell (AFC) developed by British scientist Sir Francis Bacon. Bacon's AFC technology was licensed by a US company, which developed it as the source of onboard power and drinking water for its Apollo lunar missions in 1962. A number of companies, in the United States and Europe, sprang into action and began developing terrestrial applications of AFCs. They produced a number of prototype AFC products, but were unable to bring them to the commercial market. They found AFCs to be unsuitable for terrestrial applications. Many companies abandoned AFC development by the 1970s [14].

In the mid-1970s, phosphoric acid fuel cells (PAFCs) became recognized as better suited for stationary, terrestrial applications. A number of US companies launched R&D of PAFCs after the US Government started to assist those companies by funding their R&D and demonstrations. By the mid-1980s, attention focused on molten carbonate fuel cells (MCFCs) and by the 1990s on solid oxide fuel cells (SOFCs). Besides, in the mid-1990s scientific interest focused on proton exchange membrane fuel cells (PEMFCs) managing to build an automobile powered by hydrogen-fueled PEMFCs [14].

PAFCs entered the market in the early 1990s as the ”fist generation” of fuel cell technology to be commercialized, however, a few hundred power plants were installed, but sales of most of them were completed with government and public subsidies. Subsequently, MCFCs arrived to the market as ”second generation” fuel cells in the early 2000. Similar to PAFCs, a small number of stationary power generation systems have been sold, also with subsidies. PEMFCs have been put on the commercial market recently covering applications as small stationary power plants, power source for material handling vehicles and emergency backup power systems. However, fuel cell researchers and developers are still struggling to develop reliable, durable, and inexpensive fuel cells that are competitive with conventional power generation technologies [14].

1.2.1. Fuel cell classification

According to the classification of fuel cells, these can be divided by the type of electrolyte used in the cell. The electrolyte can be aqueous, solid, or molten; alkaline, neutral, or acid; or polymer, chemical substance, or ceramic. The choice of the electrolyte determines the temperature range in which the fuel cell operates, aside from the type of material used in the fuel cell. Low temperature fuel cells usually have slow chemical reactions and require rare and precious metal platinum catalyst at the fuel electrode or the oxygen electrode or both to speed up the reaction. Higher temperatures typically promote faster reactions, and requirements for catalysis are lessened. The operating temperatures also impact the type of fuel that is used. In low temperature fuel cells, gaseous fuel must be converted to hydrogen prior to entering the fuel cell. In high temperature fuel cells, hydrocarbon fuels can be internally converted to hydrogen or even directly oxidized electrochemically [14]. There are five types of fuel cells currently under development including:

1. Proton exchange membrane fuel cells (PEMFCs)
2. Alkaline fuel cells (AFCs)
3. Phosphoric acid fuel cells (PAFCs)
4. Molten carbonate fuel cells (MCFCs)
5. Solid oxide fuel cels (SOFCs)

Table 1.1 provides a summary of the characteristics of the different types of fuel cells. [14–16]

Table 1.1. Comparison of Fuel Cell Technologies [14,15].

Fuel cell type	**Common electrolyte**	**Operating temperature**	**Typical stack size**	**Efficiency**	**Applications**	**Advantages**	**Disadvantages**
Polymer electrolyte membrane (PEM)	Porfluoro sulfonic acid	<120 °C, typically 80 °C	<1 kW to 100 kW	60 % direct H_2 ; 40 % reformed fuel	a) Backup power; b) Portable power; c) Distributed generation; d) Transportation; e) Specialty vehicles	a) Solid electrolyte reduces corrosion and electrolyte management problems; b) Low temperature; c) Quick start-up and load following	a) Expensive catalyst; b) Sensitive to fuel impurities; c) Low temperature waste heat
Alkaline (AFC)	Aqueous solution of potassium hydroxide soaked in a matrix, or alkaline polymer membrane	<100 °C	1 kW to 100 kW	60 %	a) Military; b) Space; c) Backup power; d) Transportation	a) Oxygen electrode reaction faster in alkaline electrolyte, leads to high performance; b) Low cost components; c) Quick start-up	a) Sensitive to CO_2 in fuel and air; b) Electrolyte management (aqueous); c) Electrolyte conductivity (polymer)

Phosphoric acid (PAFC)	Phosphoric acid soaked in a matrix or imbibed in a polymer membrane	150 °C to 200 °C	5 kW to 400 kW, 100 kW module (liquid PAFC); <10 kW(polymer membrane)	40 %	a) Distributed generation	a) Suitable for Combined Heat and Power (CHP); b) Increased tolerance to fuel impurities	a) Expensive catalyst; b) Long start-up time; c) Low current and power; d) Sulfur sensitivity
Molten Carbonate (MCFC)	Molten lithium, sodium, and/or potassium carbonates, soaked in a porous matrix	600 °C to 700 °C	300 kW - 3 MW, 300 kW module	50 %	a) Electric utility; b) Distributed generation	a) High efficiency; b) Fuel flexibility; c) Can use a variety of catalysts; d) Suitable for CHP; e) Hybrid/gas turbine cycle	a) High temperature corrosion and breakdown of cell components; b) Long start-up time; c) Low power density
Solid oxide (SOFC)	Ytria stabilized zirconia	500 °C to 1000 °C	1 kW to 2 MW	60 %	a) Auxiliary power; b) Electric utility; c) Distributed generation	a) High efficiency; b) Fuel flexibility; c) Solid electrolyte; d) Suitable for CHP & CHHP; e) Hybrid / gas turbine cycle	a) High temperature corrosion and breakdown of cell components; b) Long start-up time; c) Limited number of shut downs

1.3. Molten Carbonate Fuel Cell overview

The concept of MCFCs dates back to the 1950s when Dutch scientists G. H. J. Broers and J. A. A. Ketelaar began their fuel cell research at the University of Amsterdam. They reported that their first MCFC prototype operated continuously for 6 months with an electrolyte made of an alkali metal carbonate impregnated in a disk of magnesium oxide. Nevertheless, Broers and Ketelaar's work was stopped in 1969 because the industry lacked interest and the technology competed poorly with conventional power and nuclear power. However, impressed with the Dutch research, the US Army funded MCFC development from the mid-1960s to the late 1960s, finalizing the support by the lack of positive results. After that, the US Department of Energy started showing interest in MCFC technology in the mid-1970s and funded the development and demonstration of MCFC power plants. US funding for MCFC development continued for nearly 25 years until 2000 [14, 17–20]

Along with the United States, Japan became the most active player in MCFC development. In 1981, Japan's Ministry of Economy, Trade, and Industry (METI) implemented a 24-year, MCFC development program under the Moonlight Project that continued until 2004, with a total budget of about $470 million. The ultimate goal of the program was to develop large-scale MCFC power plants that could be fueled by coal gas and replace coal-burning thermal power plants [14]. European countries revived their interest in MCFC technology in the mid- to late 1980s. The Netherlands and Italy started their MCFC development efforts in 1986, and Germany in 1988. However, the European efforts were of lesser intensity compared to those of the United States and Japan. Nonetheless, the European Union (EU) also played a major role in supporting MCFC development and demonstration efforts. Elsewhere in the world, the only other major actor was South Korea, which started its MCFC development in 1993. Again, the government was more interested in acquiring global state-of-the-art technology via licensing and corporate participating with the global MCFC leader, Fuel Cell Energy (FCE) of the United States [14].

MCFCs still have a number of serious technical challenges. In particular, MCFCs suffer from short service life and high costs. The main challenge for MCFCs stems from the very corrosive and mobile electrolyte, which requires use of nickel and high-grade stainless steel for the cell components [21–23]. Besides, the higher temperatures promote material problems, impacting mechanical stability and stack life. In addition, throughout the lifetime of MCFCs, a slow but steady loss of electrolyte occurs, which tends to cause gradual performance decay [24]. Dissolution of the oxygen electrode also is the primary life-limiting constraint of MCFCs. The current state-of-the-art oxgyen electrode, nickel oxide (NiO), slowly dissolves into the electrolyte, creating metal particles that precipitate across the electrolyte tile, a porous form of lithium aluminate filled with a molten carbonate electrolyte, eventually leading to fuel electrode - oxygen electrode shorting. The mechanism by which NiO dissolves into the electrolyte is not fully understood. Furthermore, a source of CO_2 is required at the oxygen electrode to form the carbonate ion, which requires additional Balance of Plant (BoP) components. To be commercially successful, MCFCs need to meet longevity requirements of at least 40 000 h as well as cost reduction. Since the mid-1970s, the materials for the electrodes and electrolyte have remained essentially unchanged [14, 17].

1.4. Integration of Fuel Cells in Power-to-Gas systems

Renewable energies (e.g. wind) have the characteristic to be intermittent because they are dependent on weather conditions. This makes integration with current power networks a challenge in terms of matching fuel/energy source, generation, transmission, distribution and customer-side requirements. To cover these requirements some Energy Storage Systems (ESS) have been proposed, which include pumped hydro storage, compressed-air storage, battery energy storage, superconducting magnetic energy storage, thermal energy storage and chemical energy storage technologies [25]. A review of the different energy storage technologies and information on the real life applications, their differences and unique features helping in determining the best energy storage technology are given by Aneke and Wang [25].

Concerning chemical energy storage technology, fuel cells working in electrolysis mode play an important role because they can be integrated in a Power-to-Gas (PtG) system to convert surplus electricity coming from a renewable source into gaseous energy carriers, mainly hydrogen and methane that can be transformed back into electricity [9, 13, 26]. Robinus et al. [27] analyze the potential use of a PtG system using an alkaline electrolyzer in the electrical distribution grid as an alternative to a network expansion with cables, focusing on determining the size of the electrolyzer to cover a specific demand, the effect on the voltage grid by the installation of the electrolyzer and the economic feasibility of the system. The results indicate that laying a cable represents around 30 % of the investment and the rest, the electrolyzer cost. In the case that a PtG system is dedicated mainly to the production of hydrogen, this should meet the requirements of the potential consumers. The pressure level and the purity of hydrogen are substantial elements to achieve this goal, where auxiliary equipment is needed to increase the pressure of the gases and clean the hydrogen to desired levels. Bensmann et al. [28] study numerically two configurations of a PtG system using a Proton Exchange Membrane (PEM) electrolyzer unit with auxiliary devices including a multistage compressor, two cooler units and a dryer unit. The hydrogen delivery pressure analyzed was between 1 bar to 100 bar, presenting the energy demand by the process depending on the electrolyzer pressure for different delivery pressures. The results show that the energy demand for drying dominates the total energy balance at low delivery pressure, besides, higher electrolyzer pressures increase the losses due to hydrogen crossover.

PtG is a promising technology, nevertheless, it has many system variations, and their environmental performance needs to be evaluated and compared with conventional technologies. Zhang et al. [13] investigate the environmental performance of a PtG system using Life Cycle Assessment (LCA), covering aspects including supply of electricity, product gases (hydrogen and methane), the use of CO_2 Capture and Utilization (CCU) obtained by different sources, the comparison with conventional technologies, and the investigation of further environmental impacts of PtG in addition to the impact of global warming potential. The analysis varies the used electrolyzer considering an alkaline electrolyzer and a PEM electrolyzer. The results of system variations show that PtG can, depending on electricity supply and CO_2 source, reduce GHG emission compared to conventional gas production technologies.

Among electrolyzers, the most mature and commercial is the Alkaline electrolyzer [29,30], followed by the Proton Exchange Membrane (PEM) electrolyzer [29]. The capital costs for alkaline and PEM electrolyzer systems are presented in [27, 31]. Solid Oxide Electrolyzers (SOECs) are in laboratory stage, however, they have been greatly advanced in the last years related to experimental and numerical aspects. Menon et al. [32] carried out a parametric analysis of the principal variables affecting the performance of a SOEC using a quasi-two-dimensional model. The thermoneutral voltage has been found using an isothermal analysis. This result is important in order to maximize efficiency, via conscious choice of optimum design for steam electrolysis systems. Klotz et al. [33] use a zero-dimensional model, previously developed by Leonide et al. [34] to predict the performance of Solid Oxide Fuel Cells (SOFC), to simulate the behavior of small and large area cells in SOFC and SOEC mode. Ferrero et al. [35] studied experimentally and numerically reversible solid oxide cells. Two commercial nickel/zirconia cermet (Ni/YSZ) supported planar solid oxide cells with the air electrode made by either lanthanum strontium manganite/zirconia (LSM/YSZ) or lanthanum strontium cobalt ferrite (LSCF) were characterized. The numerical model was divided into two parts: the first one characterizes the electrochemical process and mass transport of gaseous species at the electrodes, the second one takes results from the previous calculations to determine the heat transfer in the system. Kazempoor and Braun [36] performed a parametric analysis to investigate the effect of various operating parameters related to SOEC electrochemical performance, as well as hydrogen and syngas production. Some of the results indicate that carbon dioxide plays an important role increasing the electrochemical losses at higher CO_2 concentrations. Luo et al. [37] carried out an exergy analysis to compare three methane production systems including 1) water electrolysis + Sabatier reactor, 2) water/carbon dioxide co-electrolysis + methanation reactor (MR) , and 3) a single SOEC-MR. Moreover, a comparison of SOEC, proton exchange membrane electrolysis cell and an alkaline electrolysis cell is performed. The results obtained show that SOEC presents a higher efficiency. Besides, according to the methane production systems the single SOEC-MR presents the highest efficiency. Mehran et al. [38] tested a fabricated solid oxide cell at various high-pressure conditions to determine the electrochemical and syngas production characteristics. The cell was operated between 1 bar and 8 bar at 800 °C in both fuel cell and co-electrolysis mode. The results show that increasing the pressure a higher performance can be obtained; the ohmic and activation polarizations are slightly lower in electrolysis mode and increasing the pressure these polarizations are diminished.

Molten Carbonate Fuel Cells (MCFCs) as well as Solid Oxide Fuel Cells (SOFCs), are high-temperature technologies that can operate in reversible mode to convert surplus electricity into a gas rich in hydrogen, and when required back into electricity. Additionally, working in fuel cell mode, MCFCs can be used to separate and re-use CO_2 [39–41], this fact results interesting because they can be coupled to future energy networks and PtG technologies helping to decrease the GHG emissions, Figure 1.4 and Figure 1.5, respectively,.

However, Molten Carbonate Electrolysis Cells (MCECs), unlike SOECs, have been little studied, and these studies have been conducted only at small-size level, i.e., limited only to lab-scale experiments using button cells like Hu et al. [42–46]. In [42], they carried out an experimental investigation on the performance of molten carbonate cells in both fuel cell and electrolysis mode reporting polarization curves and electrochemical impedance spectroscopy using button cells with a geometrical electrode area of $3\,\mathrm{cm}^2$. Standard mixtures consisting of 64/16/20% $H_2/CO_2/H_2O$ mole fraction and 15/30/55% $O_2/CO_2/N_2$ mole fraction were used for the fuel electrode and the oxygen electrode, respectively, in order to study different operating conditions. The results show that the cell exhibited better electrochemical performance in MCEC mode than in MCFC mode; besides the fuel electrode showed higher polarization loss in electrolysis cell mode than in fuel cell mode. The electrode kinetics of the Ni and NiO porous electrode for hydrogen production in a MCEC were studied in [43] and [44], respectively, obtaining a dependency of the exchange current density on hydrogen, carbon dioxide and water partial pressures for the fuel electrode, besides, the exchange current density on oxygen and carbon dioxide partial pressure for the oxygen electrode. Another work involved the evaluation of the performance of the nickel electrode with hydrogen-lean gases in MCEC mode, i.e. 1 % [45], indicating that charge-transfer polarization increased compared to the reference condition. Finally, performance and durability tests of the MCEC and the reversible MCFC were performed for 2165 h and 1019 h, respectively [46]. The cells presented a small degradation at the end of the durability test of the MCEC, contrary for the case of reversible MCFC that present an improvement at the end of the test.

Thus, it is necessary to increase the knowledge in the reversible operation mode of molten carbonate cell, focused more on electrolysis mode that has been poorly investigated.

1.5. Hypothesis

The operation of an MCFC in reversible mode could help to increase the operative life of this kind of cells by delaying the electrolyte loss and operating an MCFC in reverse mode to produce hydrogen could be technically feasible as other hydrogen production technologies.

1.6. Aim of the thesis

The aim of this thesis is to test experimentally and predict numerically the performance of a single Molten Carbonate Fuel Cell working in reversible mode, i.e., the cell operates switching between fuel cell mode (Molten Carbonate Fuel Cell, MCFC) and electrolysis mode (Molten Carbonate Electrolysis Cell, MCEC), in order to obtain more knowledge for the conditions that increase the electrical power or hydrogen production, respectively.

There are some specific objectives which are described below that are being proposed to reach the aim of this work.

1. To test experimentally a single MCFC cell operating only in fuel cell mode in order to obtain experimental data which allow the evaluation and comparison of some MCFC zero-dimensional models as well as to identify the model that fits better with the experimental data and then evaluate its applicability in electrolysis mode.
2. To test experimentally a single MCFC cell operating in reversible mode in order to study the effect of different operative parameters on the cell performance when it changes between fuel cell and electrolysis mode.
3. To validate the zero-dimensional model of the cell operating in reversible mode with the experimental data acquired from the single MCFC tested.
4. To evaluate numerically and experimentally the effect of water and carbon dioxide reduction on the performance of the cell operating in reverse mode.
5. To carry out an endurance performance test of a single MCFC operating in reverse mode in order to determine its feasibility to produce hydrogen as well as its stability operating as electrolyzer.

2

Molten Carbonate Fuel Cell Features

2.1. Main components

MCFC is the only one, among all the hydrogen-oxygen fuel cells, which employs a molten salt electrolyte, compound of lithium, sodium and/or potassium, that decreases the contact resistance and improves the gas sealing [47], also is the one with the thickest electrolyte, this fact helps to decrease the NiO dissolution phenomena [47–49], besides, improving the structural resistance. Figure 2.1 shows the thickness of electrode and electrolytes for various fuel cells. To melt the electrolyte the cell requires to operate over 500 °C, commonly between 600 °C and 700 °C [47, 48].

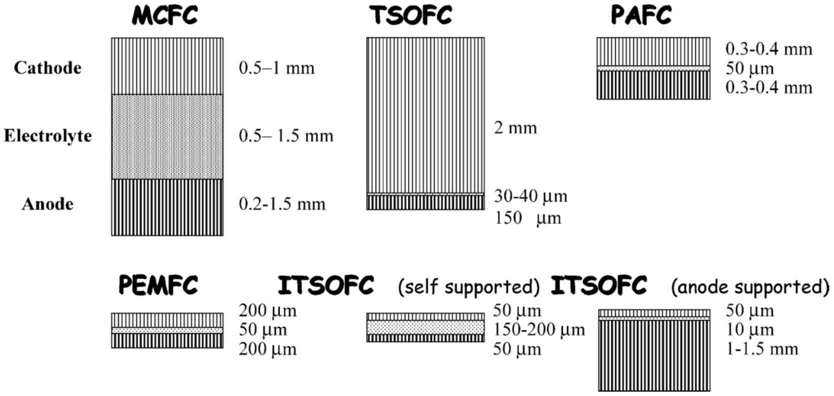

Figure 2.1. Thickness of electrodes and electrolytes for various fuel cells [47].

A Molten Carbonate Fuel Cell operated in reverse mode to produce fuel gas, e.g., hydrogen or syngas, is named Molten Carbonate Electrolysis Cell (MCEC). The only difference between MCEC and MCFC is the direction of current, since the principle of operation for the electrolyzer is the inverse of fuel cell [50]. An electrolyzer is a device that produces hydrogen by water splitting that requires the addition of electricity and depending of the operation the addition of heat, and represents a crucial link towards achieving a hydrogen economy. Its principal components are fuel electrode, oxygen electrode, electrolyte and current collectors. Regarding MCEC, its components are made of the same materials as those used to manufacture an MCFC, where the fuel electrode is fabricated of porous nickel and alloyed with Cr and/or Al, whereas the oxygen electrode is fabricated of porous lithiated nickel oxide. The electrolyte in the MCFC consists of an eutectic mixture of the combination of lithium, potassium and/or sodium carbonate, which remains liquid at the operating temperature. A porous matrix, commonly fabricated of $\gamma - \mathrm{LiAlO_2}$, is used to retain the electrolyte, besides, conducting the carbonate ions between the electrodes as well as separating the fuel and oxidant gases [47,49]. Below, there are presented some requirements that fuel electrode, oxygen electrode and current collector should have to support the operating conditions in an MCFC.

1. **Fuel electrode**. The fuel electrode is required to have high corrosion resistance for melted carbonate under the fuel gas atmosphere. It also should be stable under steam and CO_2 generated at the fuel electrode. Besides, the fuel electrode should be resistant to the interstitial action of hydrogen. Moreover, chrome and aluminum, etc., are usually added for the improvement of creep resistivity at high temperatures [51,52].
2. **Oxygen electrode**. The oxygen electrode is operated under severe conditions of an oxidative atmosphere, and thus the metallic oxide is used. Typically, the porous media made of oxidized nickel particles is used. Nickel oxide does not have sufficient electric conductivity; however, the electric conductivity is given by lithium in molten carbonate being doped in the oxygen electrode [51,52].
3. **Current collector**. The current collector is placed within the gas flow channel for improvement of the electric contact. Perforated metal plates are generally used [51].

2.2. Reactions involved in Molten Carbonate Fuel Cells

The electrochemical reactions occurring in MCFCs electrodes are the oxidation and reduction reactions, as is shown in Figure 2.2.

The reduction reaction occurs at the oxygen electrode. In this case, the carbon dioxide and oxygen are reduced forming the carbonate ions. The formed ions travel through the electrolyte to the fuel electrode. The reaction is defined as:

$$\mathrm{CO_2} + \frac{1}{2}\,\mathrm{O_2} + 2\,\mathrm{e^-} \longrightarrow \mathrm{CO_3^{2-}} \tag{2.1}$$

On the other hand, the oxidation reaction occurs in the fuel electrode. If the fuel is hydrogen, it reacts with the carbonate ions coming from the oxygen electrode to form steam and carbon dioxide as products. The oxidation reaction is defined as:

$$H_2 + CO_3^{2-} \longrightarrow H_2O + CO_2 + 2\,e^- \tag{2.2}$$

However, carbon monoxide can oxidize if it is present in the fuel electrode as shown in the following reaction in Eq. (2.3) [53]:

$$CO + CO_3^{2-} \longrightarrow 2\,CO_2 + 2\,e^- \tag{2.3}$$

Nevertheless, in literature it is claimed that the most likely way for carbon monoxide to be utilized is through the shift reaction [54].

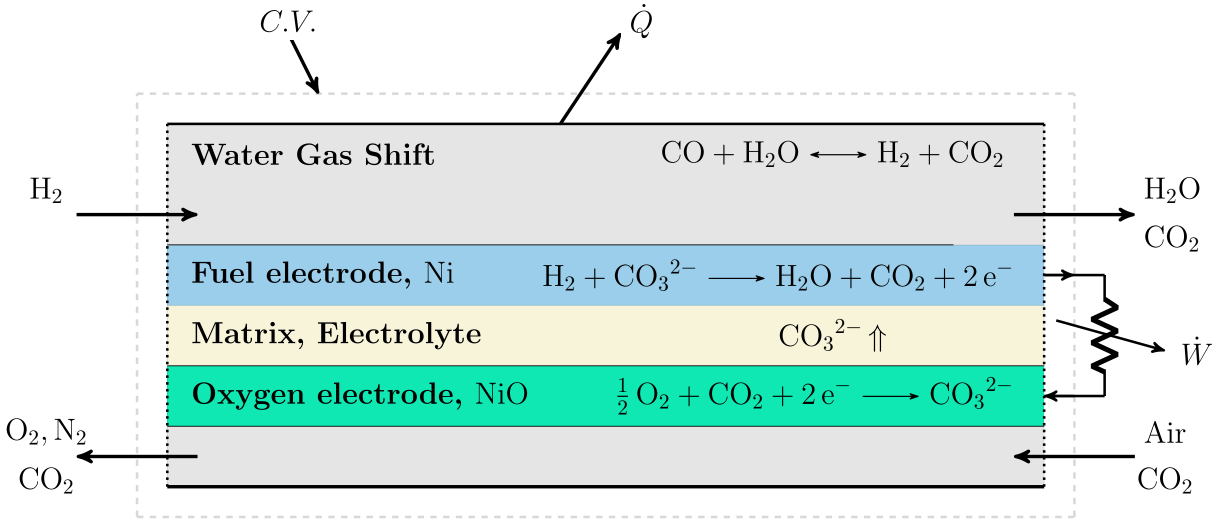

Figure 2.2. Reactions occurring inside an MCFC.

The electrons are discharged from the fuel electrode and taken into the oxygen electrode through an external circuit in a series of reaction. Moreover, power and heat generation by the fuel cell are achieved by the reactions involved and electrons flowing. Thus, the global reaction is

$$H_2 + \frac{1}{2} O_2 + CO_{2,oe} \longrightarrow H_2O + CO_{2,fe} \tag{2.4}$$

showing that carbon dioxide is being produced in the fuel electrode.

If steam reforming takes place in the fuel electrode, two more reactions need to be considered:

a) steam reforming occurs when methane reacts with water to form hydrogen and carbon monoxide.

$$CH_4 + H_2O \longrightarrow CO + 3\,H_2 \tag{2.5}$$

b) water gas shift reaction occurs when carbon monoxide reacts with water to form hydrogen and carbon dioxide.

$$CO + H_2O \longrightarrow CO_2 + H_2 \tag{2.6}$$

2.3. Reactions involved in Molten Carbonate Electrolysis Cell

Figure 2.3 presents the primary components and reactions occurring inside an MCEC.

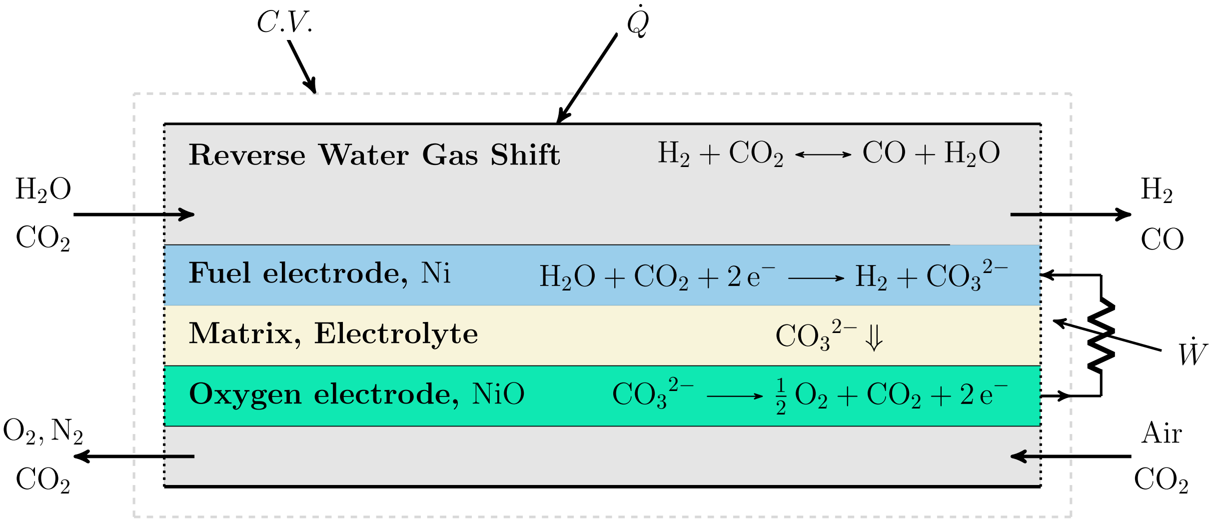

Figure 2.3. Reactions occurring inside an MCEC.

Water, carbon dioxide, heat and electricity are required to perform the reduction reaction in the fuel electrode, producing H_2 and carbonate ions (CO_3^{2-}). The reduction reaction is expressed as:

$$H_2O + CO_2 + 2\,e^- \longrightarrow H_2 + CO_3^{2-} \tag{2.7}$$

The carbonate ions are conducted through the electrolyte to be oxidized at the oxygen electrode, producing carbon dioxide and oxygen. No flow is strictly required at the oxygen electrode inlet; nevertheless, some flow, air mixed with a little amount of carbon dioxide, is supplied to sweep out the formed gases, besides, avoiding degradation of the electrode. The oxidation reaction is stated as:

$$CO_3^{2-} \longrightarrow CO_2 + \frac{1}{2}O_2 + 2\,e^- \tag{2.8}$$

Contrary to a fuel cell, electricity and heat are required to split the water and/or CO_2 in the fuel electrode. Thus, the global reaction is

$$H_2O + CO_{2,\mathrm{fe}} \longrightarrow H_2 + \frac{1}{2}\,O_2 + CO_{2,\mathrm{oe}} \tag{2.9}$$

The molar flow-rate of hydrogen produced by Eq. (2.7) is determined by the reaction rate of the cell. It depends on the current demanded and the number of electrons involved in the reaction, n_e, as Eq. (2.10) shows.

$$\dot{n}_{\mathrm{H_2}} = \frac{I}{n_e\mathbf{F}} \tag{2.10}$$

2.4. Voltage in the Molten Carbonate Cells operating in reversible mode

The electrical power in the system is a function of voltage and current. The voltage depends on the composition of the gases, the current density, the operating temperature and pressure. Thus, operating the system under a certain electric current, the voltage would change depending on the electrical overpotentials present in the system that include ohmic, activation and concentration losses, all of them described in detail in section 2.5. Hence, the system voltage is predicted, adding (in electrolysis mode) or subtracting (in fuel cell mode) the electrical overpotentials from the ideal voltage, also named Nernst voltage, Eq. (2.11).

$$V_m = V_{Nernst} \pm j\left(R_{ohm} + R_{act,oe} + R_{act,fe} + R_{conc,fe} + R_{conc,oe}\right) \tag{2.11}$$

The Nernst voltage is a function of temperature, pressure, and molar fractions of gases, evaluated at equilibrium. Since no specific mode of operation is occurring at open circuit, the Nernst voltage is determined indistinctly for fuel cell or electrolyzer mode as Eq. (2.12) states [55, 56].

$$V_{Nernst} = E^0 - \frac{\mathbf{R}T}{n_e\mathbf{F}} \ln\left[\frac{y_{\mathrm{H_2O,\,fe}}}{y_{\mathrm{H_2,\,fe}}{y_{\mathrm{O_2,\,oe}}}^{1/2}} \frac{y_{\mathrm{CO_2,\,fe}}}{y_{\mathrm{CO_2,\,oe}}} \left(\frac{p_{ref}}{p}\right)^{1/2}\right] \tag{2.12}$$

Where the standard voltage, E^0, can be determined as a function of the standard Gibbs free energy variation of the global electrochemical reaction at the cell operating temperature [55].

$$E^0 = \frac{\Delta\bar{g}^o}{n_e\mathbf{F}} \tag{2.13}$$

If the Nernst potential is evaluated using the feeding gas molar fractions, the actual Nernst voltage in Eq. (2.11) has to be penalized also taking into account the losses due to the gas conversion which occurs inside the cell and changes the gas composition. Figure 2.4 shows the voltage losses of a cell operating in reversible mode.

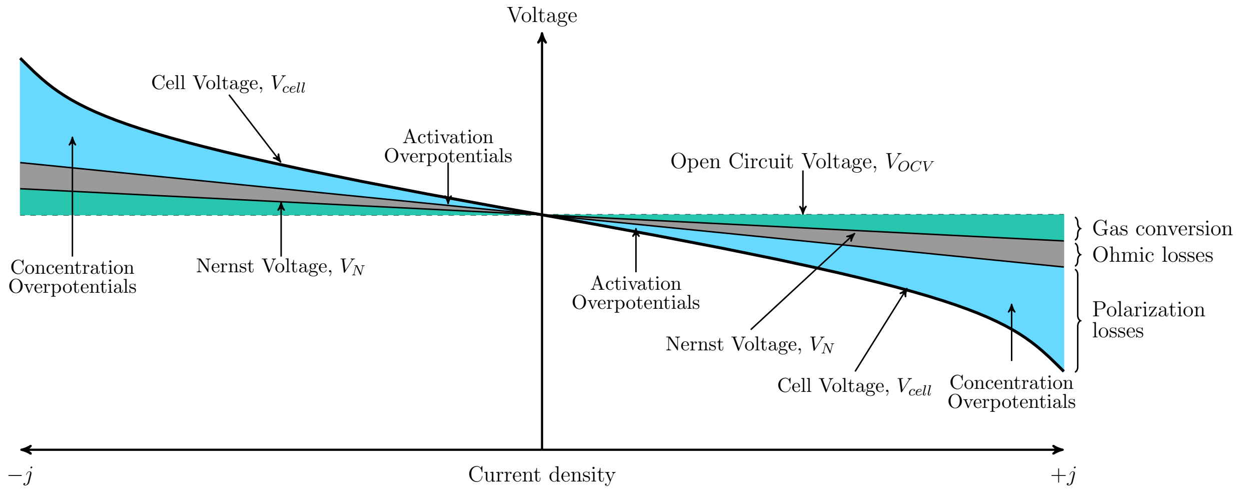

Figure 2.4. Voltage losses of a cell working in reversible mode.

2.5. Zero-dimensional models to determine voltage losses in MCFC

There are some zero-dimensional models which have been proposed to determine the voltage losses shown in Eq. (2.11), which are presented and explained in detail in this section.

2.5.1. Model 1

This model was proposed and developed by the Central Research Institute of Electric Power Industry (CRIEPI) research group in Japan using single cells [57]. This electrochemical model considers that simultaneous diffusion of superoxide ($O_2{}^-$) and CO_2 is the dominant feature of mass transport associated with oxygen reduction. The model was continuously improved by the research group; thus, four sub-models are presented. In general, the overpotentials prediction for this model in the fuel electrode is only a function of temperature and partial pressure of hydrogen. Besides, the overpotentials in the oxygen electrode depend on temperature, and oxygen, carbon dioxide and steam content.

2.5.1.1. Model 1A

This first model was developed using single cells under oxygen electrode gas conditions. The electrolyte used during the test consists of a mixture of $(Li/K)_2CO_3$ or $(Li/Na)_2CO_3$ [58]. The overpotentials are divided in ohmic, fuel electrode activation, and oxygen electrode activation. This model has been applied in analyses of single cells calculating the overpotentials depending on the electrolyte used [59] and also in stacks to evaluate the performance using three-dimensional analysis to get the voltage, temperature, and current profiles [60]. The equations to determine the ohmic and activation losses are expressed in terms of specific electrical resistances stated as [59]:

Ohmic resistance

$$R_{ohm} = A_{ir} \exp\left(\frac{\Delta h_{ir}}{\mathbf{R}T}\right) \tag{2.14}$$

Fuel electrode activation resistance

$$R_{act,fe} = A_a T p_{\mathrm{H_2}}^{-0.5} \exp\left(\frac{\Delta h_a}{\mathbf{R}T}\right) \tag{2.15}$$

Oxygen electrode activation resistance

$$R_{act,oe} = A_{c_1} T p_{\mathrm{O_2}}^{-0.75} p_{\mathrm{CO_2}}^{0.5} \exp\left(\frac{\Delta h_{c_1}}{\mathbf{R}T}\right) + A_{c_2} T \exp\left(\frac{\Delta h_{c_2}}{\mathbf{R}T}\right) y_{\mathrm{CO_2}}^{-1} \tag{2.16}$$

The values of the coefficients for the previous equations are given in Table 2.1 for a $(Li/K)_2CO_3$ (62/38 mol %) electrolyte.

Table 2.1. Coefficients for Model 1A equations using $(Li/K)_2CO_3$ (62/38 mol %) electrolyte [59].

Parameters	Value	Units	Equation
A_{ir}	1.28×10^{-6}	$\Omega\,m^2$	(2.14)
Δh_{ir}	25 200	kJ/kmol	(2.14)
A_a	1.39×10^{-13}	$\Omega\,m^2\,atm^{0.5}\,K^{-1}$	(2.15)
Δh_a	77 800	kJ/kmol	(2.15)
A_{c_1}	1.97×10^{-13}	$\Omega\,m^2\,atm^{0.25}\,K^{-1}$	(2.16)
Δh_{c_1}	83 400	kJ/kmol	(2.16)
A_{c_2}	2.2×10^{-10}	$\Omega\,m^2\,K^{-1}$	(2.16)
Δh_{c_2}	22 800	kJ/kmol	(2.16)

2.5.1.2. Model 1B

This model is an improvement of model 1A, adding now the effect of steam on the oxygen electrode. The water dissolved in the electrolyte generates hydroxide ions which can affect the oxygen electrode overpotentials similar to carbon dioxide [57]. The ohmic resistance remain without any modification. Thus, the activation resistances are defined as [57]:

Fuel electrode activation resistance

$$R_{act,fe} = A_a p_{\mathrm{H_2}}^{-0.5} \exp\left(\frac{\Delta h_a}{\mathbf{R}T}\right) \tag{2.17}$$

Oxygen electrode activation resistance

$$R_{act,oe} = A_{c_1} p_{\mathrm{O_2}}^{-0.75} p_{\mathrm{CO_2}}^{0.5} \exp\left(\frac{\Delta h_{c_1}}{\mathbf{R}T}\right) + A_{c_2} \exp\left(\frac{\Delta h_{c_2}}{\mathbf{R}T}\right) \left(A_{c_3} y_{\mathrm{H_2O}} + y_{\mathrm{CO_2}}\right)^{-1} \tag{2.18}$$

2.5.1.3. Model 1C

This model has been developed using single cells by applying a $(\mathrm{Li/Na})_2\mathrm{CO_3}$ (60/40 mol %) mixture of electrolyte [61]. The activation resistance for the fuel electrode and the oxygen electrode are defined as:

Fuel electrode activation resistance

$$R_{act,fe} = A_a T p_{\mathrm{H_2}}^{-0.5} \exp\left(\frac{\Delta h_a}{\mathbf{R}T}\right) \tag{2.19}$$

Oxygen electrode activation resistance

$$\begin{aligned} R_{act,oe} = {} & A_{c_1} T p_{\mathrm{O_2}}^{-0.75} p_{\mathrm{CO_2}}^{0.5} \exp\left(\frac{\Delta h_{c_1}}{\mathbf{R}T}\right) \\ & + A_{c_2} T \exp\left(\frac{\Delta h_{c_2}}{\mathbf{R}T}\right) \left[A_{c_3} y_{\mathrm{H_2O}} \exp\left(\frac{\Delta h_{c_3}}{\mathbf{R}T}\right) + y_{\mathrm{CO_2}}\right]^{-1} \end{aligned} \tag{2.20}$$

2.5.1.4. Model 1D

This model is a kind of combination between model 1B and model 1C. This model has been applied to evaluate stacks containing a $(\mathrm{Li/Na})_2\mathrm{CO_3}$ (60/40 mol %) electrolyte [62]. The activation resistance equation in the fuel electrode is the same as Eq. (2.17). Besides, the oxygen electrode activation resistance equation combines Eq. (2.18) and Eq. (2.20) in order to consider the effect of steam and temperature, respectively. The resulting equation is presented as [62]:

$$R_{act,oe} = A_{c_1} p_{\mathrm{O_2}}^{-0.75} p_{\mathrm{CO_2}}^{0.5} \exp\left(\frac{\Delta h_{c_1}}{\mathbf{R}T}\right) + A_{c_2} \exp\left(\frac{\Delta h_{c_2}}{\mathbf{R}T}\right) \left[A_{c_3} y_{\mathrm{H_2O}} \exp\left(\frac{\Delta h_{c_3}}{\mathbf{R}T}\right) + y_{\mathrm{CO_2}}\right]^{-1} \tag{2.21}$$

2.5.2. Model 2

This model was proposed and developed by Yuh and Selman [63] using button cells and a $(\mathrm{Li/K})_2\mathrm{CO}_3$ (62/38 mol %) electrolyte. The voltage losses are determined evaluating the ohmic and activation energy overpotentials. In most of the cases, the ohmic resistance is calculated using Eq. (2.22) [64], but, this value depends on the set-up. This model considers the fuel electrode activation losses as a function of temperature and partial pressures of hydrogen, carbon dioxide and steam, Eq. (2.23) [63], unlike the previous model that only considered the hydrogen effect. Therefore, this model does not consider steam content in the oxygen electrode activation losses, Eq. (2.24) [63]. At high current densities the concentration losses can become significant, so this term is included as a function of the limiting current density in the fuel cell. Concentration losses are expressed in Eq. (2.25) [65, 66].

Ohmic resistance

$$R_{ohm} = 0.5 \times 10^{-4} \exp\left[3016\left(\frac{1}{T} - \frac{1}{923}\right)\right] \tag{2.22}$$

Fuel electrode activation resistanceosses

$$R_{act,fe} = 2.27 \times 10^{-9} p_{\mathrm{H_2}}^{-0.42} p_{\mathrm{CO_2}}^{-0.17} p_{\mathrm{H_2O}}^{-1} \exp\left(\frac{6,435}{T}\right) \tag{2.23}$$

Oxygen electrode activation resistance

$$R_{act,oe} = 7.505 \times 10^{-10} p_{\mathrm{O_2}}^{-0.43} p_{\mathrm{CO_2}}^{-0.09} \exp\left(\frac{9,289}{T}\right) \tag{2.24}$$

Concentration losses

$$V_{conc} = \frac{\mathbf{R}T}{n_e\mathbf{F}} \left(\frac{T - 273.15}{T_{ref}}\right)^2 \sum_K \upsilon_k \ln\left(1 - \frac{j}{j_{L,k}}\right) \tag{2.25}$$

2.5.3. Model 3

This model has been developed by the University of Genoa in collaboration with Ansaldo using single cells and a $(Li/K)_2CO_3$ electrolyte. In this model, the electrical resistance equations neglect the fuel electrode resistance. Only the ohmic resistance is considered, one resistance associated with the content of electrolyte in the matrix, and the oxygen electrode resistance. These resistances are expressed in Eq.(2.26) to Eq. (2.28) [67], respectively, and the constants are presented in Table 2.2. Initially the model does not consider the effect of concentration losses and the model was improved to consider it in terms of the limiting current density associated with hydrogen in the fuel electrode and carbon dioxide in the oxygen electrode, which is expressed in Eq. (2.29) [68, 69].

Table 2.2. Coefficients for Model 3 equations [67].

Coefficient	Value	Units
A	1.38×10^{-7}	$\Omega\,m^2\,Pa^{0.67}$
B	11 400	K
D	4.8×10^{-8}	$\Omega\,m^2$
F	6596	K
β	0.67	-
c_{ir}	0.348×10^{-4}	$\Omega\,m^2$

$$R_{contact} = c_{ir} \tag{2.26}$$

$$R_{electrolyte} = D \exp\left(\frac{F}{T}\right) \tag{2.27}$$

$$R_{electrode} = \frac{A \exp\left(\frac{B}{T}\right)}{\prod_i p_i^{\beta_i}} \tag{2.28}$$

$$\Delta V_{conc} = \frac{\mathbf{R}T}{n_e\mathbf{F}}\left[\ln\left(1 - \frac{j}{j_{L,H_2}}\right) + \frac{j}{j_{L,H_2}} + \ln\left(1 - \frac{j}{j_{L,CO_2}}\right) + \frac{j}{j_{L,CO_2}}\right] \tag{2.29}$$

2.5.4. Model 4

This model is proposed by Milewski et al. [70] considering only the electric phenomena involved in the fuel cell, i.e., the flow of ions and electrons, reducing the cell voltage calculation to fewer factors. The aim is to combine all cell working conditions in a number of factors as low as possible and having the factors relatively easy to determine. These factors include: the maximum voltage under isothermal conditions, V_{max}; the maximum current density, j_{max}; the fuel utilization factor, η_f; the area specific internal ionic resistance defined by the permeability of the electrolyte for carbonate ions, r_1; and the area specific internal electronic resistance, defined by the electric conductance of the molten electrolyte, r_2. The equation for the cell voltage is stated as [70]:

$$V_m = \frac{V_{max} - \eta_f j_{max} r_1}{\frac{r_1}{r_2}(1-\eta_f)+1} \tag{2.30}$$

2.5.5. Model 5

This is a model that has been developed using single cells and a $(\mathrm{Li/K})_2\mathrm{CO}_3$ (62/38 mol %) electrolyte. The model is based mainly on the polarization effect of the diffusion phenomena. The diffusion in the oxygen electrode considers two mechanisms, the Superoxide Path (SOP) and Peroxide Path (POP), however, the results indicate that POP shows a better agreement with experimental data [71]. Thus, POP was chosen for the kinetic formulation. Besides, the activation phenomenon is not considered because it is almost negligible for this kind of fuel cell [71]. Nevertheless, the model was improved and validated in a wide range of operation including steam in the oxygen electrode and carbon capture conditions [72–74]. The ohmic resistance is determined with experimental values following the Arrhenius type equation, Eq. (2.31). The polarization losses are divided for each electrode, in the case of the oxygen electrode the polarization resistance is expressed in terms of temperature, operational pressure, and the content of carbon dioxide, oxygen and water, Eq. (2.32) and Eq. (2.33). Thus, the fuel electrode resistance depends on temperature, operational pressure and the content of hydrogen, Eq. (2.34). The values of the parameters are given in Table 2.3.

Ohmic resistance

$$R_{ohm} = P_1 \exp\left(\frac{P_2}{T}\right) \tag{2.31}$$

Oxygen electrode polarization resistance

$$R_{\mathrm{CO_2,H_2O}} = \frac{P_3 T \exp\left(\frac{P_4}{T}\right)}{p \ln\left[1 - \left(\frac{1.5}{1+\vartheta}\right)(y_{\mathrm{CO_2}} + \vartheta y_{\mathrm{H_2O}})\right]^{-1}} \tag{2.32}$$

$$R_{\mathrm{O_2,CO_2}} = P_5 T \exp\left(\frac{P_6}{T}\right) p^{-0.25} y_{\mathrm{O_2}}^{-0.75} y_{\mathrm{CO_2}}^{0.5} \tag{2.33}$$

Fuel electrode polarization resistance

$$R_{\mathrm{H}_2} = \frac{P_7 T \exp\left(\frac{P_8}{T}\right)}{p \ln\left(1 + y_{\mathrm{H}_2}\right)} \tag{2.34}$$

Table 2.3. Coefficients for Model 5 equations [73].

Coefficients	Value	Units
P_1	1.6461×10^{-2}	$\Omega\,\mathrm{cm}^2$
P_2	3054	K
P_3	3.2×10^{-6}	$\Omega\,\mathrm{cm}^2\,\mathrm{K}^{-1}\,\mathrm{atm}$
P_4	2743	K
P_5	4.5×10^{-9}	$\Omega\,\mathrm{cm}^2\,\mathrm{K}^{-1}\,\mathrm{atm}^{0.25}$
P_6	10 036	K
P_7	3.4×10^{-9}	$\Omega\,\mathrm{cm}^2\,\mathrm{K}^{-1}\,\mathrm{atm}$
P_8	9362	K
ϑ	0.16	-

The voltage prediction of every model as a function of the current density is compared with data obtained from an experimental campaign only for the reference dry condition. Then, the model with the closer approach with the experimental curves is selected with the aim of subsequently being tested in electrolysis mode. The experimental campaigns are presented in chapter 3. Details of the numerical model are described in chapter 4. Finally, the experimental and numerical results are presented in chapter 5.

3

Experimental Set-up and Analysis Techniques

The experimental campaign was carried out to measure the performance of a single molten carbonate cell operating in reversible mode, i.e., switching between fuel cell mode and electrolysis mode.

3.1. Materials and cell assembly

The single cell tested has an electrode-electrolyte interface area of $80\,\mathrm{cm}^2$. The electrodes of the cell consist of Ni alloy and lithiated NiO, corresponding to fuel electrode and oxygen electrode, respectively. The electrolyte used was an eutectic mixture of $(Li/K)_2CO_3$ $(62/38\,\mathrm{mol}\,\%)$. A porous $LiAlO_2$ matrix is used to contain the electrolyte and give support to the cell. The current collectors used on each electrode are made of stainless steel SS-316L. Figure 3.1 shows the components of the single cell. Some specifications of standard components used in the tested MCFC are described in Table 3.1.

The cell is assembled from bottom to top following the next order (see Figure 3.2):

1. Fuel electrode cell frame.
2. Fuel electrode current collector.
3. Fuel electrode.
4. Matrix.
5. Oxygen electrode.
6. Oxygen electrode current collector.
7. Oxygen electrode cell frame.

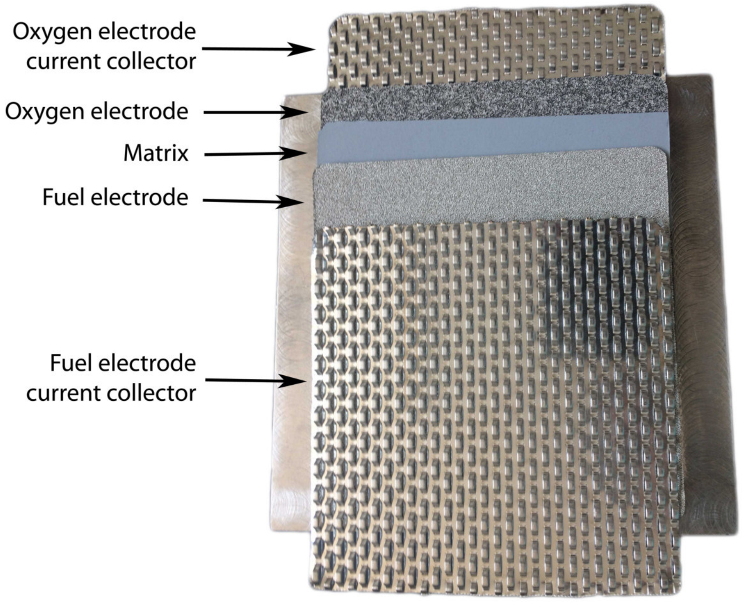

Figure 3.1. Molten carbonate single cell components.

Table 3.1. Characteristics of cell components used in the set-up [50, 75, 76].

	Fuel electrode
Material	Ni+5% wt Al or Ni+5% wt Cr
Thickness, mm	0.6 - 0.7
Porosity, %	52 - 65
	Oxygen electrode
Material	Lithiated NiO
Thickness, mm	0.6 - 0.7
Porosity, %	60 - 77
	Electrolyte
Material, mol %	Li_2CO_3/K_2CO_3, 62/38
	Matrix
Material	γ-$LiAlO_2$
	Current collector
Material	SUS-316L

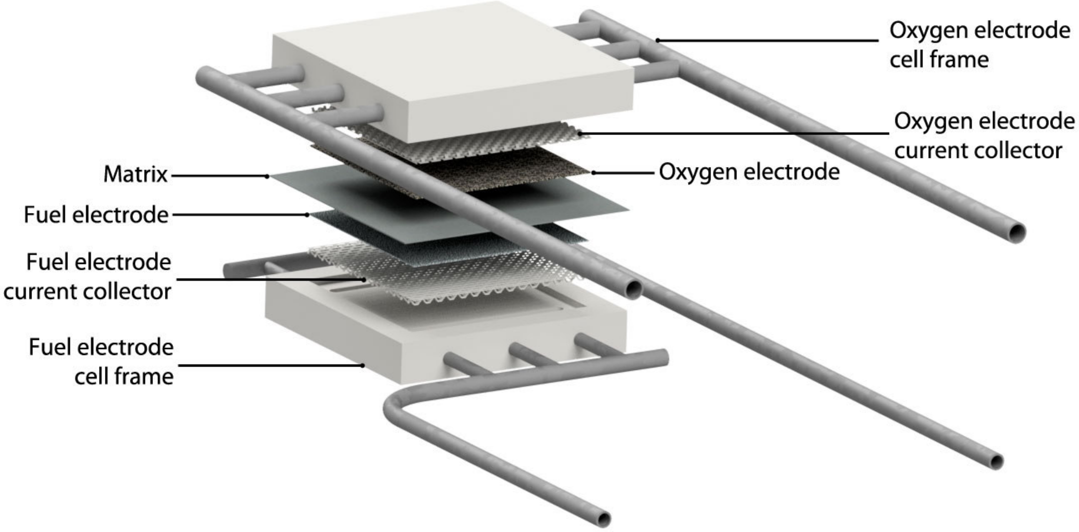

Figure 3.2. Molten carbonate single cell assembly.

The electrolyte is added and spread over the oxygen electrode current collector. During the cell heating, when the melting point of the electrolyte is reached, it converts into liquid and goes down by gravity, filling in this way the oxygen electrode, matrix and fuel electrode as shown in Figure 3.3. The filling degree depends of the capillarity forces acting in every component [47].

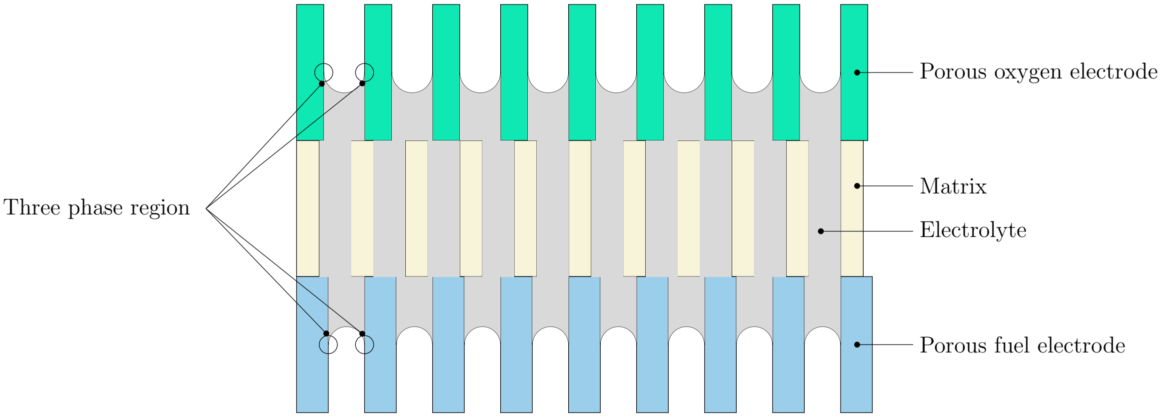

Figure 3.3. Distribution of molten carbonate electrolyte in porous electrodes of MCFC as a result of balance in capillary pressure (adpated from [47]).

3.2. Single cell test station

The single cell was tested in the test bench shown in Figure 3.4. The test bench is equipped with Bronkhorst® gas flow meters for all the gases except water which was supplied to the mixture using a Controlled Evaporation and Mixing system (CEM). Five K thermocouples are used to monitor the thermal behavior of the system, two thermocouples are placed in the lines supplying the gases (fuel and oxygen line), another one at the exit of the fuel electrode. The aim of these is to control the temperature of the gases by line-heaters to ensure that water present in the lines remains in gaseous state avoiding stagnation points, that lead to erroneous data. The last two thermocouples are in the furnace and the fuel electrode housing. A sealing pressure of ~0.2 MPa [77] is maintained by a mechanical load that compresses axially the cell, to ensure a good contact among the cell components and a good gas seal on the wet seal area. All these components and parameters are controlled and monitored by a LabView custom-made software.

Figure 3.4. Molten carbonate single cell test bench.

Besides, auxiliary equipment to test and monitor the electrochemical performance was used, including an Agilent® N5743A DC power supply and an Agilent® N3300A DC electronic load to supply and extract a specific current, respectively, letting the cell to operate reversibly and obtaining polarization curves. Besides, a Solartron Interface SI-1287 was used to carry out Electrochemical Impedance Spectroscopy (EIS). EIS and polarization curves were used to characterize the performance of the cell. EIS measurements were performed at OCV, cell mode and electrolyzer mode. Concerning OCV, a potentiostatic perturbation of 10 mV was chosen. In order to ensure cell and electrolyzer mode, an electrical current of 1 A was extracted from (+) or supplied to (-) the system, respectively, with a galvanostatic perturbation of 0.8 A. Regarding polarization curves, these were obtained extracting or supplying current to simulate fuel cell and electrolysis mode, respectively. The current was varied with increments of 10 mA/cm^2, until getting close to the limiting current.

3.3. Experimental Campaign

After the start-up procedure, the single cell was operated galvanostatically for a short time, until steady state in terms of voltage and internal resistance was reached. Once the performance of the cell was steady the experimental campaign started.

The experimental work is divided into two steps: firstly, the cell is operated only in cell mode to study the effect of different operating parameters on the cell performance in order to compare the available electrochemical models already used in other works, to determine the model that best fits with the experimental results; then, this model is calibrated to fit with data obtained during the experimental campaign. Table 3.2 shows the tested conditions. Run 1 indicates the reference condition for this campaign.

Table 3.2. Conditions tested for fuel cell model validation.

		Composition, Vol %		
		Fuel electrode	Oxygen electrode	
Type	Run	$CO_2/H_2O/H_2/N_2$	$CO_2/O_2/N_2$	T, °C
Ref	1	18/11/71/0	6/12/82	650
$H_{2,fe}$ effect	2	20/0/**70**/**10**	6/12/82	650
	3	20/0/**60**/**20**	6/12/82	650
	4	20/0/**50**/**30**	6/12/82	650
$CO_{2,oe}$ effect	5	18/11/71/0	**20**/12/**68**	650
	6	18/11/71/0	**10**/12/**78**	650
	7	18/11/71/0	**4**/12/**84**	650
T_{cell} effect	8	18/11/71/0	6/12/82	**680**
	9	18/11/71/0	6/12/82	**620**

Secondly, an experimental step was performed to test the cell working in reversible mode, although the aim is to understand the performance of the cell working in reverse mode, i.e., electrolysis mode. To get a better comprehension of the phenomena occurring in the cell, gas compositions and flow rates fed to fuel and oxygen electrodes were varied along with cell temperature. Particular importance was dedicated to the ratio between flow rates of oxygen and fuel electrodes respectively (Electrodes Flow Ratio, EFR). This was tested to get the minimum flow rate required in the oxygen electrode since no flow seems to be required when the cell works in electrolysis mode, as Eq. (2.1) indicates. The conditions tested in this second experimental part are listed in Table 3.3. Run 2 was chosen as the reference condition in reversible mode: the components entering on each electrode which are participating in the reactions have the same proportion, allowing to compare the variations of inlet compositions and monitor the cell degradation.

Table 3.3. Experimental conditions tested for reversible mode in the second experimental campaign.

		Composition, Vol %				
		Fuel electrode	Oxygen electrode			
	Run	$CO_2/H_2O/H_2/N_2$	$CO_2/O_2/N_2$	p_{O_2}/p_{CO_2}	EFR	T, °C
EFR	1	25/25/25/25	25/25/50	1	**1**	650
	2	25/25/25/25	25/25/50	1	2	650
	3	25/25/25/25	25/25/50	1	**3**	650
	4	25/25/25/25	25/25/50	1	**4**	650
Fuel electrode composition	5	**30**/25/25/**20**	25/25/50	1	2	650
	6	**40**/25/25/**10**	25/25/50	1	2	650
	7	**50**/25/25/**0**	25/25/50	1	2	650
	8	25/**30**/25/**20**	25/25/50	1	2	650
	9	25/**40**/25/**10**	25/25/50	1	2	650
	10	25/**50**/25/**0**	25/25/50	1	2	650
	11	25/25/**15**/**35**	25/25/50	1	2	650
	12	25/25/**5**/**45**	25/25/50	1	2	650
Oxygen electrode composition	13	25/25/25/25	**20**/25/**55**	**1.25**	2	650
	14	25/25/25/25	**15**/25/**60**	**1.67**	2	650
	15	25/25/25/25	**10**/25/**65**	**2.5**	2	650
	16	25/25/25/25	**5**/25/**70**	**5**	2	650
	17	25/25/25/25	25/**20**/**55**	**0.8**	2	650
	18	25/25/25/25	25/**15**/**60**	**0.6**	2	650
	19	25/25/25/25	25/**10**/**65**	**0.4**	2	650
	20	25/25/25/25	25/**5**/**70**	**0.2**	2	650
Tcell	21	25/25/25/25	25/25/50	1	2	**630**
	22	25/25/25/25	25/25/50	1	2	**610**
	23	25/25/25/25	25/25/50	1	2	**590**
	24	25/25/25/25	25/25/50	1	2	**570**

3.4. Long-term operation

Finally, the third experimental campaign was carried out to study the degradation rate of a Molten Carbonate Electrolysis Single Cell with a gas composition trying to simulate a real operating condition with a low amount of hydrogen and carbon dioxide in the fuel electrode and oxygen electrode, respectively. In the fuel electrode a high content of water and carbon dioxide was supplied to promote the reaction (2.7). Besides, in the oxygen electrode air was supplied with a low content of carbon dioxide, i.e., 5 % to avoid an increase in overpotentials in electrolysis mode and avoid problems associated to corrosion [78]. Table 3.4 shows the conditions set in the long-term test of the single MCEC.

Table 3.4. Conditions tested for the long-term test during the third experimental campaign.

Fuel electrode		Oxygen electrode		
Composition, Vol % $CO_2/H_2O/H_2/N_2$	Flow NmL/min	Composition, Vol % $CO_2/O_2/N_2$	Flow NmL/min	T ℃
47.5/47.5/5/0	330	5/20/75	1320	650

The results of the three experimental campaigns, aside from a numerical and experimental comparison, are presented in chapter 5.

4

Zero-Dimensional Thermodynamic Analysis

In this chapter the thermodynamic concepts to analyze the chemical reactions occurring in the fuel electrode and the oxygen electrode are presented. Besides, the equations needed to determine the concentration overpotentials are shown. Finally, a section is included to present the expressions to determine the heat losses, the thermal efficiency and the thermo-neutral voltage.

4.1. Chemical reactions in equilibrium

4.1.1. Molten Carbonate Fuel Cell reactions

In a Molten Carbonate Fuel Cell, hydrogen is the main reactant that oxidizes to produce electricity according to reaction in Eq. (2.2). MCFCs can operate using hydrocarbon fuels, reforming them by reaction in Eq. (2.5), to produce hydrogen and carbon monoxide. Besides, the carbon monoxide reacts chemically by Water Gas Shift, reaction in Eq. (2.6), producing hydrogen and carbon dioxide.

It is considered that steam reforming (SR) and water gas shift (WGS) reactions are occurring inside the fuel electrode in the presence of Ni catalyst. Besides, the cell is considered to operate in steady state condition and the gas mixtures are treated as ideal gases. Thus, the equilibrium constants of the reactions are function only of temperature, and the partial pressure of the gases at the outlet as [65, 79]:

$$K_{eq,SR} = \frac{p_{\mathrm{H_2}}^3 p_{\mathrm{CO}}}{p_{\mathrm{CH_4}} p_{\mathrm{H_2O}}} \tag{4.1}$$

$$K_{eq,WGS} = \frac{p_{\mathrm{CO_2}} p_{\mathrm{H_2}}}{p_{\mathrm{CO}} p_{\mathrm{H_2O}}} \tag{4.2}$$

The equilibrium constants as a function of temperature, $K_{eq,i}(T)$, can be determined knowing the standard Gibbs free energy change for the reaction involved, stated as [55]:

$$\ln K_{eq,\text{SR or WGS}}(T) = -\frac{\Delta \bar{g}^{o}_{\text{SR or WGS}}}{\mathbf{R}T} \tag{4.3}$$

In this way, taking into consideration all the reactions involved in the fuel electrode during DIR, three simultaneous reactions should be solved to determine the amount of hydrogen, methane and carbon monoxide which are reacting in each reaction. These are indicated with a superscript r in the next reactions [79, 80]:

$$\overbrace{H_2}^{r} + CO_3^{2-} \longrightarrow H_2O + CO_2 + 2\,e^- \qquad \textit{Electrochemical} \tag{4.4a}$$

$$\overbrace{CH_4}^{r} + H_2O \longrightarrow CO + 3\,H_2 \qquad SR \tag{4.4b}$$

$$\overbrace{CO}^{r} + H_2O \longrightarrow CO_2 + H_2 \qquad WGS \tag{4.4c}$$

The molar flow rate of hydrogen, methane and carbon monoxide reacting in each reaction are defined as $\dot{n}^r_{H_2}$, $\dot{n}^r_{CH_4}$ and $\dot{n}^r_{CO}$, respectively. The chemical equilibrium is considered to occur at the exit of the fuel electrode. Hence, a mole balance at the exit of the fuel electrode is performed to determine the amount of these species. The total molar flow rate balance is stated as [80]:

$$\dot{n}^e_{CH_4} = \dot{n}^{in}_{CH_4} - \dot{n}^r_{CH_4} \tag{4.5a}$$

$$\dot{n}^e_{CO} = \dot{n}^{in}_{CO} + \dot{n}^r_{CH_4} - \dot{n}^r_{CO} \tag{4.5b}$$

$$\dot{n}^e_{CO_2} = \dot{n}^{in}_{CO_2} + \dot{n}^r_{H_2} + \dot{n}^r_{CO} \tag{4.5c}$$

$$\dot{n}^e_{H_2O} = \dot{n}^{in}_{H_2O} + \dot{n}^r_{H_2} - \dot{n}^r_{CH_4} - \dot{n}^r_{CO} \tag{4.5d}$$

$$\dot{n}^e_{H_2} = \dot{n}^{in}_{H_2} - \dot{n}^r_{H_2} + 3\dot{n}^r_{CH_4} + \dot{n}^r_{CO} \tag{4.5e}$$

$$\dot{n}^e_{fe} \overline{= \dot{n}^{in}_{fe} + \dot{n}^r_{H_2} + 2\dot{n}^r_{CH_4}} \tag{4.5f}$$

The molar flow-rate of hydrogen consumed by the cell, Eq. (2.2), is determined by the reaction rate of the cell. It depends of the current demanded, I, and the number of electrons involved in the reaction, n_e [65].

$$\dot{n}^r_{H_2} = \frac{I}{n_e \mathbf{F}} \tag{4.6}$$

Meanwhile, the molar flow rates of methane and carbon monoxide reacting in the SR and WGS reaction, respectively, are determined calculating the partial pressures of every component as $p_i = p(\dot{n}_i^e/\dot{n}_{fe}^e)$, and replaced in the equilibrium constant previously defined in Eq. (4.1) and Eq. (4.2) [79, 80].

$$K_{eq,SR} = \frac{\left(\dfrac{\dot{n}_{\mathrm{CO}}^{in} + \dot{n}_{\mathrm{CH_4}}^{r} - \dot{n}_{\mathrm{CO}}^{r}}{\dot{n}_{fe}^{in} + \dot{n}_{\mathrm{H_2}}^{r} + 2\dot{n}_{\mathrm{CH_4}}^{r}}\right)\left(\dfrac{\dot{n}_{\mathrm{H_2}}^{in} - \dot{n}_{\mathrm{H_2}}^{r} + 3\dot{n}_{\mathrm{CH_4}}^{r} + \dot{n}_{\mathrm{CO}}^{r}}{\dot{n}_{fe}^{in} + \dot{n}_{\mathrm{H_2}}^{r} + 2\dot{n}_{\mathrm{CH_4}}^{r}}\right)^3\left(\dfrac{p}{p_{ref}}\right)^2}{\left(\dfrac{\dot{n}_{\mathrm{CH_4}}^{in} - \dot{n}_{\mathrm{CH_4}}^{r}}{\dot{n}_{fe}^{in} + \dot{n}_{\mathrm{H_2}}^{r} + 2\dot{n}_{\mathrm{CH_4}}^{r}}\right)\left(\dfrac{\dot{n}_{\mathrm{H_2O}}^{in} + \dot{n}_{\mathrm{H_2}}^{r} - \dot{n}_{\mathrm{CH_4}}^{r} - \dot{n}_{\mathrm{CO}}^{r}}{\dot{n}_{fe}^{in} + \dot{n}_{\mathrm{H_2}}^{r} + 2\dot{n}_{\mathrm{CH_4}}^{r}}\right)} \tag{4.7}$$

$$K_{eq,WGS} = \frac{\left(\dfrac{\dot{n}_{\mathrm{CO_2}}^{in} + \dot{n}_{\mathrm{H_2}}^{r} + \dot{n}_{\mathrm{CO}}^{r}}{\dot{n}_{fe}^{in} + \dot{n}_{\mathrm{H_2}}^{r} + 2\dot{n}_{\mathrm{CH_4}}^{r}}\right)\left(\dfrac{\dot{n}_{\mathrm{H_2}}^{in} - \dot{n}_{\mathrm{H_2}}^{r} + 3\dot{n}_{\mathrm{CH_4}}^{r} + \dot{n}_{\mathrm{CO}}^{r}}{\dot{n}_{fe}^{in} + \dot{n}_{\mathrm{H_2}}^{r} + 2\dot{n}_{\mathrm{CH_4}}^{r}}\right)}{\left(\dfrac{\dot{n}_{\mathrm{CO}}^{in} + \dot{n}_{\mathrm{CH_4}}^{r} - \dot{n}_{\mathrm{CO}}^{r}}{\dot{n}_{fe}^{in} + \dot{n}_{\mathrm{H_2}}^{r} + 2\dot{n}_{\mathrm{CH_4}}^{r}}\right)\left(\dfrac{\dot{n}_{\mathrm{H_2O}}^{in} + \dot{n}_{\mathrm{H_2}}^{r} - \dot{n}_{\mathrm{CH_4}}^{r} - \dot{n}_{\mathrm{CO}}^{r}}{\dot{n}_{fe}^{in} + \dot{n}_{\mathrm{H_2}}^{r} + 2\dot{n}_{\mathrm{CH_4}}^{r}}\right)} \tag{4.8}$$

Knowing the amount of hydrogen reacting, $\dot{n}_{\mathrm{H_2}}^{r}$, the molar flow rate of methane and carbon monoxide are determined solving simultaneously Eq. (4.7) and Eq. (4.8), where the classical Newton-Raphson method can be used.

4.1.2. Molten Carbonate Electrolysis Cell reactions

Contrary to the MCFC, the electrochemical reactions involved in an MCEC are the reduction of water and carbon dioxide in the fuel electrode, and the oxidation of the carbonate ion in the oxygen electrode, as shown in Figure 2.3. The main electrochemical reaction occurring in the fuel electrode for hydrogen production is the simultaneous reduction of water and carbon dioxide stated in Eq. (2.7) [43]. Besides, there is the possibility that carbon dioxide reacts electrochemically to produce carbon monoxide through the following reaction [43]:

$$2\,\mathrm{CO_2} + 2\,\mathrm{e^-} \longrightarrow \mathrm{CO} + \mathrm{CO_3^{2-}} \tag{4.9}$$

However, in this study, only Eq. (2.7) is assumed to be occurring in the fuel electrode because the carbon dioxide electrolysis generating carbon monoxide is considered slower than hydrogen production in Eq. (2.7). Thus, the carbon monoxide present in the cell is generated through the reversed water-gas shift reaction [43].

4.1.2.1. Reversed water-gas shift reaction

At high temperatures, above 500 °C, and in presence of a Ni catalyst, there is considered that the reversed water-gas shift (RWGS) reaction, Eq.(4.10), will very rapidly reach equilibrium [43].

$$H_2 + CO_2 \longrightarrow H_2O + CO \tag{4.10}$$

The equilibrium constant for RWGS is expressed as:

$$K_{eq,RWGS} = \frac{p_{CO}p_{H_2O}}{p_{CO_2}p_{H_2}} \tag{4.11}$$

The equilibrium constant value, $K_{eq,RWGS}$, can be determined by Eq. (4.3). Taking into consideration the reactions involved in the fuel electrode during electrolysis mode, two simultaneous reactions should be solved to determine the amount of water and carbon dioxide which is reacting in each reaction. These are indicated with a superscript r in the next reactions:

$$\overbrace{H_2O}^{r} + CO_2 + 2\,e^- \longrightarrow H_2 + CO_3^{2-} \qquad \textit{Electrochemical} \tag{4.12a}$$

$$\overbrace{CO_2}^{r} + H_2 \longrightarrow H_2O + CO \qquad \textit{RWGS} \tag{4.12b}$$

The molar flow rate of water and carbon dioxide reacting in each reaction is defined as $\dot{n}^r_{H_2O}$ and $\dot{n}^r_{CO_2}$, respectively. Alike MCFC, the chemical equilibrium is considered to occur at the exit of the fuel electrode. Hence, a mole balance at the exit of the fuel electrode is performed to determine the amount of these species. Contrary to MCFC, in electrolysis mode, the methane is not supplied and it can be only formed at high pressures [12]. Nevertheless, it is not considered to be involved in the reactions of the fuel electrode since the cell is operated at atmospheric pressure.

$$\dot{n}^e_{CO} = \dot{n}^{in}_{CO} + \dot{n}^r_{CO_2} \tag{4.13a}$$

$$\dot{n}^e_{CO_2} = \dot{n}^{in}_{CO_2} - \dot{n}^r_{H_2O} - \dot{n}^r_{CO_2} \tag{4.13b}$$

$$\dot{n}^e_{H_2O} = \dot{n}^{in}_{H_2O} - \dot{n}^r_{H_2O} + \dot{n}^r_{CO_2} \tag{4.13c}$$

$$\dot{n}^e_{H_2} = \dot{n}^{in}_{H_2} + \dot{n}^r_{H_2O} - \dot{n}^r_{CO_2} \tag{4.13d}$$

$$\dot{n}^e_{fe} \overline{= \dot{n}^{in}_{fe} - \dot{n}^r_{H_2O}} \tag{4.13e}$$

The molar flow rate of water consumed by Eq. (2.7) to be electro-oxidized depends on the current demanded, I, and the number of electrons involved in the reaction, n_e. The molar flow rate of carbon dioxide that is being electro-oxidazed is equal to the amount of water that is involved in the same reaction. These molar flow rates consumed are determined by the Faraday equation:

$$\dot{n}^{r}_{\mathrm{H_2O}} = \frac{I}{n_e \mathbf{F}} \tag{4.14}$$

Meanwhile, the molar flow rate of carbon dioxide reacting in the RWGS reaction is determined solving Eq. (4.11). Thus, $\dot{n}^{r}_{\mathrm{CO_2}}$ is obtained substituting the partial pressures in Eq. (4.11) and solving Eq. (4.15)

$$K_{eq,RWGS} = \frac{\left(\dot{n}^{in}_{\mathrm{CO}} + \dot{n}^{r}_{\mathrm{CO_2}}\right)\left(\dot{n}^{in}_{\mathrm{H_2O}} - \dot{n}^{r}_{\mathrm{H_2O}} + \dot{n}^{r}_{\mathrm{CO_2}}\right)}{\left(\dot{n}^{in}_{\mathrm{CO_2}} - \dot{n}^{r}_{\mathrm{H_2O}} - \dot{n}^{r}_{\mathrm{CO_2}}\right)\left(\dot{n}^{in}_{\mathrm{H_2}} + \dot{n}^{r}_{\mathrm{H_2O}} - \dot{n}^{r}_{\mathrm{CO_2}}\right)} \tag{4.15}$$

4.2. Mass balance

Electrochemical devices are subject to reacting mixtures that convert the chemical energy content in the fuel and produce new species. However, a mass balance should be performed to verify that mass conservation is occurring in the chemical process. Mass conservation equation in steady state is defined as [55]:

$$\dot{m}_{in} = \dot{m}_{e} \tag{4.16}$$

where $\dot{m}_{in}$ and $\dot{m}_{e}$ are the net mass flow rates entering and exiting the fuel electrode and oxygen electrode, respectively.

$$\dot{m}_{fe,in} + \dot{m}_{oe,in} = \dot{m}_{fe,e} + \dot{m}_{oe,e} \tag{4.17}$$

The calculation of the total mass flow rate at the exit of any electrode is determined considering the addition of the source term of each specie involved in the electrochemical reactions as:

$$\dot{m}_{fe,e} = \dot{m}_{fe,in} + \sum_{j=1}^{j} S_j \tag{4.18}$$

$$\dot{m}_{oe,e} = \dot{m}_{oe,in} + \sum_{j=1}^{j} S_j \tag{4.19}$$

The mass source term for any component is defined as [66, 81–83]:

$$S_j = \frac{I \upsilon_j M_j}{n_e \mathbf{F}} \tag{4.20}$$

S_j is determined considering the stoichiometric coefficients υ_j for the reactions in the fuel electrode or the oxygen electrode. The sign for υ_j is considered positive if the specie involved is a product and negative if the specie involved is a reactant. Once the composition leaving each electrode is determined and the mass balance has been verified, voltage losses can be calculated.

4.3. Voltage losses

The voltage of the cell is a function of the operating conditions as temperature, composition of the gases and current density as Eq. (2.12) indicates. When a fuel cell is operated with a certain electric current, the cell voltage drops below the thermodynamically predicted value. This is due mainly by three major types of fuel cell losses: activation, ohmic and concentration. If the system is operating in fuel cell mode or electrolysis mode, the voltage losses are going to be subtracted or added to the open circuit voltage, respectively, in order to obtain the actual voltage, as presented in Figure 2.4 and Eq. (2.11).

Concerning the voltage losses presented in Eq. (2.11), five semi-empirical electro-kinetic models already published have been considered to determine the ohmic, activation and concentration voltage losses. These models and their particularities are presented in section 2.5. Thus, Table 4.1 summarizes what voltage losses are taken into account by Model 1 [57–59], Model 2 [63, 65], Model 3 [67–69], Model 4 [70], and Model 5 [71–74], as well as the size of the cell used to validate the models. It is worth to be noticed that Model 4 calculates the actual voltage in terms of other parameters, so that the values of ohmic, activation and concentration overpotentials are not calculated directly.

Table 4.1. Zero-dimensional models comparison.

Overpotential	Model 1	Model 2	Model 3	Model 4	Model 5
Ohmic	✔	✔	✔	✗	✔
Activation fuel electrode	✔	✔	✗	✗	✗
Activation oxygen electrode	✔	✔	✔	✗	✗
Concentration	✗	✔	✔	✗	✔
Obtained by	SC	BC	SC	SC	SC

SC: Single cell
BC: Button cell

In [78], it is presented that Model 5 gives a closer prediction of the voltage than the other 4 models. However, a fitting was required in order to approach the model to the experimental data of the first experimental campaign. Thus, Model 5 was adjusted with these experimental data, giving a good correlation between the numerical and experimental voltage in fuel cell mode. However, the correlation between the numerical and experimental voltage in electrolysis mode was not totally good as in fuel cell mode. It was mainly reflected when the estimated voltage was obtained close to the limiting current density, the adjusted model was not able to predict correctly this region. Hence, it was required to improve the concentration overpotentials prediction.

4.3.1. Concentration voltage losses

The way in which concentration affects Nernst voltage is because the real reversible thermodynamic voltage of a fuel cell is determined by the reactant and product concentration at the reaction sites. The limiting case for mass transport is when the reactant concentration in the catalyst layer drops all the way to zero. Thus, the fuel cell can never sustain a higher current density than that which causes the reactant concentration to fall to zero. It is the limiting current density of the fuel cell or electrolyzer. Therefore, the limiting current density is calculated by Fick's law and expressed in Eq. (4.21).

$$j_L = n_e \mathbf{F} D^{eff} \frac{c_R^0}{\delta} \tag{4.21}$$

Fuel cell mass transport design strategies focus on increasing the limiting current density. These design strategies include the following:

a) Ensuring a high c_R^0, by designing good flow structures that evenly distribute reactants.
b) Ensuring that D^{eff} is larger and δ is small, by carefully optimizing fuel cell operating conditions, electrode structure, and diffusion layer thickness.

A fuel cell will never be able to produce a higher current density than that determined by its limiting current density. However, the other fuel cell losses, ohmic and activation losses, may reduce the fuel cell voltage to zero well before the limiting current density is ever reached.

There are several components in a gas mixture, thus, the effective diffusion coefficient $D_{i,m}^{eff}$ for a component i in the mixture depends on the molecular interaction of specie i with the other components in the mixture as stated in [84]:

$$D_{i,m}^{eff} = \frac{1 - y_i}{\displaystyle\sum_{i,j \neq i} \frac{y_j}{D_{ij}^{eff}}} \tag{4.22}$$

In porous structures, the gas molecules tend to be impeded by the pore walls as they diffuse. The diffusion flux should therefore be corrected to account for the effects of such blockage. Because the pores are not straight, the diffusion effectively takes place over a longer distance than it would in a homogeneous material. The effects of longer pores and smaller areas are often lumped together in an effective diffusion as [16, 85]:

$$D_{ij}^{eff} = \frac{\varepsilon}{\tau} D_{ij} \tag{4.23}$$

Based on the kinetic gas theory, the binary diffusion coefficient is calculated as [86]:

$$D_{ij} = \frac{0.001T^{1.75}\left(\frac{M_i + M_j}{M_i M_j}\right)^{0.5}}{\left(\nu_i^{1/3} + \nu_j^{1/3}\right)^2 p} \tag{4.24}$$

The limiting current density expression in Eq. (4.21) requires determination of the bulk concentration c_i^0, which can be obtained using the ideal gas law, taking into account the partial pressure of the specie of interest, stated as [16]:

$$c_i^0 = \frac{p_i^0}{\mathbf{R}T} \tag{4.25}$$

Thus, the limiting current density, j_L is stated as:

$$j_L = \frac{n_e \mathbf{F} D_{i,m}^{eff}}{\delta} \frac{y_i p}{\mathbf{R}T} \tag{4.26}$$

Once the limiting current density calculation is evaluated, the concentration losses for the fuel electrode and oxygen electrode in both operating modes can be defined. The way in which concentration affects Nernst voltage is because the real reversible thermodynamic voltage of a fuel cell is determined by the reactant and product concentrations at the reaction sites. The calculation of the change in the Nernst potential considering the difference in concentration between the bulk, c^0, and the catalyst layer, c^*, is defined as [16]:

$$\eta_{conc} = \frac{\mathbf{R}T}{n_e \mathbf{F}} \sum_i \ln\left(\frac{c_i^0}{c_i^*}\right)^{\upsilon_i} \tag{4.27}$$

The ratio c^0/c^* can be written as [16]:

$$\frac{c_i^0}{c_i^*} = \frac{j_{L,i}}{j_{L,i} - j} \tag{4.28}$$

Substituting Eq. (4.28) into Eq. (4.27), the concentration overpotentials can be expressed in terms of the limiting current density as:

$$\eta_{conc} = \frac{\mathbf{R}T}{n_e\mathbf{F}} \sum_i \ln \left(\frac{j_{L,i}}{j_{L,i} - j} \right)^{\upsilon_i} \tag{4.29}$$

Thus, the concentration losses in terms of the limiting current densitiesor each electrode in both operating modes are presented.

a) Concentration losses in the fuel electrode in fuel cell mode.

$$\eta_{conc,fe} = \frac{\mathbf{R}T}{n\mathbf{F}} \ln \left[\left(\frac{j_{L,\mathrm{H_2}}}{j_{L,\mathrm{H_2}} - j} \right) \left(\frac{j_{L,\mathrm{H_2O}} - j}{j_{L,\mathrm{H_2O}}} \right) \left(\frac{j_{L,\mathrm{CO_2}} - j}{j_{L,\mathrm{CO_2}}} \right) \right] \tag{4.30}$$

b) Concentration losses in the oxygen electrode in fuel cell mode.

$$\eta_{conc,oe} = \frac{\mathbf{R}T}{n\mathbf{F}} \ln \left[\left(\frac{j_{L,\mathrm{O_2}}}{j_{L,\mathrm{O_2}} - j} \right)^{1/2} \left(\frac{j_{L,\mathrm{CO_2}}}{j_{L,\mathrm{CO_2}} - j} \right) \right] \tag{4.31}$$

c) Concentration losses in the fuel electrode in electrolysis mode.

$$\eta_{conc,fe} = \frac{\mathbf{R}T}{n\mathbf{F}} \ln \left[\left(\frac{\mid j_{L,\mathrm{H_2}} \mid - \mid j \mid}{\mid j_{L,\mathrm{H_2}} \mid} \right) \left(\frac{\mid j_{L,\mathrm{H_2O}} \mid}{\mid j_{L,\mathrm{H_2O}} \mid - \mid j \mid} \right) \left(\frac{\mid j_{L,\mathrm{CO_2}} \mid}{\mid j_{L,\mathrm{CO_2}} \mid - \mid j \mid} \right) \right] \tag{4.32}$$

d) Concentration losses in the oxygen electrode in electrolysis mode.

$$\eta_{conc,oe} = \frac{\mathbf{R}T}{n\mathbf{F}} \ln \left[\left(\frac{\mid j_{L,\mathrm{O_2}} \mid - \mid j \mid}{\mid j_{L,\mathrm{O_2}} \mid} \right)^{1/2} \left(\frac{\mid j_{L,\mathrm{CO_2}} \mid - \mid j \mid}{\mid j_{L,\mathrm{CO_2}} \mid} \right) \right] \tag{4.33}$$

4.4. Energy balance

Once the chemical reactions occurring inside the cell and the electrical losses have been calculated, it is possible to perform an energy balance in the cell. The conservation of energy principle remains valid even when a chemical reaction occurs within the system. Thus, it is necessary to evaluate the enthalpies of the gases flowing to or from the cell. In the case of a mixture, the specific enthalpy for a compound in the mixture at a state other than the reference is found by adding the specific enthalpy change between the reference state and the one of insterest, plus the enthalpy of formation, expressed as [55, 87]:

$$h_i = h^0_{f,i} + (h_i - h_{ref}) \tag{4.34}$$

The energy balance for a reacting system is defined in Eq. (4.35) [55, 87]. For this study, the isothermal condition is considered in the thermal analysis, assuming the cell temperature constant for all the components along the cell. Figure 2.2 and Figure 2.3 show the control volume for the fuel cell and electrolyzer, respectively, where the energy balance is going to be applied.

$$\dot{Q}_{CV} - \dot{W}_{CV} = \sum_{e} \dot{m}_i h_i - \sum_{in} \dot{m}_i h_i \tag{4.35}$$

where $\dot{W}_{CV}$ is the power produced by the cell, and $\dot{Q}_{CV}$ is the heat transfer rate to the cell. The sign convection for heat and work is [55]:

- Heat
  - $\dot{Q}_{CV} > 0$: heat transferred to the system.
  - $\dot{Q}_{CV} < 0$: heat transferred from the system.
- Work
  - $\dot{W}_{CV} > 0$: work done by the system.
  - $\dot{W}_{CV} < 0$: work done on the system.

The heat transfer rate is an energy non-available by the cell to produce power. According to the Gouy-Stodola theorem, the loss of work is equal to the irreversibilities within the system. These are determined by the rate of entropy production multiplied by a reference temperature [88].

$$\dot{Q}_{CV} = \dot{W}_{lost} = T_0 \dot{\sigma} \tag{4.36}$$

The production of entropy is determined applying a balance of entropy on the cell, which is stated as [55, 87]:

$$\dot{\sigma} = \sum_{e} \dot{m}_i s_i - \sum_{in} \dot{m}_i s_i - \sum_{j} \frac{\dot{Q}_j}{T_j} \tag{4.37}$$

The term $\dot{Q}_j$ represents the heat transfer rate at the location on the boundary where the instantaneous temperature is T_j. This term is determined by the losses of voltage multiplied by the current, which represents a heat production [32]. To maintain an agreement with the sign convection, the heat is multiplied by a minus, indicating that heat is transferred from the system.

$$\dot{Q}_j = -I\left(V_{Nernst} - V\right) \tag{4.38}$$

The ideal first-law efficiency $\eta_{th,I}$ of a fuel cell at temperature T is the ratio of the useful energy to the total energy, expressed as [16, 87]:

$$\eta_{th,I} = \frac{\text{useful energy}}{\text{total energy}} = \frac{\Delta g}{\Delta h} \tag{4.39}$$

The second-law efficiency $\eta_{th,II}$ of a fuel cell and an electrolyzer at temperature T are expressed in Eq. (4.40) and Eq. (4.41), respectively [89].

$$\eta_{th,II} = \frac{V}{V_{Nernst}} \tag{4.40}$$

$$\eta_{th,II} = \frac{V_{Nernst}}{V} \tag{4.41}$$

The experimental and numerical results of the single MCFC operating in reversible mode are presented in chapter 5.

5

Results and Discussion

In this chapter the results are presented in three parts. The first part is related to the experimental results focused on the reversible operation of the molten carbonate cell; in the second one the modeling results are presented; finally, in the third one the experimental results of the long-term test of the cell operating in electrolysis mode are presented. Two experimental campaigns were carried out in order to study the parameters that affect the most the performance of reversible molten carbonate cells. The first campaign, Table 3.2, had the objective to collect data of a MCFC to compare numerically five MCFC models available in literature. Then, the selection of one model is performed with the aim of fitting it with the experimental data. Finally, a comparison of the fitted model is carried out with data of the second campaign where the cell works in reversible mode. Therefore, the discussion of this first campaign is presented in section 5.2, where the model fitting is presented.

5.1. Experimental results of the MCFC operating in reversible mode.

Figure 5.1 summarizes the evolution of the internal resistance during the first and second experimental campaign divided into two zones: 1) fuel cell mode, and 2) reversible mode. The first zone related to cell mode, from 0 h to 650 h, does not present significant changes in the internal resistance. Contrary for the second zone where reversible mode was tested, from 650 h to 800 h, presents a significant rise in the internal resistance at a rate of about $4.2 \times 10^{-5}\,\Omega/\text{h}$, possible hypotheses are given in the end of the section. However, the internal resistance remains basically constant during the period from 650 h to 800 h, making it possible to perform a reliable comparison between experimental and numerical data for this period. To perform a better comparison between experimental data during the second campaign, the reference condition, run 2, i.e. a 25/25/25/25% $CO_2/H_2O/H_2/N_2$ fuel electrode gas composition and a 25/25/50% $CO_2/O_2/N_2$ oxygen electrode gas composition at 650 °C, was tested before every set of parameters presented in Table 3.3, in order to track the cell internal resistance. If there is some degradation present, it will be possible to perform at least a qualitative comparison for the cases where the degradation was higher.

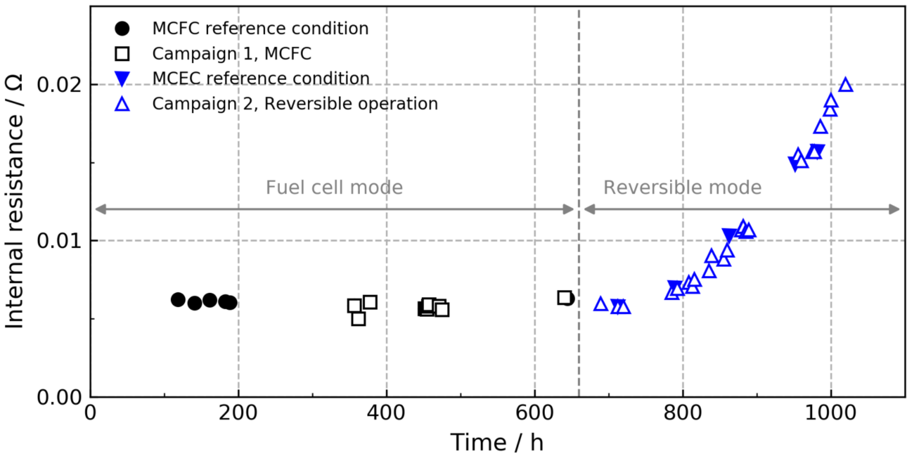

Figure 5.1. Evolution of the internal resistance in MCFC reversible operation.

One way to compare the modes of operation is by using the EIS technique. Figure 5.2 shows an example of the electrochemical impedance spectra comparison of the single cell in OCV, in cell and electrolysis mode with the conditions of Run 12, i.e. a 25/5/25/45% $CO_2/H_2O/H_2/N_2$ fuel electrode gas composition and a 25/25/50% $CO_2/O_2/N_2$ oxygen electrode gas composition at 650 °C. The results indicate a larger impedance in cell mode than in OCV and electrolysis mode, indicating that the cell shows a higher polarization for hydrogen oxidation. Also, the region of high frequency related to charge transfer shows minimal differences. Thus, electrolysis mode seems to be a good mode of operation to decrease polarization losses because the production of hydrogen decreases the polarization losses. This result is similar with the ones reported by Lu et al. [46], which have been obtained by testing button cells.

5.1.1. Cell temperature effect.

Analyzing the effect of temperature, presented in Figure 5.3, it can be observed that the performance is better at higher temperatures for both modes of operation, in this case at 650 °C. The decrease of performance could be explained by the increase in the internal resistance and activation overpotentials, which are inversely dependent on temperature. Figure 5.4 shows that internal resistance grows when cell temperature is reduced which is expected because the ionic resistivity rises as temperature decreases, opposing the flow of carbonate ions. Besides, an increment in the concentration polarization and transfer resistance, related with low and high frequency regions, respectively, are associated with low cell temperatures.

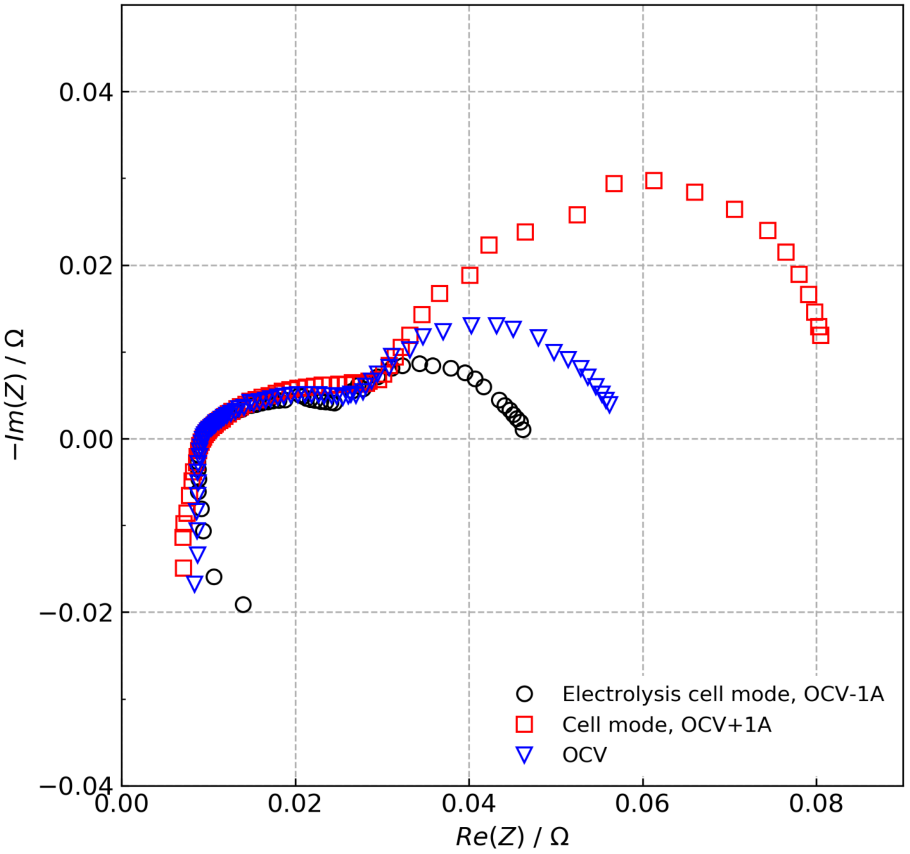

Figure 5.2. Electrochemical impedance spectra of the single cell in electrolysis mode, cell mode and OCV with the fuel electrode gas composition of 25/5/25/45%, $CO_2/H_2O/H_2/N_2$ at 650 °C.

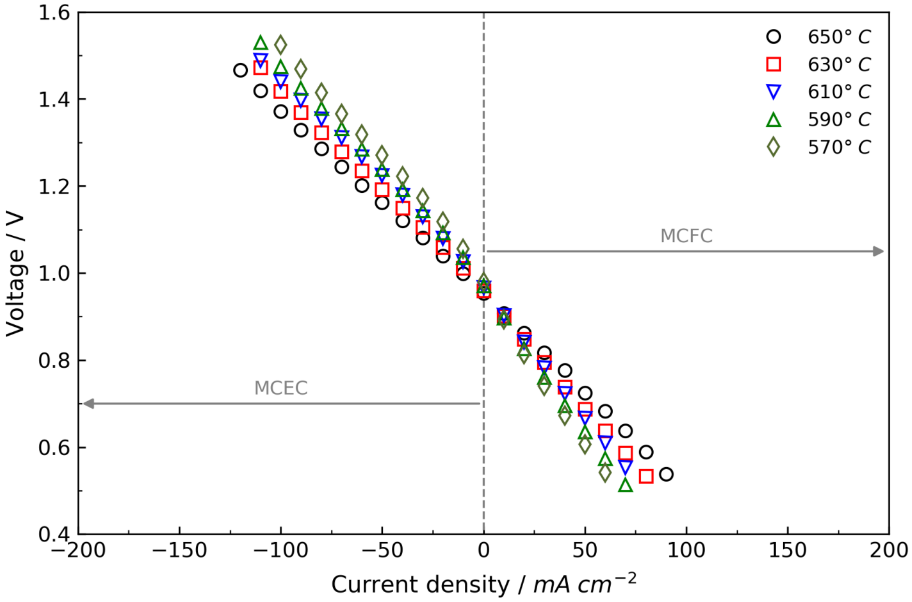

Figure 5.3. Experimental temperature effect during MCFC reversible operation.

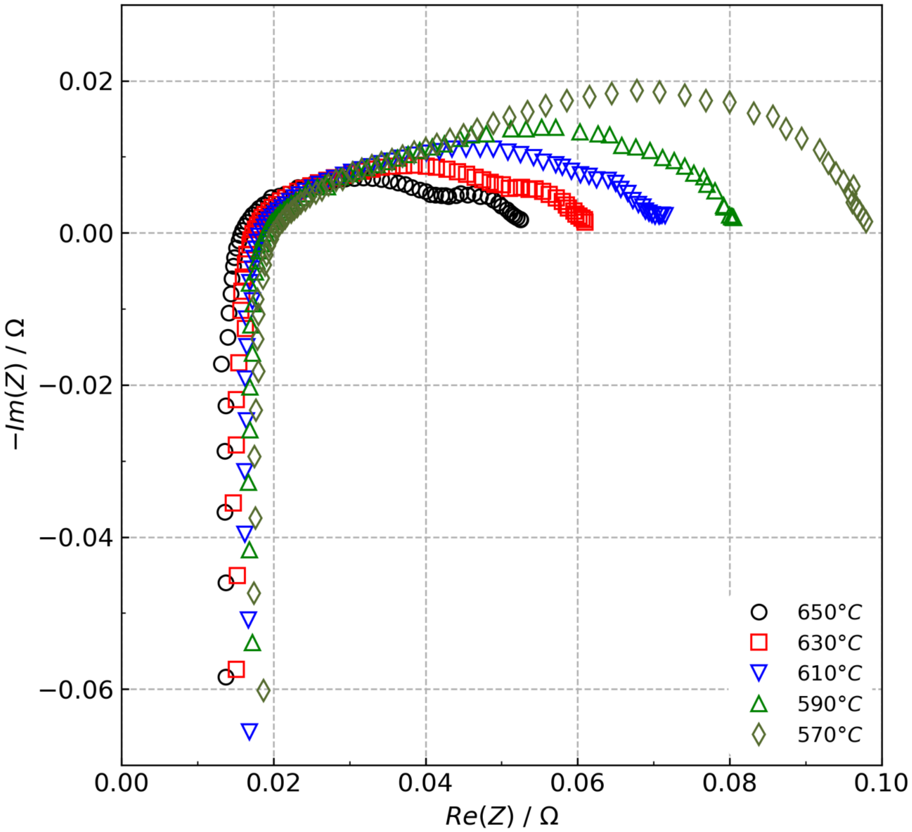

Figure 5.4. Electrochemical impedance spectra of the cell temperature effect in OCV.

5.1.2. Electrode flow ratio effect.

Figure 5.5 shows the experimental voltage under fuel cell and electrolysis operation at different Electrodes Flow Ratio (EFR, oxygen-to-fuel) with fuel and oxidant composition of 25/25/25/25%, $CO_2/H_2O/H_2/N_2$ and 25/25/50%, $CO_2/O_2/N_2$, respectively. It can be observed a higher influence in electrolysis cell mode, having a decrease in polarization resistance when increasing the EFR up to 3. In previous studies [42–46], the electrode flow rate was equal to 1, nevertheless, a cooling effect and diffusion could be favored increasing the EFR. In the polarization curves presented in Figure 5.5, there is a symmetric effect of limiting current density that can be observed, since both modes of operation show the limiting current density in almost the same point, around $130\,\mathrm{mA/cm^2}$ and $-130\,\mathrm{mA/cm^2}$, for fuel cell and electrolysis mode, respectively. The limiting current density should be avoided in practice because of reactants starvation. Figure 5.6 shows the electrochemical impedance spectra in OCV related to changes in EFR, in this case an EFR of 4 increases the polarization losses, indicating that higher EFR does not necessarily give a better performance.

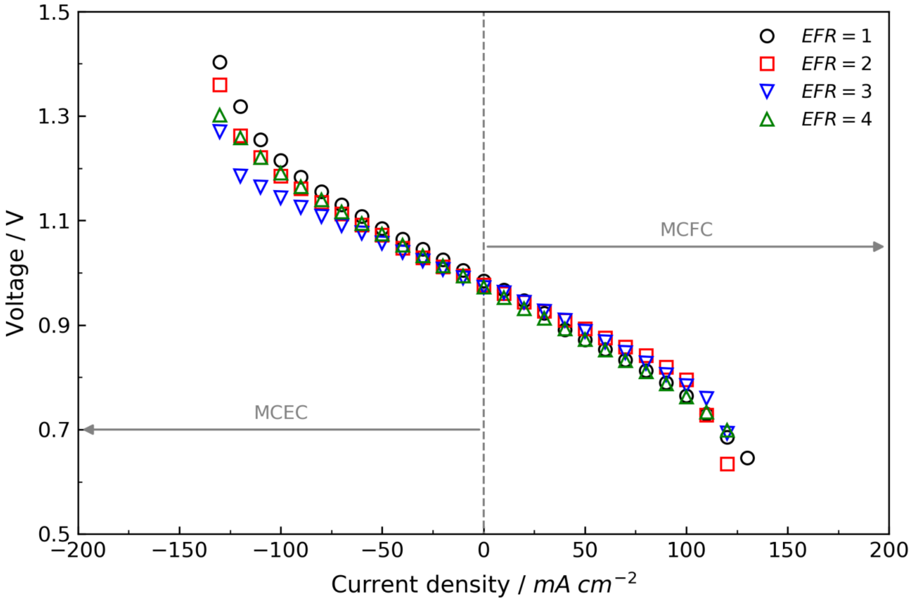

Figure 5.5. Experimental Electrodes Flow Ratio (EFR) effect in reversible MCFC operation.

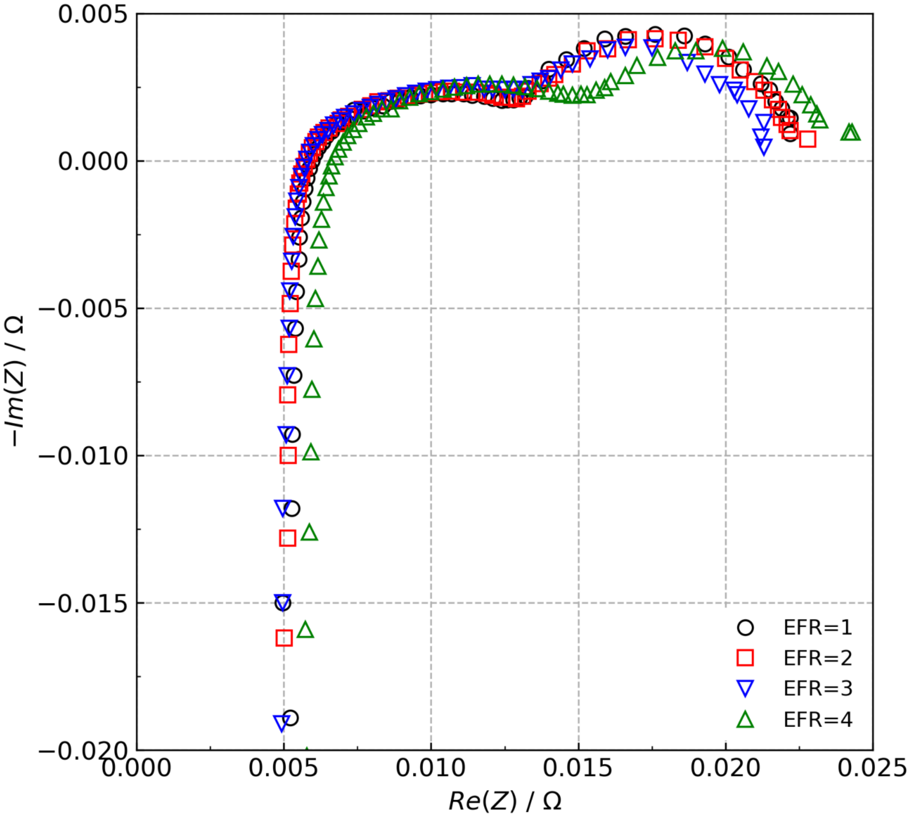

Figure 5.6. Electrochemical impedance spectra of the EFR effect in OCV at 650 °C.

5.1.3. Fuel electrode gas composition effect.

The effect of composition variations in the stream supplied to the fuel electrode is presented from Figure 5.7 to Figure 5.12, which are related to carbon dioxide, water and hydrogen effect, respectively, during MCFC reversible operation.

Figure 5.7 shows the effect of CO_2 composition in the fuel electrode. Results show that higher CO_2 concentration in the fuel electrode working in electrolysis mode improves the performance. According to Eq. (2.4), carbon dioxide and water react in the same ratio to produce hydrogen in the electrolysis process. However, Figure 5.7 shows that, although water has been consumed, carbon dioxide seems to continue reacting. This fact can be explained because carbon dioxide can react with hydrogen in the RWGS reaction, Eq. (4.10), forming water and carbon monoxide, then the water formed reacts with the remaining carbon dioxide to produce again hydrogen, Eq. (2.7). Contrary, in the MCFC region the performance of the cell is diminished when the amount of carbon dioxide in the fuel electrode is raised. The explanation for this decrease is that increasing the CO_2 content in the fuel electrode, hydrogen reacts with this in the reverse water gas shift reaction provoking a faster consumption of hydrogen and, consequently, higher overpotentials.

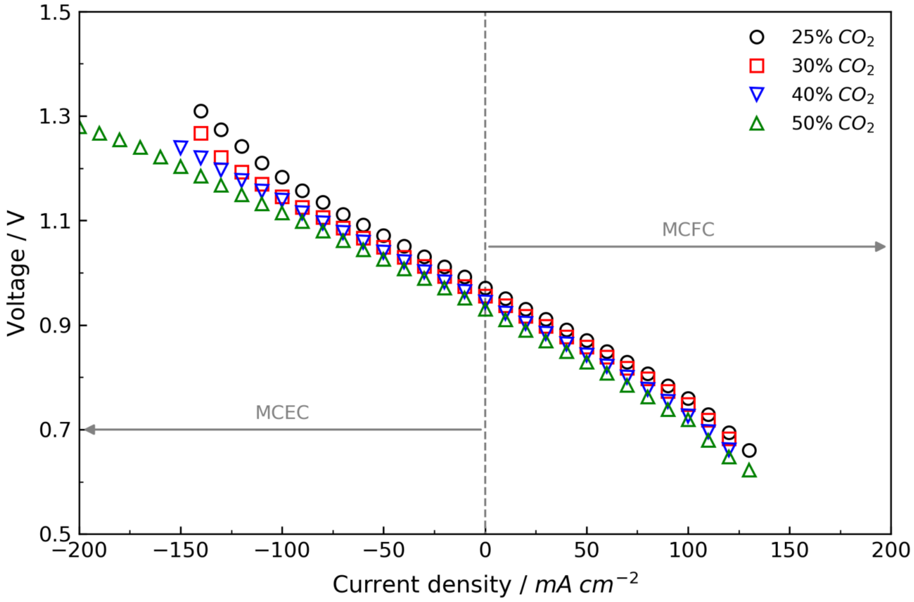

Figure 5.7. Experimental CO_2 concentration effect in the fuel electrode during MCFC reversible operation.

Electrochemical impedance spectra of the CO_2 effect in the fuel electrode are presented in Figure 5.8. There are no changes in the high frequency region and internal resistance, however, in the low frequency region associated to the concentration polarization, the radii of the semicircles tend to increase when the content of CO_2 decreases, which was also confirmed by the polarization curves.

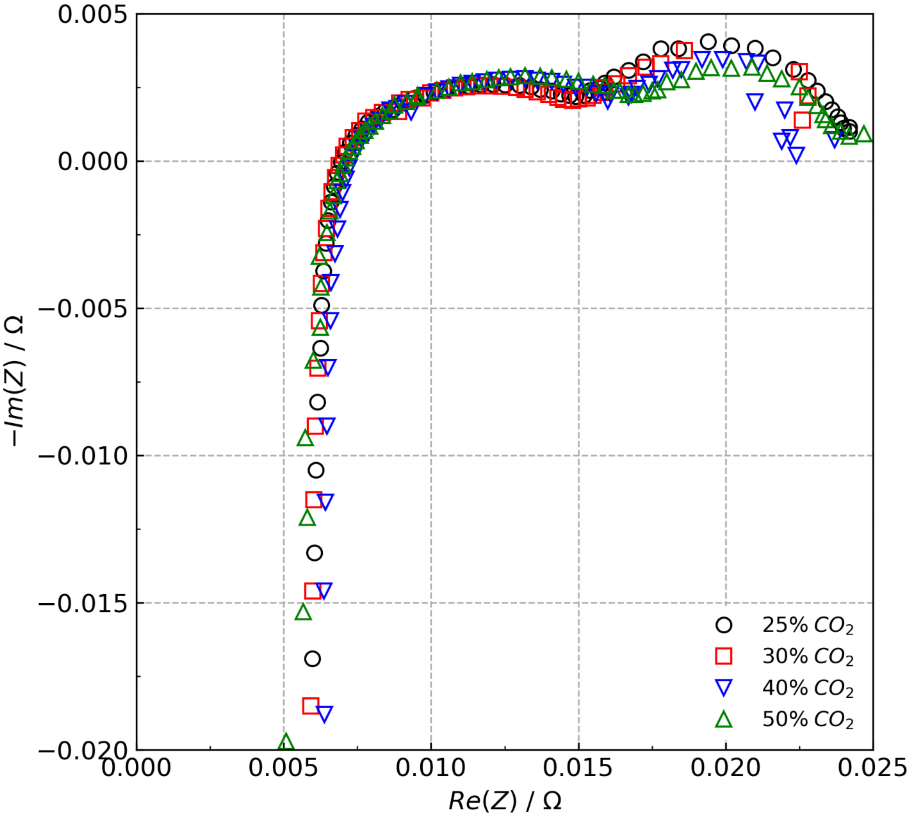

Figure 5.8. Electrochemical impedance spectra of the CO_2 concentration effect in the fuel electrode in OCV at 650 °C.

Regarding water concentration in the fuel electrode, the polarization curves shown in Figure 5.9 indicate a small effect on the cell voltage when working in electrolysis mode. Hydrogen and carbon dioxide concentration in the fuel electrode were kept constant, thus, according to the reduction reaction of water and carbon dioxide in Eq. (2.2), the reaction is limited by the smallest amount between these compounds. Besides, contrary to carbon dioxide, water can not react unless CO_2 is present. This is one reason that the polarization curves in Figure 5.7 and Figure 5.9 show small changes for all the cases.

Analyzing the electrochemical impedance spectra for water effect in the fuel electrode in electrolysis mode shown in Figure 5.10, there is an increase in the internal resistance, a growth in the high frequency region and an increase in the low frequency region, all of this when the water content is increased.

Concerning hydrogen content, it is necessary to avoid provoking fast degradation in the cell by a too lean hydrogen supply. Nonetheless, in fuel cell mode, the hydrogen is elemental to perform the oxidation reaction, and its lack is reflected in a bad performance as Figure 5.11 shows. When the cell is operated with 5 % of hydrogen, it is depleted faster at lower current

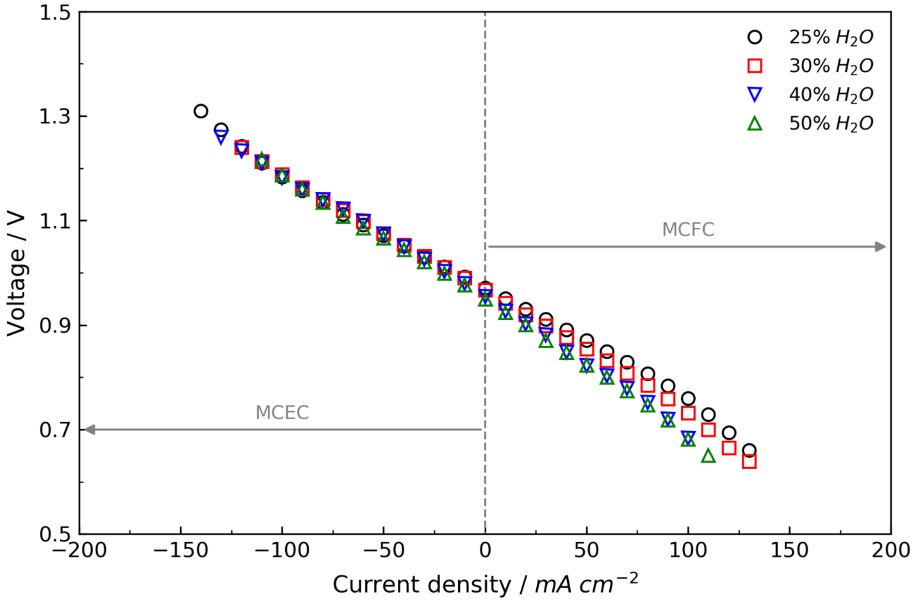

Figure 5.9. Experimental H_2O concentration effect in the fuel electrode during MCFC reversible operation.

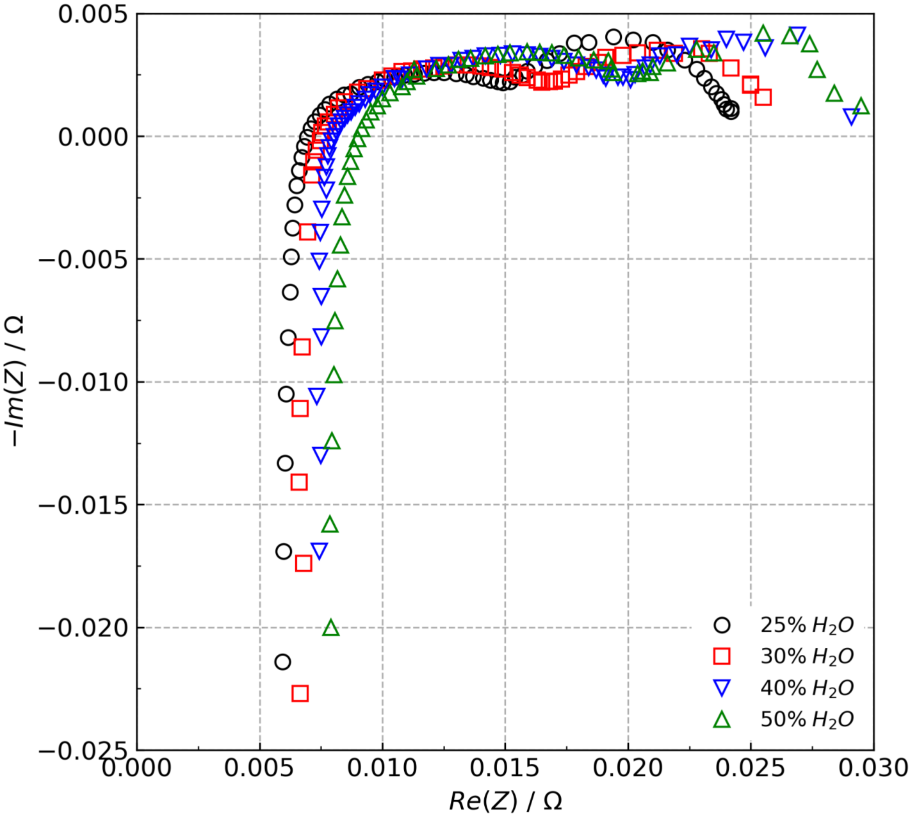

Figure 5.10. Electrochemical impedance spectra of the H_2O concentration effect in the fuel electrode in electrolysis mode at 650 °C.

densities causing limiting conditions to be reached at lower loads when compared with cases of higher H_2 concentration. In electrolysis mode, the objective is hydrogen production. It is desired to minimize the amount required of hydrogen in electrolysis mode if its possible to zero. In electrolysis mode, the performance improves with lower H_2 concentration at lower current densities, converging at one point, approximately at $120\,\mathrm{mA/cm^2}$, where the differences are minimum, rising again at higher current densities. As can be seen in Figure 5.12, the presence of H_2 helps to reduce concentration losses. In the polarization curves can be observed that increasing the hydrogen concentration in fuel cell mode the performance is improved. In electrolysis mode, increasing the current density, the hydrogen content rises decreasing the overpotentials. The hydrogen effect can be observed in the electrochemical impedance spectroscopy curves in OCV presented in Figure 5.12, where there is an evident difference in the increase in the polarization losses caused by the lack of hydrogen. There is an increase in the polarization losses between 15 % and 5 % of H_2 concentration of around $1.93 \times 10^{-2}\,\Omega$, representing an increment of approximately 52.3 % respect to a 15 % of H_2 concentration.

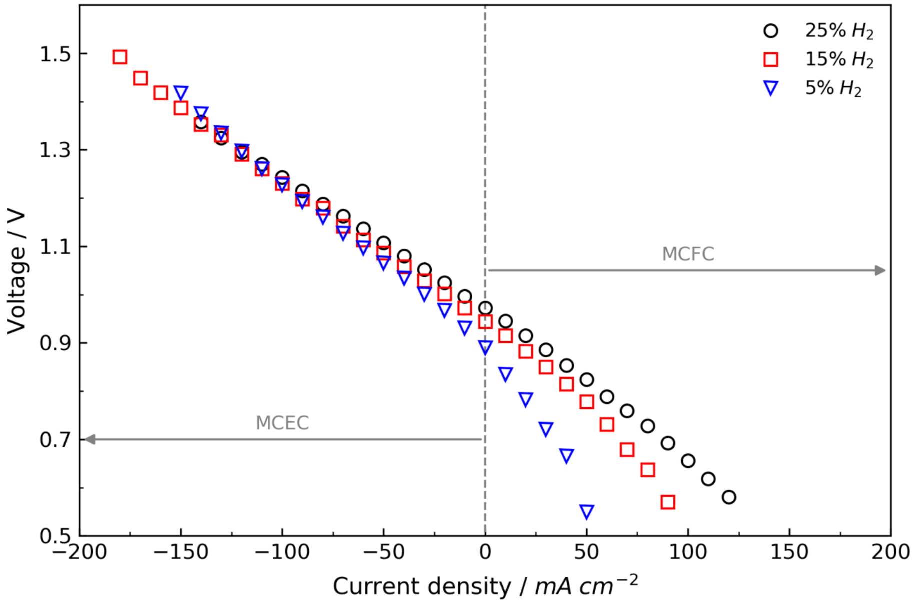

Figure 5.11. Experimental H_2 concentration effect in the fuel electrode during MCFC reversible operation.

5.1.4. Oxygen electrode gas composition effect.

Now, the effect of carbon dioxide and oxygen variations in the oxygen electrode when the cell operates in reversible mode are presented from Figure 5.13 to Figure 5.16. However, these gases are supplied to the oxygen electrode to deplete the gases formed by oxidation of the carbonate ions, as Eq. (2.1) states.

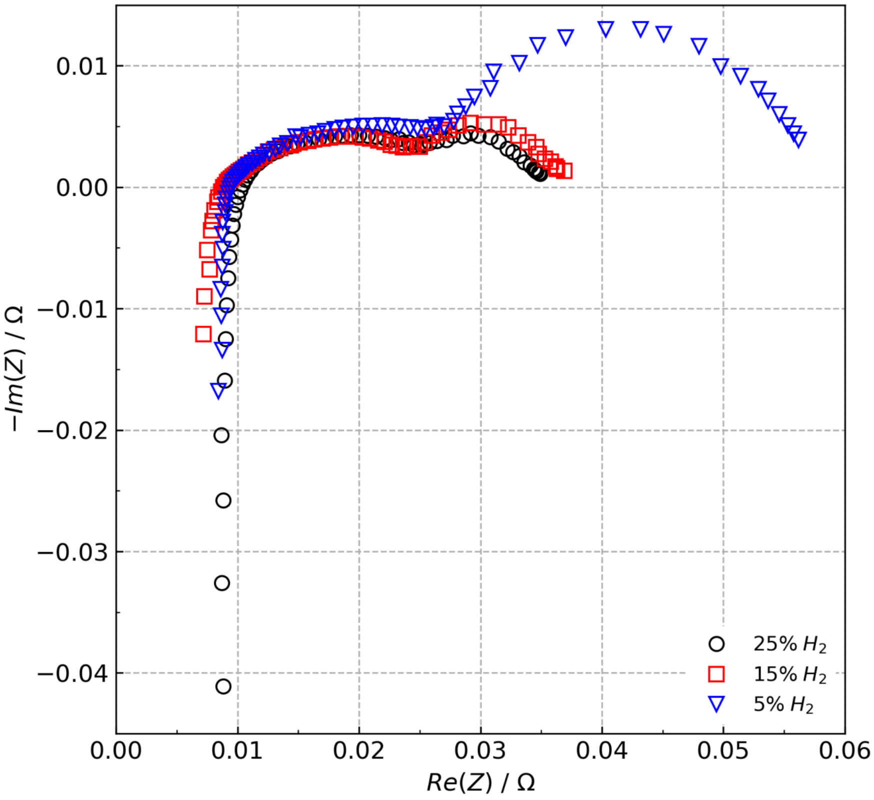

Figure 5.12. Electrochemical impedance spectra of the H_2 concentration effect in the fuel electrode in electrolysis mode at 650 °C.

Regarding the effect of carbon dioxide in the oxygen electrode, it is more evident in fuel cell mode where a lean gas mixture in carbon dioxide highly increase the overpotentials, thus, a limiting point is reached at lower current densities, as shown in Figure 5.13. Contrarily to fuel cell mode, in electrolysis mode a lower content of carbon dioxide gives a better performance that is maintained up to around $-100\,\mathrm{mA/cm^2}$, after that current density, the effect is inverted and the higher amount of carbon dioxide gives a better performance. Besides, after this current density, it seems that current limitation starts because the overpotentials begin to increase faster. The effect of decreasing the CO_2 content in the flow entering the oxygen electrode is more perceptible in Figure 5.14. For this parameter, its effect is noticeable in the low frequency region where concentration losses are increased with lower CO_2 content. However, in almost all the cases, the shape of the spectra remains basically constant. The increase in polarization losses caused by the reduction in carbon dioxide content is approximately $5.6 \times 10^{-3}\,\Omega$, representing an increment of 16 % between the maximum and minimum CO_2 tested concentration.

On the other hand, Figure 5.15 shows the effect of oxygen concentration in the oxygen electrode. This specie causes in fuel cell mode a reduction of performance when its concen-

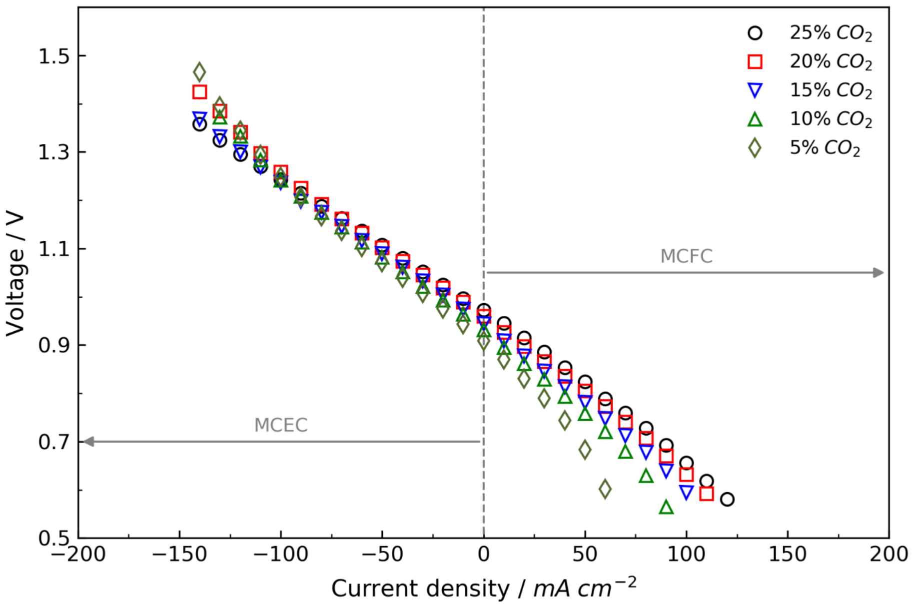

Figure 5.13. Experimental CO_2 concentration effect in the oxygen electrode during MCFC reversible operation.

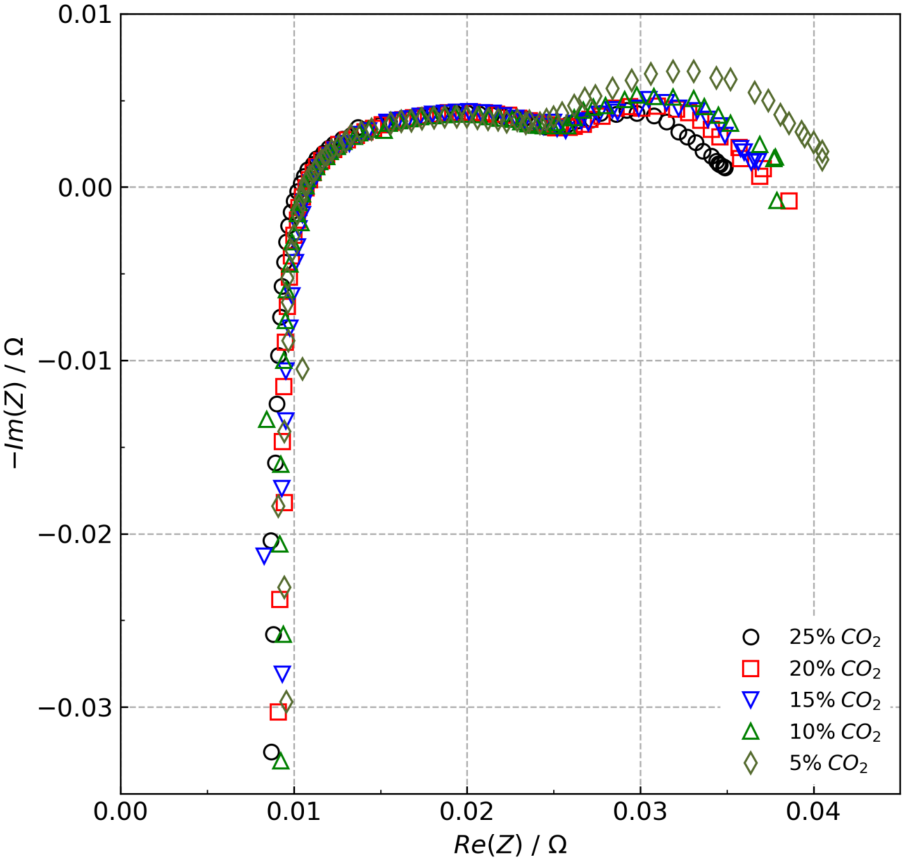

Figure 5.14. Electrochemical impedance spectra of the CO_2 concentration effect in the oxygen electrode in OCV at 650 °C.

tration is decreased, similarly to what carbon dioxide causes. In electrolysis mode, the higher amount of oxygen causes an improvement in the performance being more evident at high current densities.

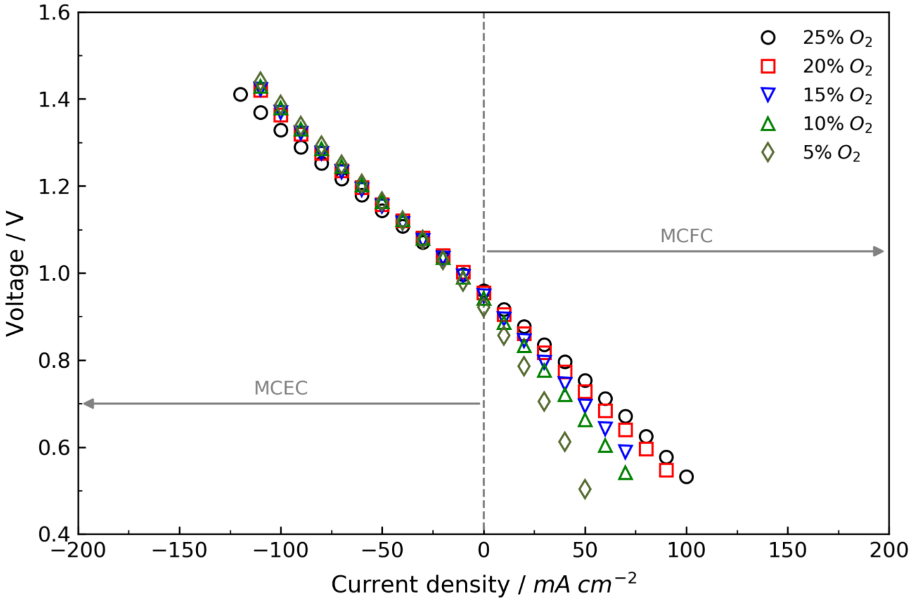

Figure 5.15. Experimental O_2 concentration effect in the oxygen electrode during MCFC reversible operation.

Figure 5.16 shows the electrochemical impedance spectra of oxygen content variations in the oxygen electrode. The internal resistance presents a slight increment in the analyzed cases, contrary to the polarization resistance that is highly increased when the content of oxygen is reduced. Referring to run 20 where the content of oxygen and carbon dioxide were 5 % and 25 %, respectively, corresponding to a pressure ratio (p_{O_2}/p_{CO_2}) of 0.2, shows that the polarization zone is almost merged with the electronic charge zone, i.e. low and high frequency regions, respectively; besides, electronic charge phenomena show a growing effect when decreasing the content of oxygen. The increase in polarization losses between the maximum and minimum amount of oxygen tested, 25 % and 5 %, respectively, is approximately $2.27 \times 10^{-2}\,\Omega$, corresponding to 46.23 %.

5.1.5. Cell degradation and refilling.

The tested cases in the second campaign were carried out varying a p_{O_2}/p_{CO_2} ratio in the oxygen electrode from 0.2 to 5. According to literature, a high partial pressure of carbon dioxide in the oxygen electrode accelerates NiO dissolution, promoting Ni short circuits [24]. Morita et al. [24] performed accelerated tests on MCFC to study Ni short circuits by setting a high partial pressure of carbon dioxide, a p_{O_2}/p_{CO_2} ratio of 0.176, close to the value in run 20, showing that it is better to supply the minimum possible amount of carbon dioxide to

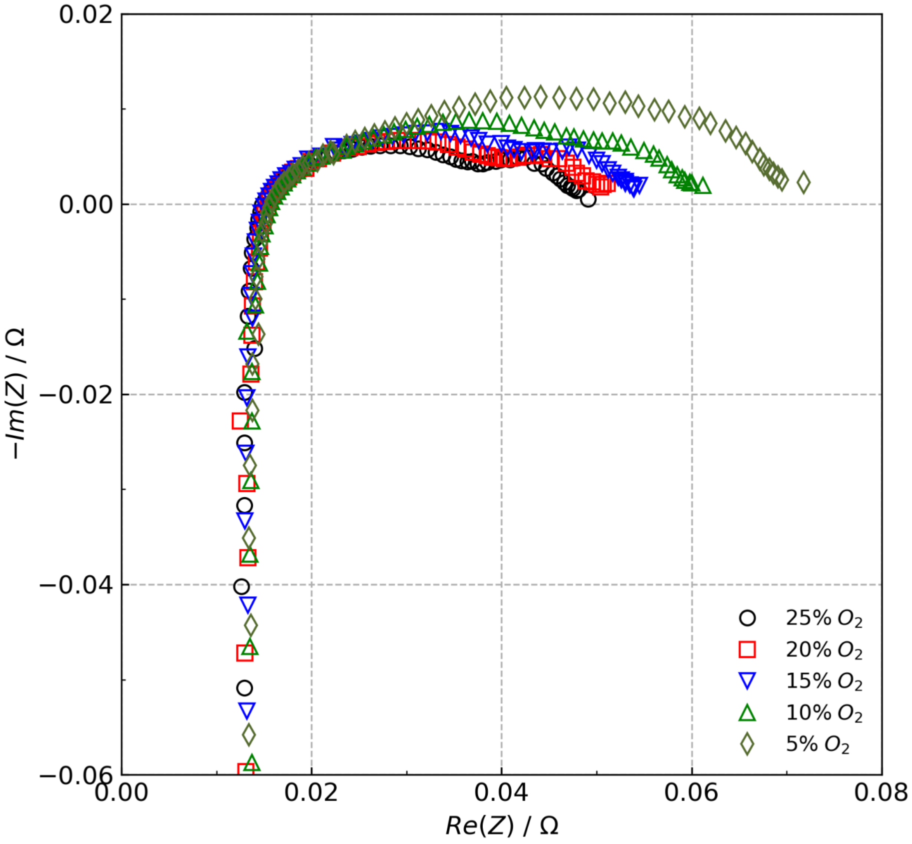

Figure 5.16. Electrochemical impedance spectra of the O_2 concentration effect in the oxygen electrode in OCV at 650 °C.

the oxygen electrode. Figure 5.17 shows the evolution of the reference condition, the time being counted from the point where the reversible operation started. There is a higher loss of performance during the last hours when lower partial pressures of carbon dioxide were tested. In general, fast degradation seems to occur with the low amounts of carbon dioxide present in the oxygen electrode during the second experimental campaign. The results of the second experimental campaign, the ones related to the reverse molten carbonate cell operation, seem to be contrary to the results of Hu et al. who tested button cells [46]. This could be explained because in a button cell, the phenomena occurring are approximately ideal, and uniform, contrary to single cells where the phenomena are influenced by the size, the geometry, surface distribution and higher polarization phenomena.

Moreover, it is important to consider that in electrolysis mode the amount of carbon dioxide and oxygen generated at the oxygen electrode increases with demand, and the amount of carbon dioxide double that of oxygen, as Eq. (2.1) indicates. Most industrial applications supply air to ensure sufficient content of oxygen when it is required in the process, hence, in the case of electrolysis mode, the amount of air should be adjusted to demand, ensuring a low partial pressure of carbon dioxide, or a high p_{O_2}/p_{CO_2} ratio at the oxygen electrode. Based on that, it is recommended to supply a gas mixture of air with around 5 % of carbon dioxide, having a p_{O_2}/p_{CO_2} ratio close to 4, regulating this amount at high current densities where more carbon dioxide is going to be forming.

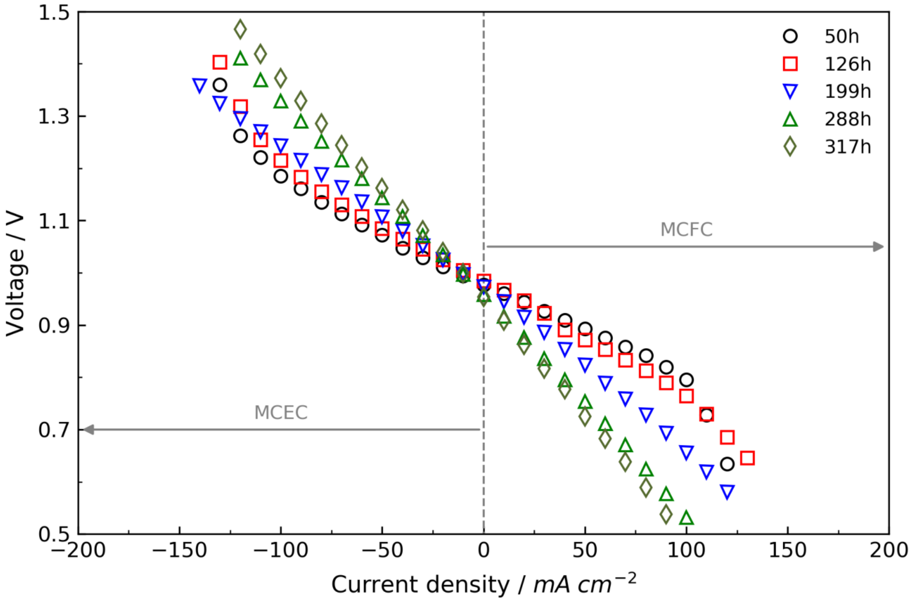

Figure 5.17. Experimental evolution of the reference condition in reversible mode of operation.

To compensate the effect of loss of electrolyte, in-operation refilling has been attempted at the end of the second experimental campaign. To do this a joint was connected to the inlet of the oxygen electrode to supply electrolyte during the operation. The first attempt consisted in adding electrolyte periodically by amounts of 2 g to 4 g in OCV waiting until a steady voltage was reached. Expecting an increase in the OCV, in total 20 g of electrolyte were supplied, however, the improvement was minimal, as can be observed in Figure 5.18 by curve C_3, where the low frequency semicircle related with the diffusive phenomena is forming again. At that moment, the amount of electrolyte added was relatively high, approximately twice the initial amount used in the set-up, and it was presumed that the extra electrolyte was flowing out from the cell carried by the gases or accumulated without reaching the cell. Therefore, the cell was left under a low current of 0.8 A for 24 h allowing the electrolyte to reach the active site. Nevertheless, this resulted in a small decrease in the internal resistance like curve C_4 shows. In the third attempt, 7 g of electrolyte were added under a load of 0.8 A, then the cell was left under 2.4 A for 24 h, curve C_5 shows how the internal resistance and the high frequency region were brought back close to the initial condition. The internal resistance presented a decrease and the difference with curve C_1 is only $1.3 \times 10^{-3}\,\Omega$, representing a difference of only 20.63 %, which means a recovery of 144.1 % of the internal resistance. The last attempt was carried out adding 4 g more of electrolyte expecting to reduce the low frequency region, nevertheless, the cell was flooded with electrolyte, that reduces the internal resistance and increases the concentration polarization region as C_6 shows. When the cell was unassembled, 22.5 g of electrolyte was stacked inside the cell, i.e. 68.2 % of the total supplied. An undesired effect of the agglomerated electrolyte was the high level of corrosion encountered, visible with the naked eye in the current collectors, mainly the oxygen electrode current collector.

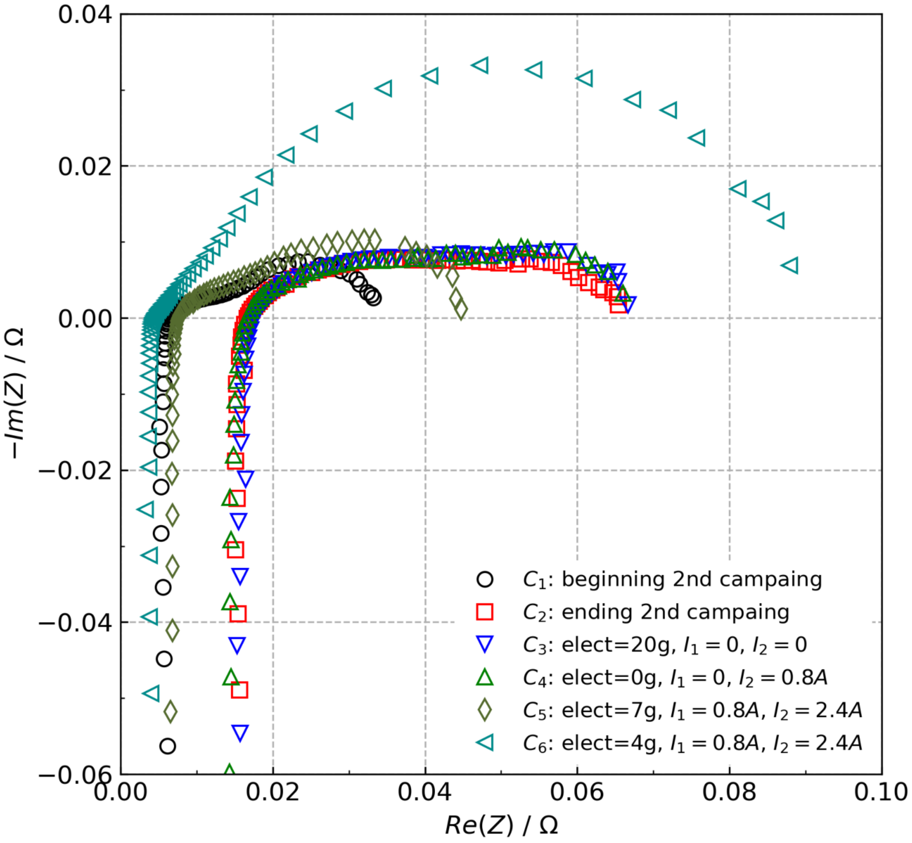

Figure 5.18. EIS showing the effect of electrolyte refilling in operation.

5.2. Experimental and numerical results in fuel cell mode

5.2.1. Experimental results in fuel cell mode.

The experimental campaign described in Table 3.2 consisted of getting data that is used in the fitting of a numerical model. The parameters that have been tested are temperature, hydrogen content in the fuel electrode, and carbon dioxide in the oxygen electrode, whose results are presented in Figure 5.19a, Figure 5.19b and Figure 5.19c, respectively.

Figure 5.19a shows the polarization curve of the cell as a function of temperature, these results show that when the cell increases the temperature it has a better performance. This fact is due to the decrease of activation voltage losses when temperature is increased. However, the increment in the cell temperature could not be totally beneficial because at higher temperatures, the corrosion in the cell is increased and the operational time could be decreased significantly. Thus, Figure 5.19a shows a few differences between 650 °C and 680 °C, where the curves are almost overlaid, in contrast with a higher gap present between polarization curves at cell operating temperatures of 650 °C and 620 °C .

The hydrogen content was tested from 50 % to 70 %, however, the polarization curves do not show a significant difference between them as Figure 5.19b shows. Thus, the difference in voltage at 100 mA/cm^2, between 50 % and 70 % of hydrogen, corresponds to 0.027 V.

Besides, carbon dioxide was tested from 4 % to 20 % in the oxygen electrode side. The results indicate a higher adverse effect on the performance when it is decreasing, as Figure 5.19c shows. Thus, a lack of carbon dioxide in the oxygen electrode causes a drop of voltage produced by the increase in polarization losses. It can be observed evaluating the difference in voltage at 100 mA/cm^2, between 4 % and 20 % of carbon dioxide concentration, which corresponds to 0.188 V.

It is well known that internal electrical resistance is a function of temperature. Figure 5.20 shows the Electrochemical Impedance Spectra (EIS) of the cell operated at the reference composition and at different operating temperatures. The intersection of the small semicircle in the curve with the horizontal axis represents the internal resistance of the cell. The internal resistance tends to decrease with the rise in temperature, it is because the resistance of materials to the flow of electrical current is inversely proportional to the increase in temperature. This performance can be observed graphically in Figure 5.20 and numerically in Table 5.1.

Table 5.1. Internal electrical resistance of the cell as a function of temperature.

Temperature [°C]	R_i [Ω]	$R"_i$ [$\Omega\,\mathrm{cm}^2$]
620	6.068×10^{-3}	4.854×10^{-1}
650	5.829×10^{-3}	4.663×10^{-1}
680	4.988×10^{-3}	3.991×10^{-1}

5.2.2. Zero-dimensional MCFC models comparison

In this section, a comparison between the experimental results and five zero-dimensional models found in literature to calculate the overpotentials in MCFC is carried out. The main characteristics of the models and the equations description to determine the overpotentials have been given in section 2.5. Figure 5.21 shows the comparison of polarization curves of the models respect to the experimental data of run 1 from Table 5.2, i.e. the reference condition

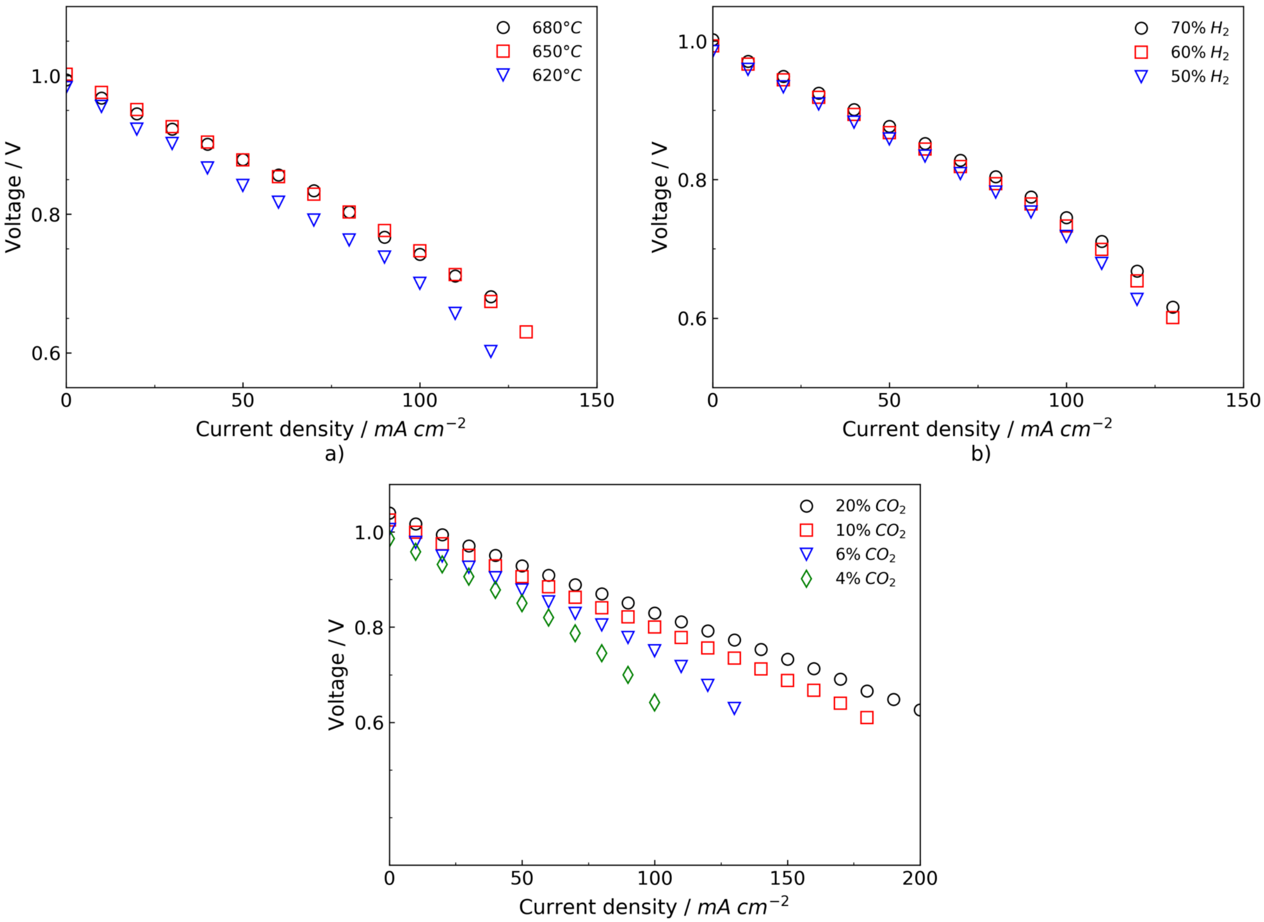

a) b) c)

Figure 5.19. Polarization curve as a function of: a) cell temperature at the reference composition, b) hydrogen content in the fuel electrode at 650 °C and c) carbon dioxide content in the oxygen electrode at 650 °C.

for the first experimental campaign; in general, all the models present a high deviation with respect to the experimental data.

The models were evaluated considering isothermal conditions. This difference is higher for Model 1, Model 2 and Model 4. Besides, Model 3 and Model 5 show a closer performance to the experimental curve. In Table 5.2, the voltage for experimental and numerical values using reference composition at 100 mA/cm^2 is shown. Thus, Model 5 is the one that best fits with experimental data at low and intermediate current densities considering the effect of the most important species involved in the performance of the cell, including: H_2, H_2O, CO_2 and O_2. On the other hand, Model 2 and Model 3 tend to predict the effect of limiting current density, because in these models this effect has been considered. Moreover, Model 5 was selected to be adjusted with experimental data based on its development [71], where few equations are required to correlate the performance of the cell, besides, its proximity with the experimental data.

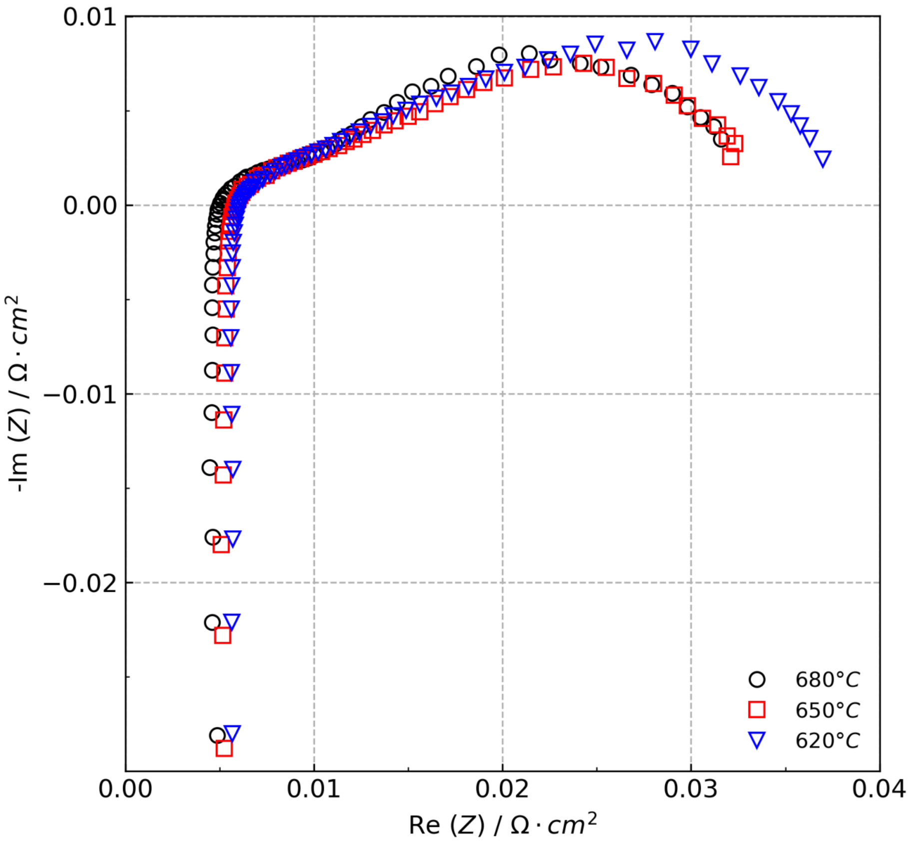

Figure 5.20. Electrochemical Impedance Spectrum as a function of the cell temperature at the reference composition. 18/11/7/0% $CO_2/H_2O/H_2/N_2$ in the fuel electrode, 6/12/82% $CO_2/O_2/N_2$ in the oxygen electrode.

Table 5.2. Experimental and numerical voltage using reference composition at 100 mA/cm^2.

	Voltage [V]
Experimental	0.747
Model 1	0.8796
Model 2	0.8721
Model 3	0.8418
Model 4	0.8652
Model 5	0.8322

5.2.3. Parameter identification and model validation in fuel cell mode

The numerical polarization curve of Model 5 in Figure 5.21 was obtained evaluating the Nernst voltage and subtracting the overpotentials which are calculated at different current densities. The overpotentials include the ohmic, activation and concentration losses. Thus, the constants of Model 5, section 2.5.5, should be checked with the experimental data of the overpotentials and decide which ones should be recalculated. Below are presented the

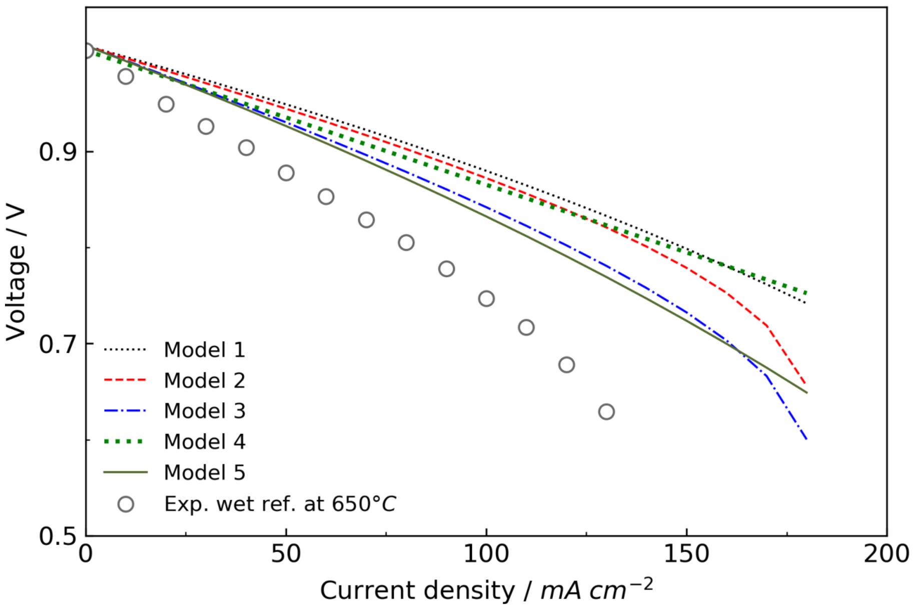

Figure 5.21. Polarization curve comparing the experimental data with the numerical models at the reference condition. 18/11/7/0% $CO_2/H_2O/H_2/N_2$ in the fuel electrode, 6/12/82% $CO_2/O_2/N_2$ in the oxygen electrode at 650 °C.

experimental overpotentials as well as the recalculated constants that adjust Model 5 with the experimental data.

The experimental trend of the total overpotentials as a function of current density are shown in Figure 5.22a, Figure 5.22b and Figure 5.22c for the cell temperature, hydrogen content effect in the fuel electrode and carbon dioxide content effect in the oxygen electrode, respectively. These overpotentials represent the voltage difference between the Nernst voltage, considering the experimental voltage at OCV, and the experimental voltage measured at any other current density value.

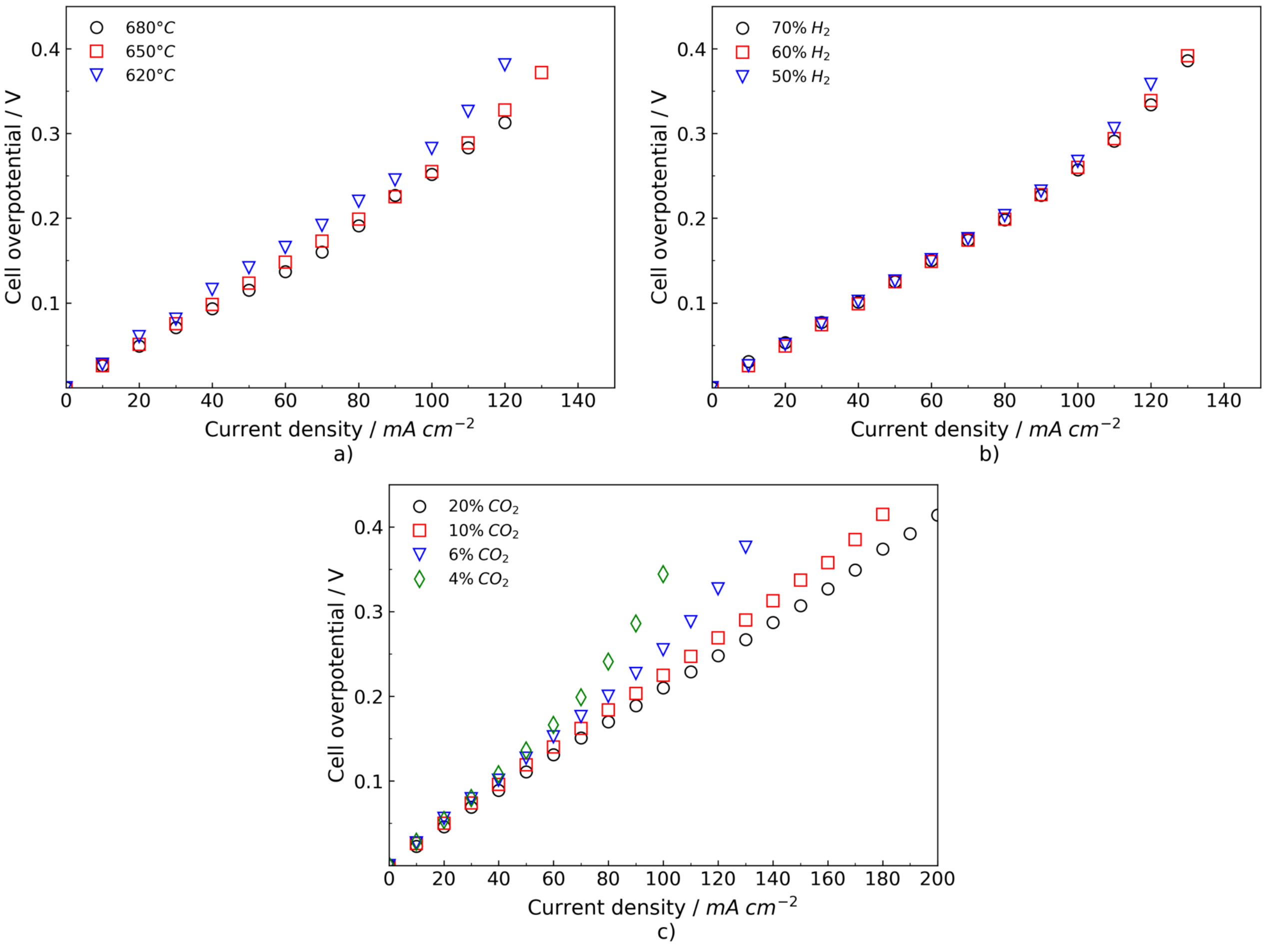

Figure 5.22. Total overpotentials as a function of: a) cell temperature at the reference composition, b) hydrogen content in the fuel electrode at 650 °C and c) carbon dioxide content in the oxygen electrode at 650 °C.

Numerical and experimental ohmic losses have been checked comparing the results of Eq. (2.31) with data of Table 5.1. The results show a good agreement between them. Thus, constants of Eq. (2.31) are left as defined. Then, ohmic losses are removed from the overall overpotentials to get only the ones related to polarization losses. Thus, it is assumed that Eq. (2.32), Eq. (2.33) and Eq. (2.34) correlate the activation losses and the equations presented in section 4.3.1 are added to consider the concentration losses. The experimental corrected overpotentials, i.e without the ohmic losses, are presented in Figure 5.23a, Figure 5.23b and Figure 5.23c as function of cell temperature, hydrogen content effect in the fuel electrode and carbon dioxide content effect in the oxygen electrode, respectively.

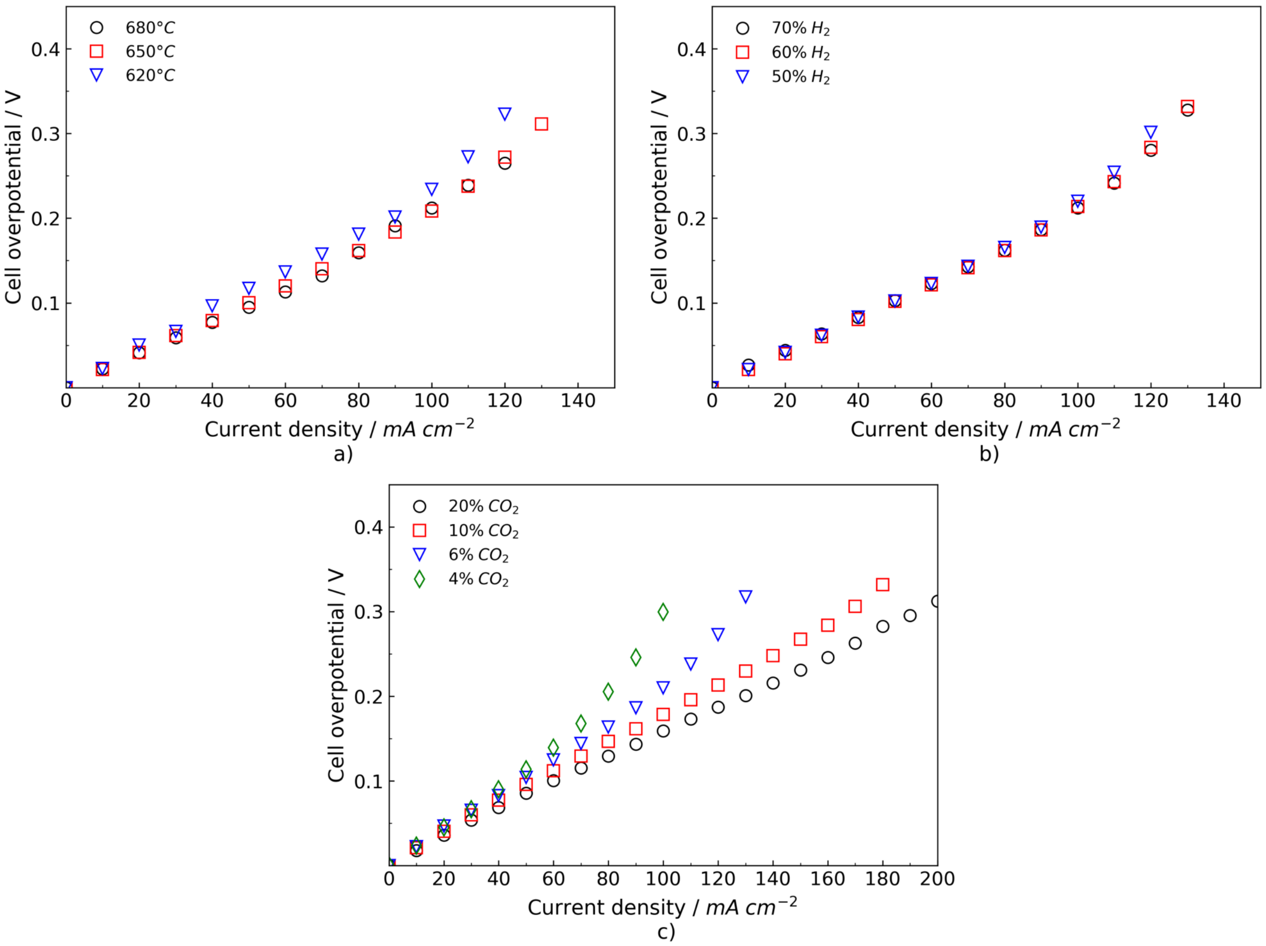

Figure 5.23. Polarization overpotentials as a function of: a) cell temperature at the reference composition, b) hydrogen content in the fuel electrode at 650 °C and c) carbon dioxide content in the oxygen electrode at 650 °C.

The recalculated constants were P_3, P_5 and P_7 from Model 5 because these parameters are associated to polarization losses, which could characterize the different hardware and components used in this study compared to [73]. The polarization losses presented in Figure 5.23 were initially assigned to the voltage losses expressed in Model 5 for both the fuel electrode and oxygen electrode involved in these constants. These parameters are a good prediction for the activation overpotentials, however do not represent completely the concentration losses. In order to improve the fitting, the experimental polarization values were replaced in a set of equations including Eq. (2.32), Eq. (2.33), Eq. (2.34), Eq. (4.30) and Eq. (4.31), all of them reflecting the polarization voltage losses, resulting in a set of equations that was solved simultaneously in order to know the value of the constants.

The new values obtained for the constants are presented in Table 5.3. The results indicate that there is an increment of almost 50 %, 100 %, and 37 % for P_3, P_5 and P_7, respectively, compared with those presented in [73]. This increment could be caused by differences in materials, geometry, flow pattern, etc. Figure 5.24 shows the polarization curves comparing the experimental data with the numerical models including the fitted model at the reference condition of fuel cell mode. The results show a good agreement with the experimental results, besides, there is a good prediction of the limiting current density..

Table 5.3. Coefficients adjusted for Model 5.

Coefficient	Value	Units
P_3	4.8918×10^{-6}	$\Omega\,\mathrm{cm}^2\,\mathrm{K}^{-1}\,\mathrm{atm}$
P_5	9.0366×10^{-9}	$\Omega\,\mathrm{cm}^2\,\mathrm{K}^{-1}\,\mathrm{atm}^{0.25}$
P_7	4.6827×10^{-9}	$\Omega\,\mathrm{cm}^2\,\mathrm{K}^{-1}\,\mathrm{atm}$

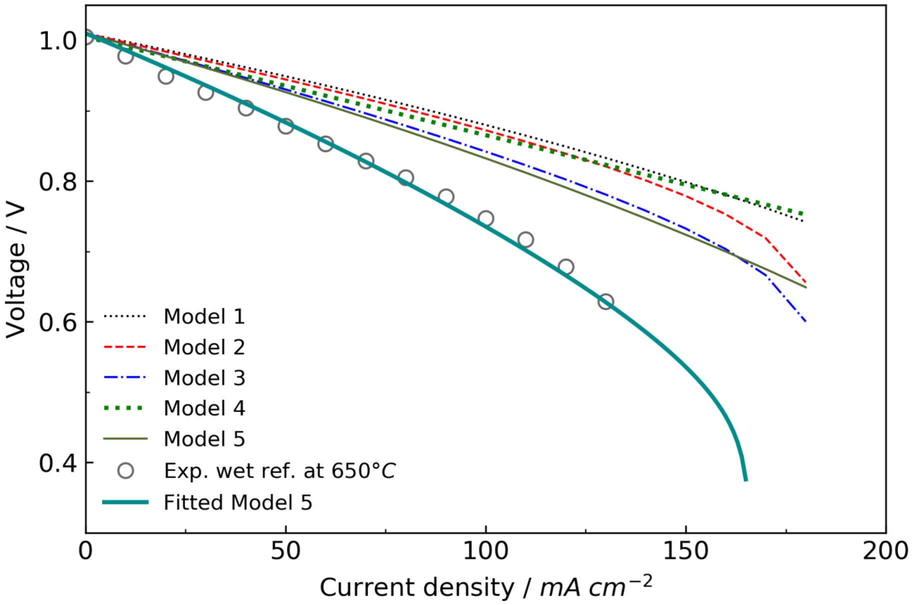

Figure 5.24. Polarization curves comparing the experimental data with the numerical models including the fitted model at the reference condition, whose composition in the fuel electrode is 18/11/71/0% $CO_2/H_2O/H_2/N_2$, 6/12/82% in $CO_2/O_2/N_2$ in the oxygen electrode at 650 °C.

Figure 5.25 presents a complete comparison between the data of the first experimental campaign (Table 3.2), Model 5, and fitted Model 5. The results show a good correlation between the experimental curves and the numerical curves of fitted Model 5, including the limiting current densities, getting and average percentage error of 0.97 % between the measured and simulated data. These results give some reliability on the use of the fitted Model 5 in conditions that have not been considered in the development, i.e. electrolysis mode.

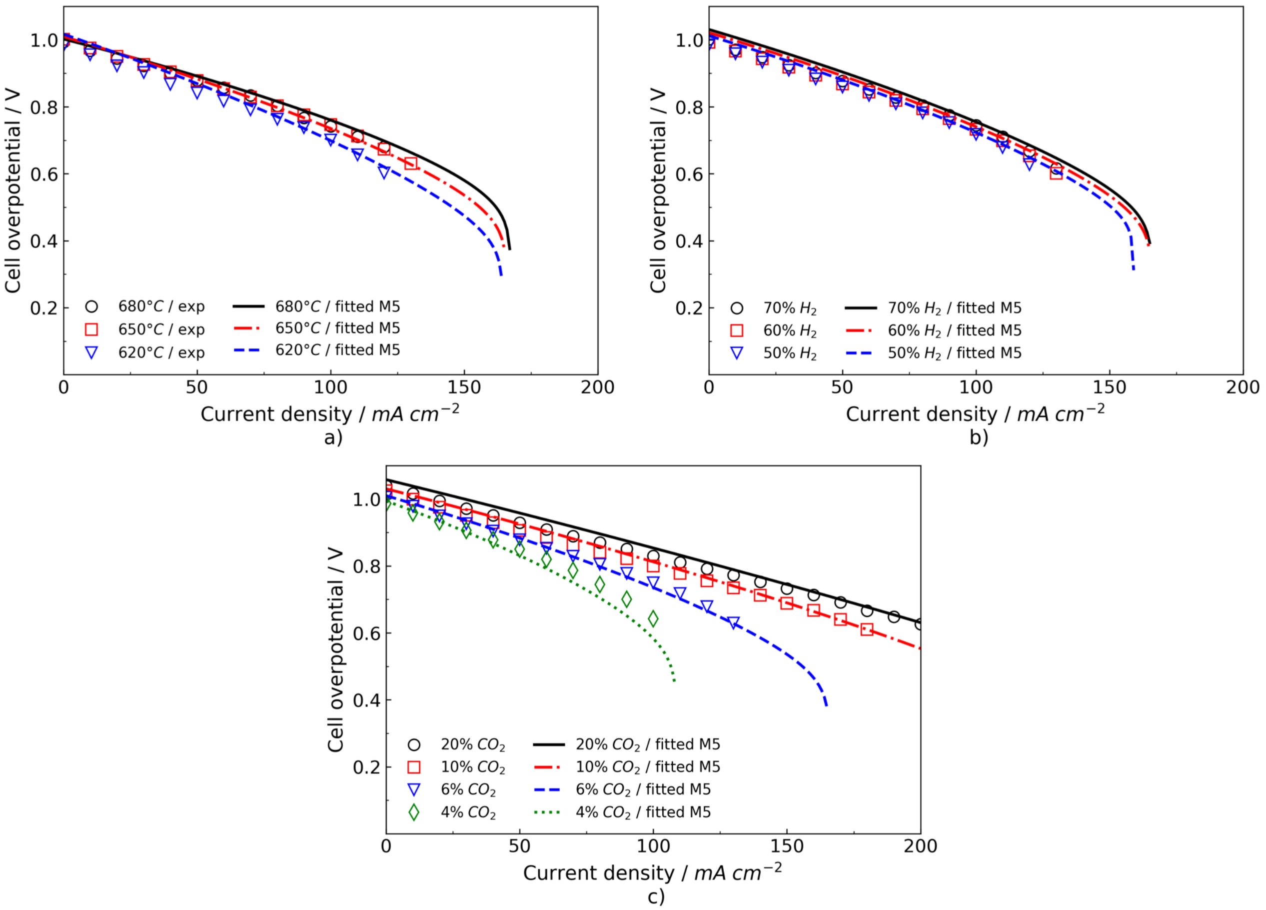

Figure 5.25. Polarization curves comparing the experimental data of the first experimental campaign and the fitted Model 5 for: a) temperature effect, b) hydrogen content in the fuel electrode, and c) carbon dioxide content in the oxygen electrode.

5.3. Numerical results in reversible cell mode

In this section the conditions of the reversible MCFC operation are evaluated numerically. Thus, the fitted Model 5 is applied to both fuel cell and electrolysis mode to predict numerically the performance of the cell operating in reversible mode. The program code was written in Anaconda Python 3.7. The code is presented in appendix B

The experimental results presented in section 5.1 indicate that there is some degradation in the cell during the reversible operation. Thus, a numerical and experimental representative comparison of only four cases is carried out. These cases were selected because they were performed in the first hours of single cell operation and it is probably that they present a small amount of degradation letting make a better comparison. The comparison is presented in Figure 5.26 which represents the cases 2, 7, 10 and 12, related to the fuel electrode composition of 25/25/25/25% $CO_2/H_2O/H_2/N_2$, 50/25/25/0% $CO_2/H_2O/H_2/N_2$, 25/50/25/0% $CO_2/H_2O/H_2/N_2$, and 25/25/5/45% $CO_2/H_2O/H_2/N_2$, respectively. Figure 5.26 shows that in fuel cell mode almost all the cases are well predicted, nevertheless at high current densities the difference is increased. In electrolysis mode the prediction of the performance is considered acceptable. It is important to mention that the numerical prediction of the cell, where several coupled phenomena are occurring at the same time, is being calculated using a zero-dimensional model at isothermal conditions giving in general a good correlation with the experimental results. The numerical results for the MCFC single cell operating in reversible mode are presented below.

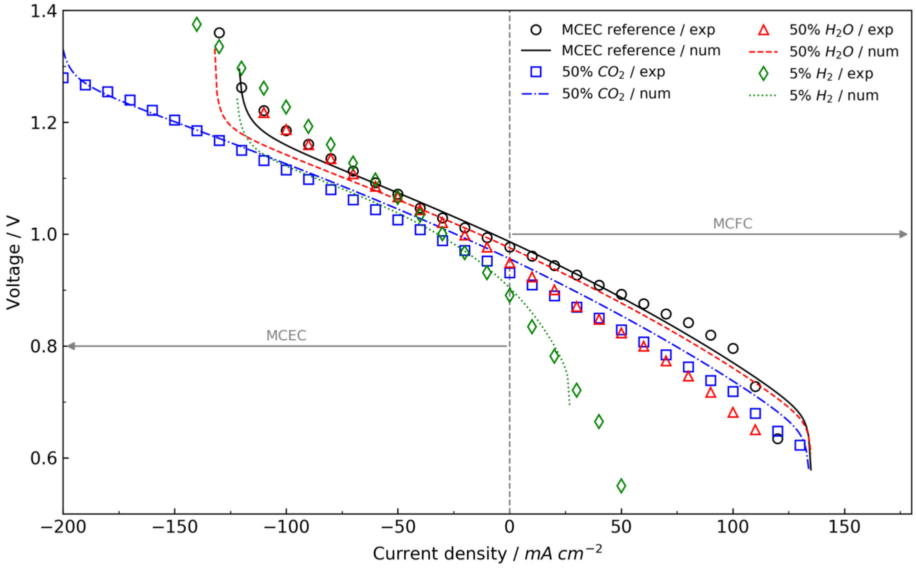

Figure 5.26. Experimental and numerical comparison of the single cell operating in reversible mode.

5.3.1. Effect of cell temperature

Figure 5.27 shows the cell temperature effect from 570 °C to 650 °C, at reference condition for reversible operation mode. In this case, the cell performance, in both operative modes, is getting worse when the cell temperature decreases causing an increment in the cell overpotentials. The numerical polarization curves have the same trend with the experimental curves, although the experimental results were affected by the degradation of the cell presenting higher voltage losses. Besides, from the numerical curves a common limiting current density point for fuel cell mode and one for electrolysis mode is observed. This can be explained because the limiting current density depends on the amount of species in every electrode, and since there are no changes in fed composition for any current, these are going to have the same limiting point for every case. In these cases the polarization curves present a symmetrical point, close to 140 mA/cm^2.

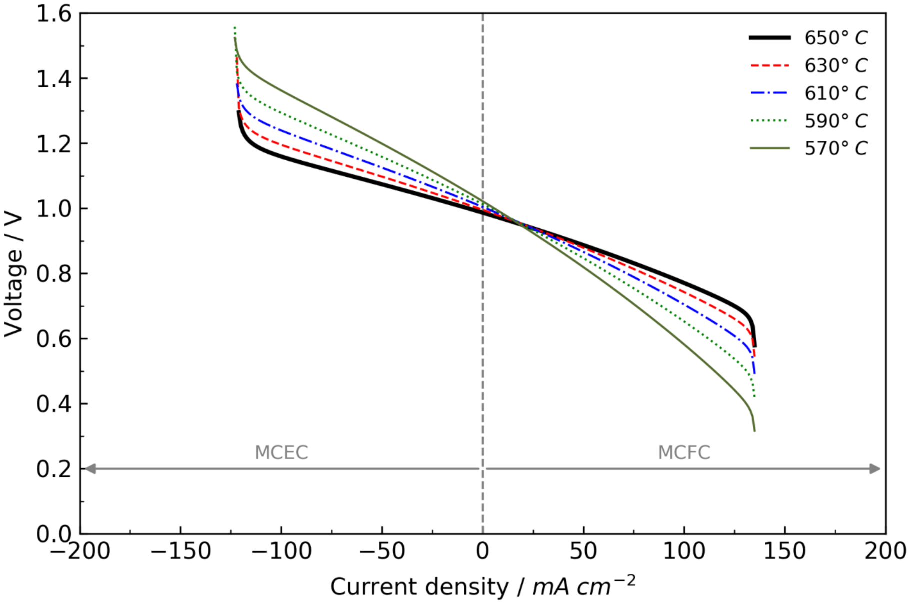

Figure 5.27. Numerical prediction of cell temperature on the single cell voltage operating in reversible mode.

5.3.2. Effect of Electrodes flow ratio

The effect of electrodes flow ratio has a negligible numerical effect in the performance of the cell as Figure 5.28 shows. This negligible effect on the cell performance is due to the fact that the model considers the reactions and overpotentials at isothermal conditions. That did not happen in the experimental results shown in Figure 5.5, where increasing the EFR causes a small rise in the performance due to a cooling effect on the cell.

5.3.3. Effect of fuel electrode gas composition

The effect of carbon dioxide, water and hydrogen concentration in the fuel electrode is presented in Figure 5.29, Figure 5.30 and Figure 5.31, respectively.

Firstly, in electrolysis mode diminishing the content of carbon dioxide causes an increment in the overpotentials, reducing significantly the limiting current as Figure 5.29 shows, affecting in this way the performance of the cell. However, the performance in fuel cell mode tends to improve when carbon dioxide content is reduced, though the effect is less evident than in electrolysis mode.

Analyzing the effect of water in the fuel electrode, shown in Figure 5.30, it is found that when it is reduced in electrolysis mode the performance gets worse, though not so much like in the case of carbon dioxide where the limiting current density changed noticeably. In fuel cell mode the water effect on the performance is similar like the one caused by carbon dioxide, it was improved when the content of water was reduced. Since carbon dioxide and water are

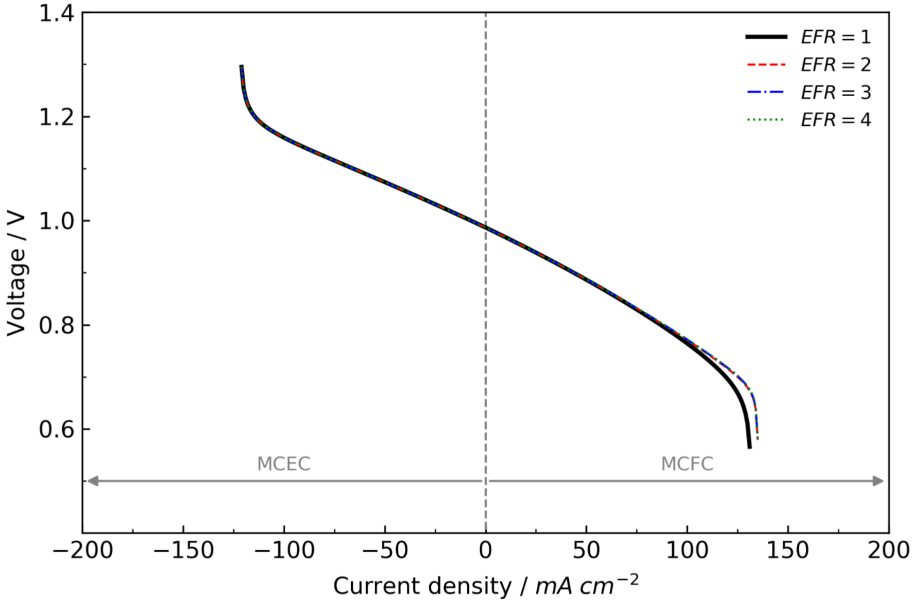

Figure 5.28. Numerical prediction of EFR effect on the single cell voltage operating in reversible mode.

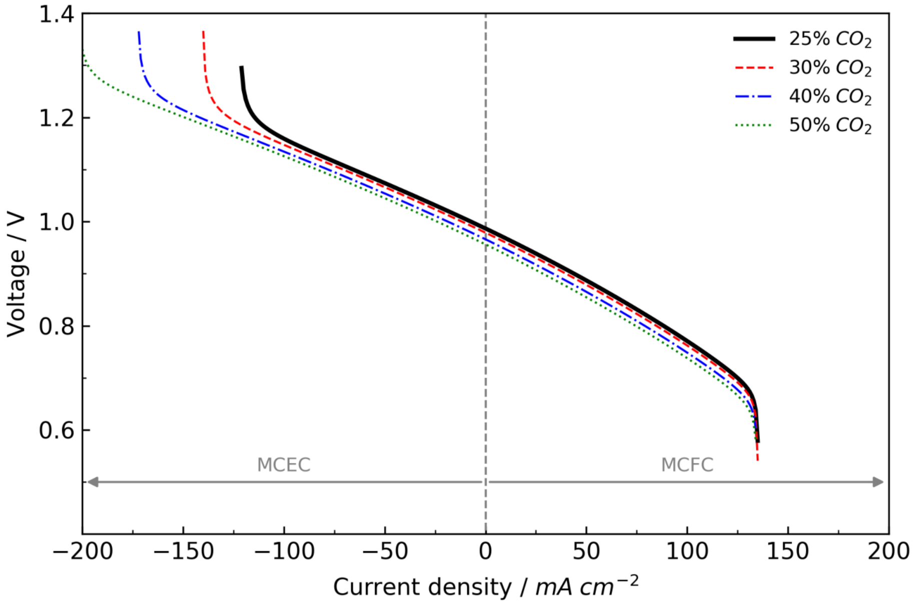

Figure 5.29. Numerical prediction of carbon dioxide effect in the fuel electrode on the cell voltage operating in reversible mode.

the reactant species involved in the electrochemical process in electrolysis mode, the amount of these species determines the limiting current densities, as can be seen in Figure 5.29 and Figure 5.30. The opposite happens in fuel cell mode where these species are the products of the electrochemical reaction, thus the limiting current density it is not affected by changes in composition of these species.

Finally, the effect of hydrogen content in the fuel electrode is presented in Figure 5.31.

In this case, when the content of hydrogen is reduced in electrolysis mode, the three cases converge to the same limiting current density because in this operative mode carbon dioxide and water are the species limiting the performance of the cell. Therefore, the hydrogen content in the mixture affects only the open circuit voltage, decreasing its value with the hydrogen concentration reduction. However, in fuel cell mode where the cell consumes hydrogen to operate, if hydrogen content is reduced, the limiting current density reduces dramatically.

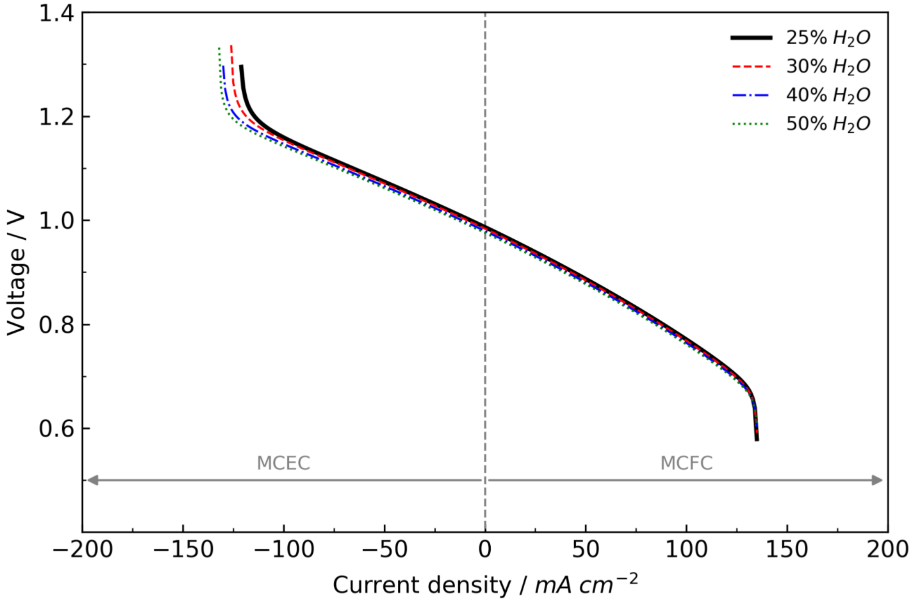

Figure 5.30. Numerical prediction of water effect in the fuel electrode on the cell voltage operating in reversible mode.

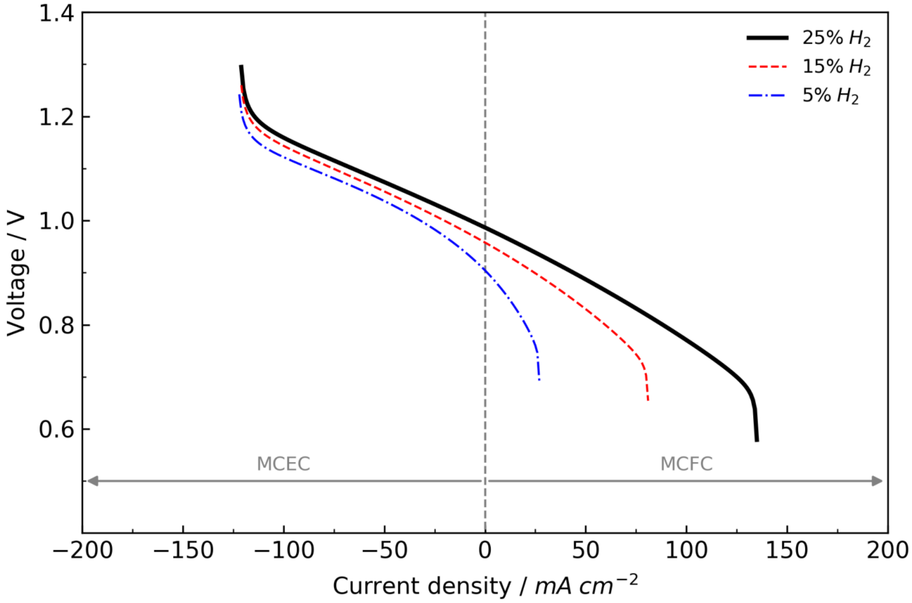

Figure 5.31. Numerical prediction of hydrogen effect in the fuel electrode on the cell voltage operating in reversible mode.

The numerical results of the carbon dioxide, water and hydrogen content in the fuel electrode can be compared with the experimental results presented in Figure 5.7, Figure 5.9 and Figure 5.11, respectively. It can be observed that in all the cases the tendency is similar with the experimental results and the performance of the cell can be predicted, even when the equation for the overpotentials in the fuel electrode considers only the effect of hydrogen, Eq. (2.34). The effect of carbon dioxide and water are considered chemically in Eq. (4.5) and Eq. (4.13) for fuel cell and electrolysis mode, respectively.

5.3.4. Effect of oxygen electrode gas composition

The effect of carbon dioxide and oxygen content in the oxygen electrode is presented in Figure 5.32 and Figure 5.33, respectively.

The increase in carbon dioxide content in the oxygen electrode in electrolysis mode decreases the performance as Figure 5.32 shows. However, at high current densities when carbon dioxide increases in the oxygen electrode, the effect is diminished. Contrary, in fuel cell mode, when the content of carbon dioxide decreases in the oxygen electrode, it causes the performance to get worse by diminishing dramatically the limiting current density, as well as an increase in the voltage losses.

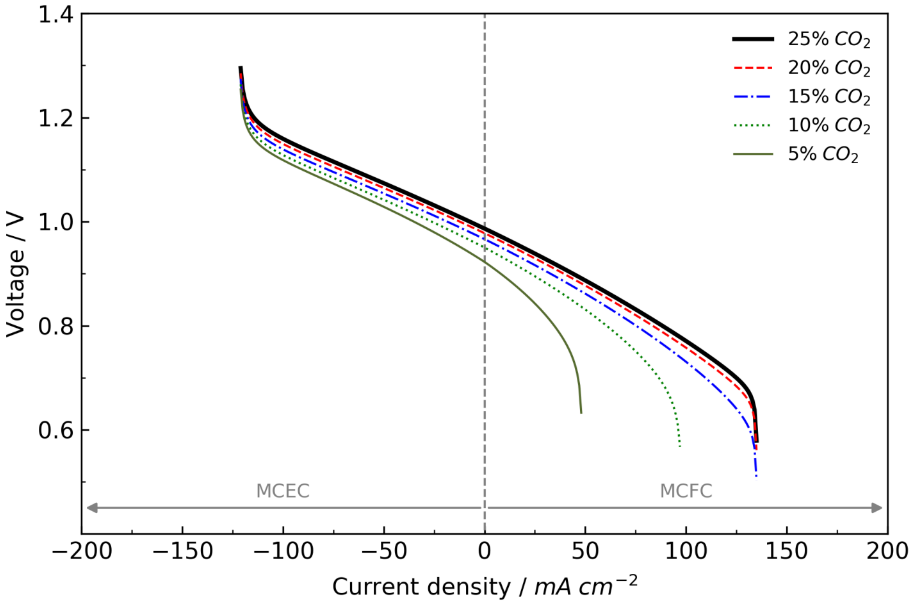

Figure 5.32. Numerical prediction of carbon dioxide effect in the oxygen electrode on the cell voltage operating in reversible mode.

Figure 5.33 shows the effect of oxygen content in the oxygen electrode. The effect of increase the oxygen content in electrolysis mode causes an improvement on the performance as well as in fuel cell mode. Reducing the oxygen content in fuel cell mode, decreases the limiting current density as well as the performance. As in the case of the fuel electrode, the reduction in the reagent species causes a reduction in the limiting current density. This tendency can be observed for the oxygen electrode in fuel cell mode where oxygen and carbon dioxide are reactants in the electrochemical reaction. Contrary, the limiting current density is not affected by changes of this species in electrolysis mode where the species is a product.

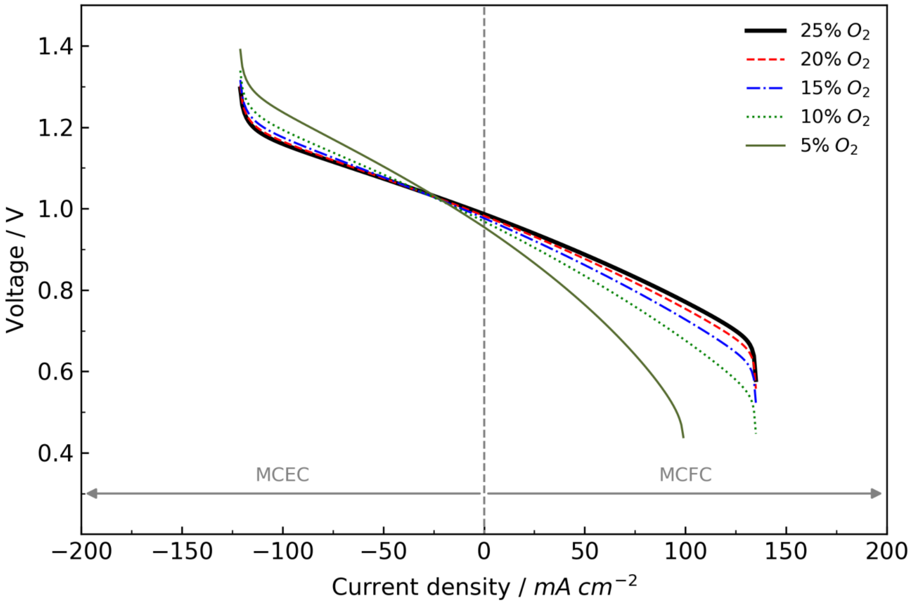

Figure 5.33. Numerical prediction of oxygen effect in the oxygen electrode on the cell voltage operating in reversible mode.

The numerical effect of carbon dioxide and oxygen can be compared with the experimental results presented in Figure 5.13 and Figure 5.15, respectively. In both cases the general performance on the oxygen electrode is predicted giving a comprehension of what effect is expected when composition is varied.

Below, the numerical results of the reference case for the cell operating in reversible mode to analyze the changes in voltage losses, heat transfer, efficiency and species consumption, is presented.

5.3.5. Voltage losses

Figure 5.34 shows the ohmic, activation and concentration losses in all the operation range of the cell at the reference condition. Ohmic losses are calculated using Eq. (2.31) and considering that internal resistance does not change in all the operative range, that is because the model is at constant cell temperature without degradation effect. It is possible to notice a symmetric effect of the ohmic overpotentials. Activation losses are calculated using Eq. (2.32) and Eq. (2.33) for oxygen electrode and Eq. (2.34) for fuel electrode, considering that these equations apply for both operation modes, it is assumed that activation energy remains constant in both operation modes. However, concentration losses do not present a quantitative symmetric shape because different species are being consumed, i.e., hydrogen in fuel cell mode and water and carbon dioxide in electrolysis mode, affecting in this way the diffusion of species which causes different overpotentials.

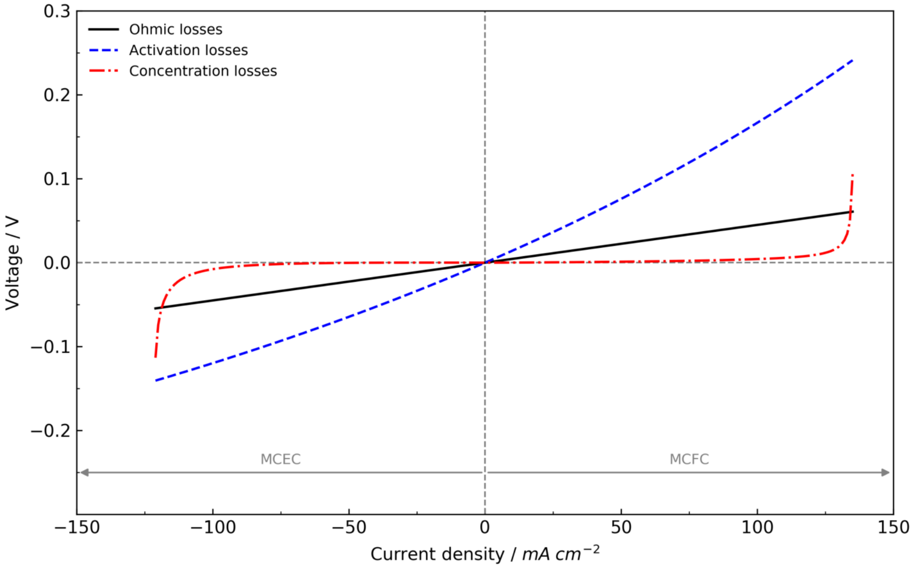

Figure 5.34. Numerical prediction of voltage losses of the cell operating in reversible mode at reference condition. Fuel electrode gas composition of 25/25/25/25% $CO_2/H_2O/H_2/N_2$, oxygen electrode gas composition of 25/25/50% $CO_2/O_2/N_2$, at 650 °C.

5.3.6. Thermo-neutral voltage

Thermo-neutral voltage is an important operative point in steam electrolyzers because it could avoid the waste of energy, and represents a point in electrolysis mode that does not require to add or remove heat. If the operation of an electrolyzer passes the thermo-neutral voltage, the heat produced by electric heating is going to be greater than the heat required by the reaction, causing a rise in the temperature if the heat is not removed from the system. On the contrary, if the electrolyzer is operated below the thermo-neutral voltage, the heat produced by electric heating is smaller than the heat required by the reaction causing a decrease in the temperature of the cell if the heat required by the system is not supplied. This effect can be noticed experimentally if the cell temperature is tracked during the operation. When the electrolyzer operates between open circuit voltage and the thermo-neutral voltage, the cell temperature tends to decrease because the cell requires more heat than the one being supplied. Contrary, the temperature begins to rise once the thermo-neutral voltage is passed.

The thermo-neutral voltage can be determined numerically by a heat transfer diagram, localizing the intersection of the net heat transfer rate with the horizontal axis as Figure 5.35 shows. Besides, Figure 5.36 shows the relationship between cell temperature and heat transfer rate in the reversible mode of operation, moreover indicating that the thermo-neutral voltage can be related experimentally with the cell temperature.

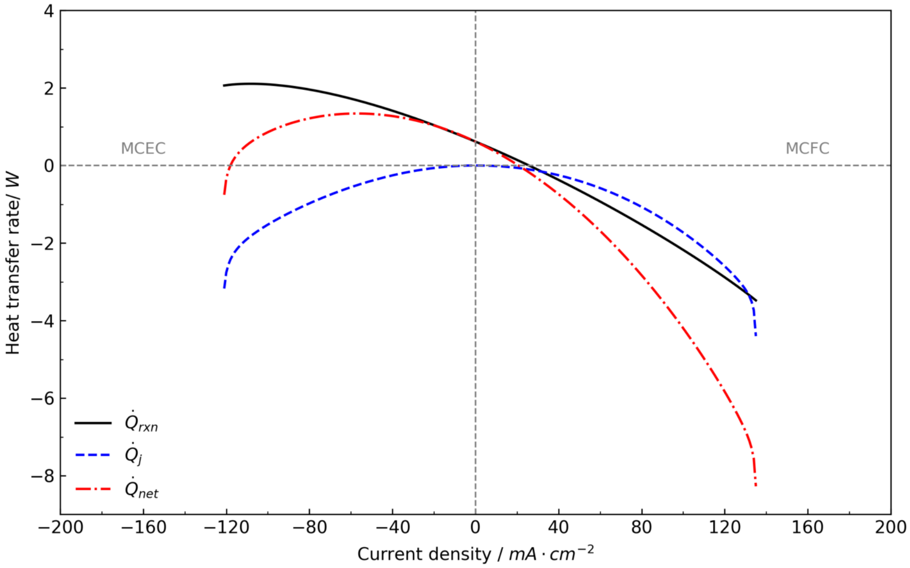

Figure 5.35. Numerical heat transfer rate of the cell operating in reversible mode at reference condition. Fuel electrode gas composition of 25/25/25/25% $CO_2/H_2O/H_2/N_2$, oxygen electrode gas composition of 25/25/50% $CO_2/O_2/N_2$, at 650 °C.

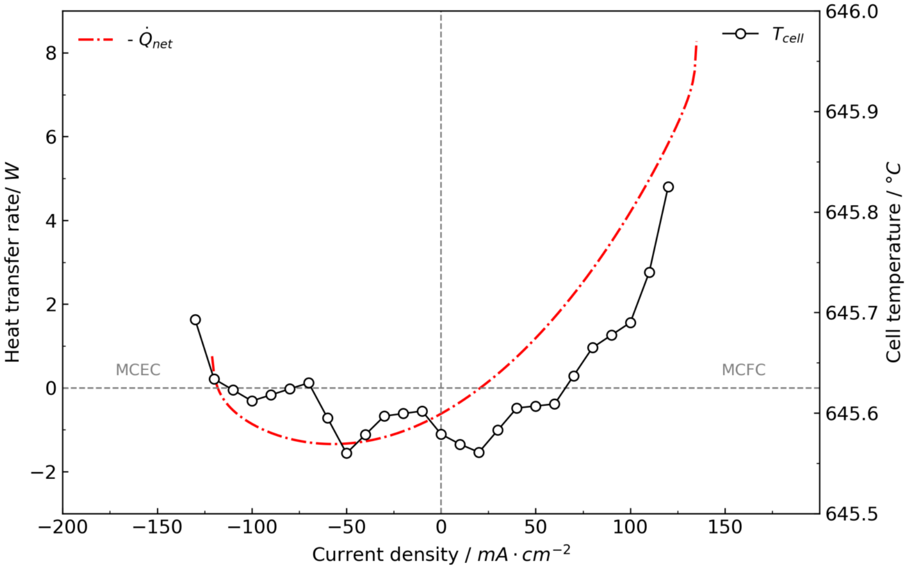

Figure 5.36. Relationship between cell temperature and net heat transfer rate in reversible mode operation, with the fuel electrode gas composition of 25/25/25/25% $CO_2/H_2O/H_2/N_2$, oxygen electrode gas composition of 25/25/50% $CO_2/O_2/N_2$, and EFR ratio of 4 at 650 °C.

Figure 5.35 shows the heat transfer rate diagram including: a) the heat transfer rate involved in the reaction ($\dot{Q}_{rxn}$), b) the heat transfer rate associated to the voltage losses ($\dot{Q}_j$), and c) the net heat transfer rate ($\dot{Q}_{net}$). The heat transfer rate involved in the reactions is calculated using Eq. (4.36) and Eq. (4.37), omitting $\dot{Q}_j$ which is associated to heat transfer due to voltage losses. Thus, the heat transfer rate involved in the reaction represents the rate of entropy generated in the process that is being converted into heat. The negative sign of this heat indicates that in fuel cell is exothermic, contrary to the electrolysis process that is endothermic.

On the other hand, the heat transfer rate associated to the voltage losses, calculated using Eq. (4.38), represents the conversion into heat of the ohmic, activation and concentration overpotentials, being negative for all the operative range. The net amount of heat transfer indicates the quantity required to be supplied or to be removed to or from the system, in order to maintain the cell temperature constant.

5.3.7. Efficiency

In this part the thermal efficiency using the second law of thermodynamics is calculated and presented in Figure 5.37. It is not convenient to express the thermal efficiency of the cell in terms of the first law because it does not provide a true criteria to measure the irreversibilities within the system, since not all of the energy released by the reaction within the cell may be converted to useful work without violating the second law of thermodynamcis. Furthermore, the thermal efficiency in terms of the first law can be greater than 100 % in cases where the entropy change for the overall reaction occurring within the cell is positive [89]. Thus, the first law efficiency of the cell is not considering in this work.

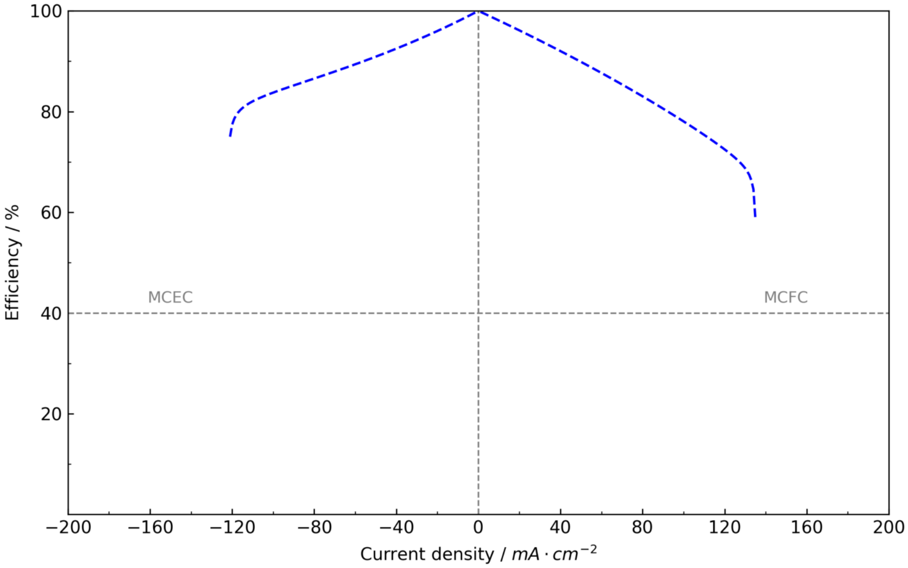

Figure 5.37. Numerical second law efficiency of the cell operating in reversible mode at reference condition. Fuel electrode gas composition of 25/25/25/25% $CO_2/H_2O/H_2/N_2$, oxygen electrode gas composition of 25/25/50% $CO_2/O_2/N_2$, at 650 °C.

The second-law efficiency can reach 100 % only in the limit of a reversible process and it will always be <100 % whether the entropy change for the reaction is positive or negative.

Furthermore, it accounts for the quality of thermal energy added to or removed from the system, thus, it provides a more consistent way of comparing different types of electrochemical devices [89]. Figure 5.37 shows the second-law efficiency in fuel cell and electrolysis mode, it can be observed that in both cases the efficiency is lower than 100 %. The lowest calculated efficiencies in electrolysis mode and fuel cell mode are 75 % and 58 %, respecetively. These are common values in electrochemical devices [87]. Moreover, it shows that the cell operates more efficiently in electrolysis mode that in fuel cell mode. In addition, it is suggested to use the second-law efficiency to compare the performance of the cell.

5.3.8. Water Gas-Shift Reaction effect

Figure 5.38 shows the carbon monoxide molar rate of reaction in the WGS reaction, $\dot{n}^r_{\mathrm{CO}}$, at reference condition in fuel cell mode and electrolysis mode, related to Eq. (2.6) and Eq. (4.10), respectively. In this case $\dot{n}^r_{\mathrm{CO}}$ is negative in both operative modes, it indicates that water gas-shift reaction is proceeding as Eq. (4.10) states, i.e. consuming hydrogen and carbon dioxide to produce water and carbon monoxide. In electrolysis mode this reaction is not totally desired when the objective of an electrolyzer is to produce hydrogen. Thus, special care should be given in the gas mixture supplied to promote a consumption of carbon monoxide in the water gas-shift reaction instead of consuming hydrogen to produce carbon monoxide. However, the results indicate that in all the range of operation in fuel cell mode, the reaction occurring is the reversed water gas-shift reaction, even in OCV.

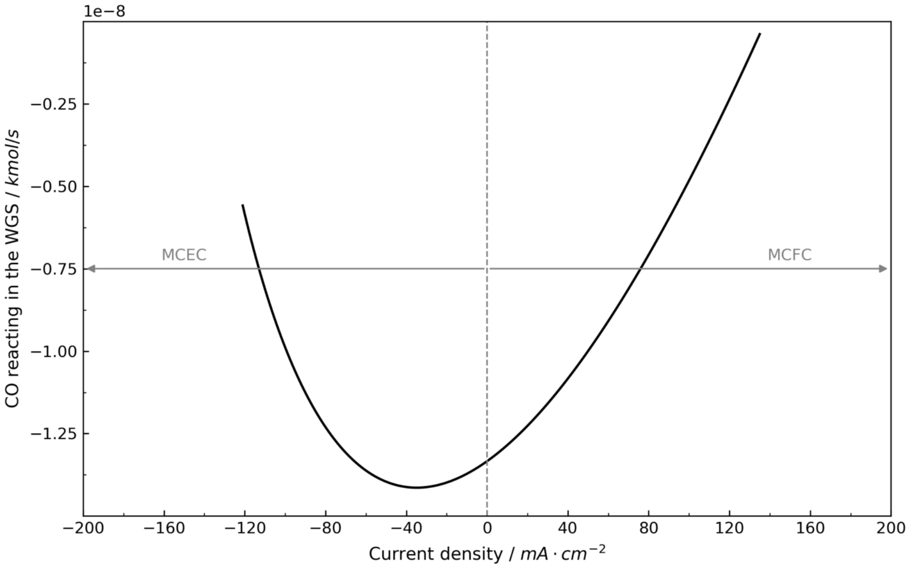

Figure 5.38. Numerical prediction of the rate of carbon monoxide reacting in the water gas shift reaction of the cell operating in reversible mode at reference condition. Fuel electrode gas composition of 25/25/25/25% $CO_2/H_2O/H_2/N_2$, oxygen electrode gas composition of 25/25/50% $CO_2/O_2/N_2$, at 650 °C.

5.3.9. Gas composition evolution

Figure 5.39 and Figure 5.40 show the species mole fraction when the cell operates in reversible mode for the fuel electrode and the oxygen electrode, respectively. The species progress in the fuel electrode is shown in Figure 5.39, which indicates that carbon monoxide is present even in OCV. Besides, in fuel cell mode, water and carbon dioxide mole fraction increase as current density increases while hydrogen is consumed as expected. Related to the content of carbon monoxide, in fuel cell mode, it is strongly influenced by the content of hydrogen, decreasing when hydrogen is consumed. However, in electrolysis mode, carbon monoxide composition is more influenced by the content of hydrogen and water, in this case the carbon monoxide content increases while hydrogen content increase until intersecting with the water slope, as Figure 5.39 shows; then the content of carbon monoxide starts to decrease with the decrease of water. Contrary, hydrogen is being formed in electrolysis mode while water and carbon dioxide is consumed as the magnitude of the current density increases. The species progress in the oxygen electrode is shown in Figure 5.40, where the species behave as expected, i.e, carbon dioxide and oxygen are consumed in fuel cell mode and they are formed in electrolysis mode.

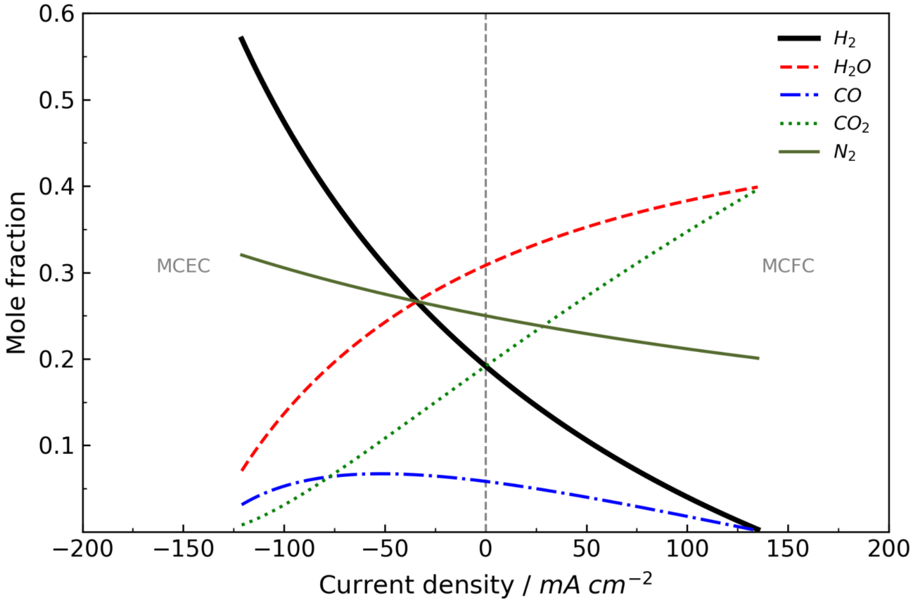

Figure 5.39. Numerical prediction of gas composition in the fuel electrode of the cell operating in reversible mode at reference condition. Fuel electrode gas composition of 25/25/25/25% $CO_2/H_2O/H_2/N_2$, oxygen electrode gas composition of 25/25/50% $CO_2/O_2/N_2$, at 650 °C.

A numerical and experimental comparison of the species in electrolysis mode at -100 mA/cm^2 working with reference composition, fuel electrode gas composition of 25/25/25/25% $CO_2/H_2O/H_2/N_2$, oxygen electrode gas composition of 25/25/50% $CO_2/O_2/N_2$, at 650 °C, is shown in Figure 5.41. The comparison is carried out using a gas mixture in a wet basis. The results indicate that the bigger difference is for water and nitrogen. The experimental water percentage is lower than the numerical, this is because to ensure a good measurement of the water, it is necessary to maintain a temperature high enough to ensure that water is entering the gas chromatographer in gas phase, otherwise, it can condensate and the measurement of water is going to be less than the one which flows out the cell. The nitrogen difference is explained because nitrogen was also used to purge the gas bags that were used to collect the gas samples in the cell, and probably some traces of nitrogen remain between samples. Anyway, water and nitrogen measurement error have almost compensated each other, which allowed to get a good correlation for the other components.

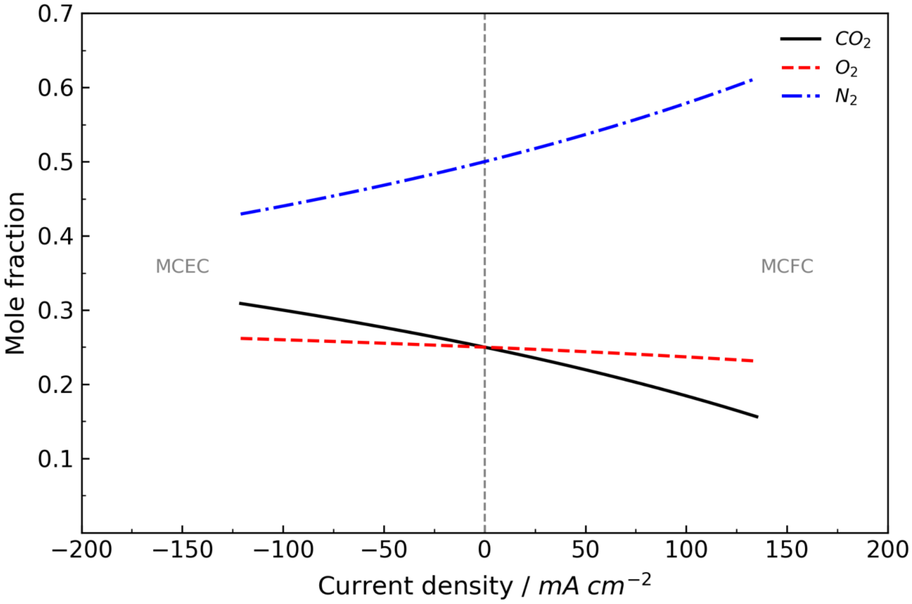

Figure 5.40. Numerical prediction of gas composition in the oxygen electrode of the cell operating in reversible mode at reference condition. Fuel electrode gas composition of 25/25/25/25% $CO_2/H_2O/H_2/N_2$, oxygen electrode gas composition of 25/25/50% $CO_2/O_2/N_2$, at 650 °C.

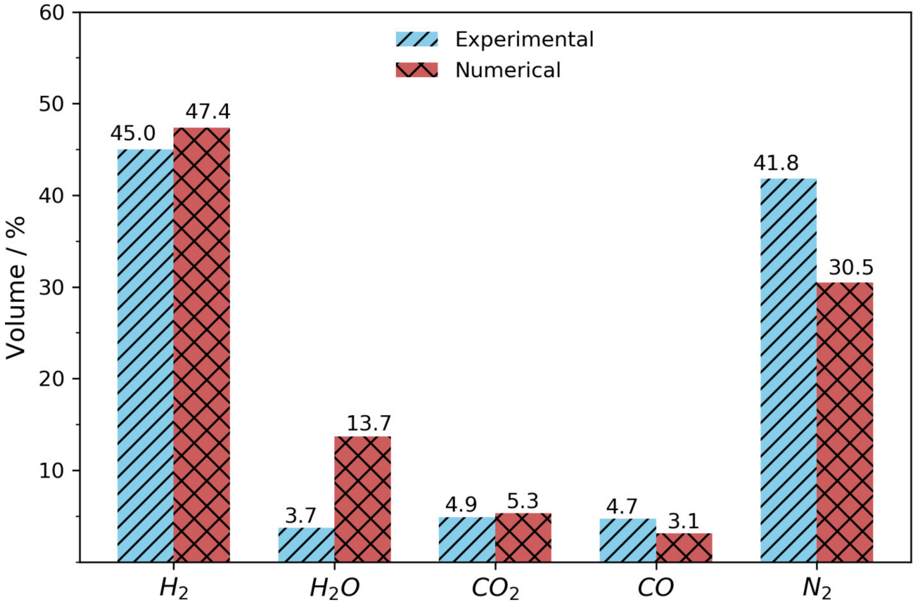

Figure 5.41. Experimental and numerical gas composition comparison in electrolysis mode at reference condition: MCEC wet basis gas composition at $-100\,\mathrm{mA/cm^2}$.

Finally, Table 5.4 shows some numerical results including hydrogen production, composition flowing out the fuel electrode, power consumption, current density and magnitude of the thermo-neutral voltage for every run of the second experimental campaign (Table 3.3,n order to evaluate the performance of the cell operating in electrolysis mode.

Table 5.4. Numerical hydrogen production and other conditions of the cell at the thermo-neutral condition for the cases of the cell operating in electrolysis mode, Table 3.3.

run	V $[V]$	j $[mA/cm^2]$	$\dot{W}$ $[W]$	y_{CO} [%]	y_{CO_2} [%]	y_{H_2} [%]	y_{H_2O} [%]	y_{N_2} [%]	$\dot{m}_{H_2,prod}$ $[kg/s] \times 10^{-8}$
1	1.208	−116.02	−11.22	3.8	1.2	54.5	8.8	31.7	8.322
2	1.211	−116.42	−11.28	3.7	1.2	54.7	8.7	31.7	8.374
3	1.212	−116.58	−11.30	3.7	1.2	54.8	8.6	31.7	8.395
4	1.213	−116.66	−11.32	3.7	1.2	54.8	8.6	31.7	8.406
5	1.221	−133.15	−13.01	6.2	1.6	58.6	7.3	26.4	8.974
6	1.243	−162.35	−16.15	12.5	2.5	64.6	6.2	14.2	9.499
7	1.265	−187.90	−19.01	20.3	3.9	69.3	6.5	0.0	9.543
8	1.207	−120.11	−11.60	2.8	1.3	57.0	13.3	25.6	9.032
9	1.206	−124.77	−12.04	1.7	1.4	59.9	24.1	12.9	9.827
10	1.208	−127.65	−12.33	1.1	1.3	61.5	36.0	0.0	10.279
11	1.193	−116.37	−11.11	3.5	1.4	42.2	8.5	44.4	8.450
12	1.160	−115.39	−10.71	3.3	1.9	29.5	8.4	56.9	8.456
13	1.207	−117.27	−11.33	3.6	1.1	55.1	8.4	31.8	8.486
14	1.203	−117.99	−11.36	3.5	1.1	55.5	8.1	31.8	8.581
15	1.198	−118.42	−11.3	3.5	1.0	55.7	8.0	31.8	8.638
16	1.187	−118.33	−11.24	3.5	1.0	55.7	8.0	31.8	8.627
17	1.213	−115.48	−11.21	3.8	1.3	54.3	9.0	31.6	8.252
18	1.216	−113.79	−11.07	4.0	1.5	53.5	9.5	31.5	8.034
19	1.223	−110.24	−10.79	4.4	1.9	51.8	10.7	31.2	7.587
20	1.240	−101.13	−10.03	5.2	3.0	47.9	13.4	30.6	6.495
21	1.225	−111.36	−10.92	4.2	1.8	52.4	10.2	31.3	7.768
22	1.246	−102.55	−10.22	4.8	3.1	48.8	12.6	30.7	6.784
23	1.269	−91.06	−9.24	5.2	5.0	44.6	15.3	29.9	5.625
24	1.292	−78.39	−8.10	5.2	7.3	40.5	17.8	29.1	4.481

The results shown in Table 5.4 help to understand better the behavior of the cell operating in electrolysis mode. In the case of the thermo-neutral voltage, it is observed that it localizes around $1.22\,\mathrm{V} \pm 0.60\,\mathrm{V}$ for all the runs. For the case of the current density at the thermo-neutral point it is more related with the species content, being carbon dioxide the species that causes it to grow most significantly. This rise in the current density results in the increment of the power demanded which could cause an increment in the price of hydrogen. Related to the hydrogen production, the electrode flow ratio effect and the hydrogen content reduction in the fuel electrode do not represent a significant parameter to increase the hydrogen production. The parameters that help to increase the hydrogen production are: 1) increase in the carbon dioxide content in the fuel electrode, 2) increase in the water content in the fuel electrode, and

3) reduction in the content of carbon dioxide in the oxygen electrode, of these being the most significant the rise in the content of water in the fuel electrode. Contrary, the parameters that cause a reduction in the hydrogen production are: 1) oxygen reduction in the oxygen electrode, and 2) decrease in the cell temperature, the latter this the most penalizing.

According to Table 5.4, run 10 represents the best case of the experimental campaign. Run 10 represents a composition of 25/50/25/0% $CO_2/H_2O/H_2/N_2$, and a composition in the oxygen electrode of 25/50/25% of $O_2/N_2/CO_2$. The electricity utility to hydrogen production at the thermo-neutral condition for run 10 is 33.33 kW h/kg of H_2, i.e., 2.79 kW h/m^3 of H_2, that is in the range of published data [90, 91]. The molar flow rate of hydrogen considered in the calculation for electricity utility is the H_2 flow content in the total flow leaving the electrolyzer.

5.4. Long-term test

A long-term test was carried out in a Molten Carbonate Electrolysis Single Cell using a gas composition trying to simulate a real operating condition in order to increase the knowledge of a MCFC operating as electrolyzer. The flow rate in the fuel and oxygen electrodes was fixed to 330 mL/min and 660 mL/min, respectively, with the fuel electrode gas composition of 47.5/47.5/5% $CO_2/H_2O/H_2$, and the oxygen electrode gas composition of 20/75/5% of $O_2/N_2/CO_2$. The performance of the cell during the long-term test is presented from Figure 5.42 to Figure 5.46. The voltage evolution during the different stages is shown if Figure 5.42.

During the long-term test, three different current densities were applied to the cell, 50 mA/cm^2, 100 mA/cm^2 and 150 mA/cm^2, corresponding to the periods 0 h to 25 h, 25 h to 620 h, and 620 h to 1003 h, respectively. In the first 25 hours, a small current density of 50 mA/cm^2 was applied to the cell aiming to activate the electrochemical processes of electrolysis and stabilize thermally the cell. In the second stage of the experiment, 25 h to 620 h, the cell was operated using a current density of 100 mA/cm^2 in order to increase the utilization factor of water and carbon dioxide, from 10.67 % to 26.10 % and 27.51 % to 50.24 %, respectively, promoting a higher hydrogen production. Unfortunately, in this period a shortage of approximately 50 h occurred in the fuel supply, caused by a failure in the system and provoking a probable evaporation of the electrolyte, produced by a lack of fuel [92]. In the third stage, the current density was increased to 150 mA/cm^2 pursuing a gradual increase in the hydrogen production.

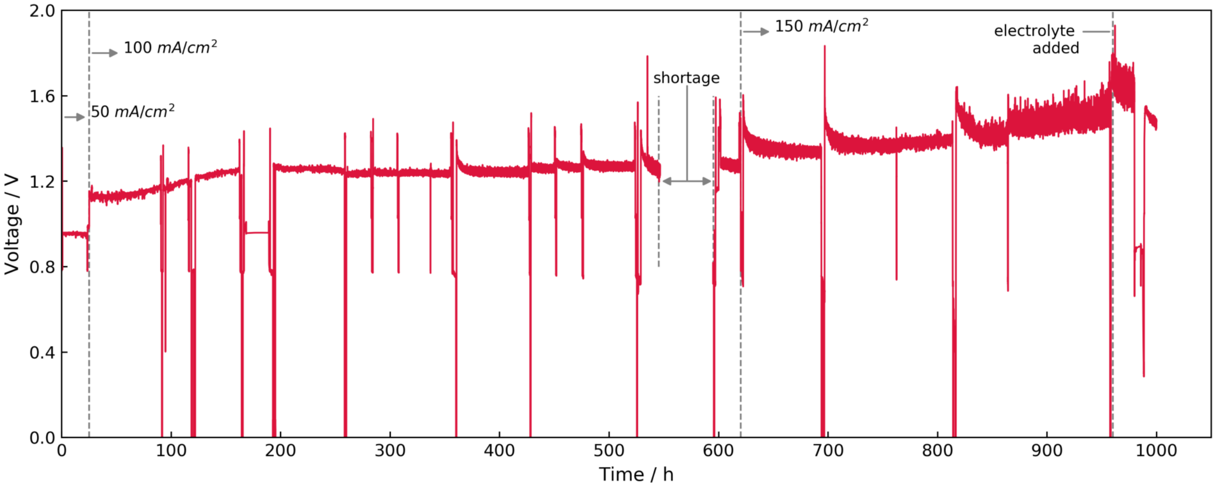

Figure 5.42. Voltage evolution during the long-term test of the single Molten Carbonate Electrolysis Cell.

Analyzing the voltage trend, during the first hours of the second period, a stabilization region is appreciated, 50 h to 350 h approximately, it could be attributed to the electrolyte distribution, defined by a rise and drop of voltage followed for a quasi-constant trend. However, after that region, the fluctuations in the voltage started to grow up [92]. This voltage fluctuations are related to a bad diffusion of the components due to loss of active sites with time. It causes an increment of water and carbon dioxide concentration in the fuel electrode provoking that species compete more to reach the diminished activated sites. In general, all of these factors increment the concentration losses. Assuming that an abnormal electrolyte evaporation caused by the shortage was reflected as an increase of electrolyte evaporation, 0.6 g of electrolyte were added in order to reduce the rise in voltage [24, 46], after that, a reduction of voltage was noticed.

It is possible to evaluate the voltage increase rate of the cell, from the period after the stabilization until before the shortage, corresponding for 200 h to 500 h. The resulting voltage increase rate is 0.043 mV/h for the single cell operating in electrolysis mode. Hu et al. [46] performed a durability test of a button cell operating in MCEC mode obtaining a cell voltage increase rate of 0.2 mV/h to 0.6 mV/h, which is almost ten times higher than the one obtained with a single cell. Moreover, Morita et al. [24] carried out a long-term stack operation working in fuel cell mode, obtaining a voltage decay rate of 0.003 mV/h, that is almost ten times lower than the one obtained in single cell.

Figure 5.43 shows the Electrochemical Impedance Spectra (EIS) evolution of the single cell during the long-term test. The EIS shows an increment of the internal resistance, i.e. the intersection of the high frequency semi-circle with the horizontal axis, respect time. Besides, the low frequency semi-circle grows with time. Both increments are mainly atribuited to a loss of electrolyte. In the case of the internal resistance increment, it could be explained because the electrolyte loss is caused by the corrosion reaction with metallic components of the cell, and the corrosion products with high electric resistance increasing internal resistance [51]. Moreover, the electrolyte loss is also caused by vaporization and creepage [51]. The low frequency semi-circle increment is explained because the loss of electrolyte or other related phenomena as corrosion, cause a decrease of the active sites where the electrochemical reactions can occur, provoking that the concentration overpotentials grow up, phenomena related to the low frequency region [93].

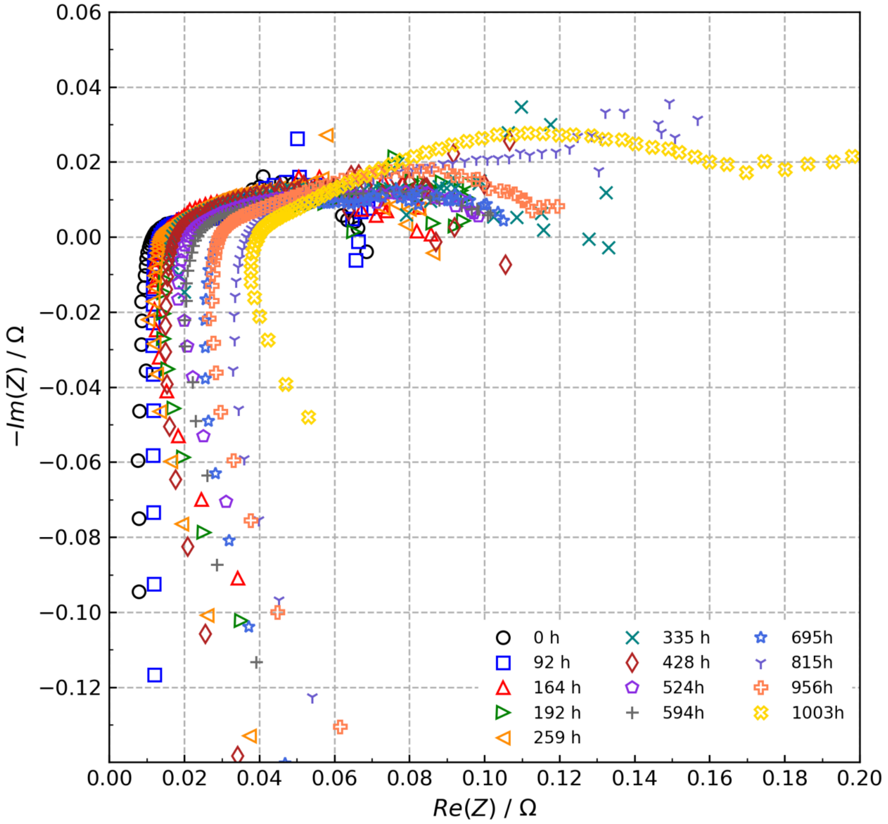

Figure 5.43. Electrochemical Impedance Spectra evolution during the long-term test of the single MCEC at open circuit voltage.

In order to appreciate better the internal resistance development, Figure 5.44 shows its evolution during the long-term test. There is an increase in the internal resistance from $1.35 \times 10^{-2}\,\Omega$ to $2.35 \times 10^{-2}\,\Omega$, corresponding to the period from 94 h to 594 h, respectively; it represents an increment of $2.01 \times 10^{-5}\,\Omega/\text{h}$ of the internal resistance. However, when the current was changed to $150\,\text{mA/cm}^2$, after the shortage, the voltage fluctuations also were increased. Moreover, the internal resistance from 594 h to 815 h grows up from $2.35 \times 10^{-2}\,\Omega$ to $3.65 \times 10^{-2}\,\Omega$, representing an increment of $5.91 \times 10^{-5}\,\Omega/\text{h}$. After the electrolyte addition, the internal resistance at 1003 h was $3.96 \times 10^{-2}\,\Omega$, comparing with 815 h, the rate of change of the internal resistance now is $1.62 \times 10^{-5}\,\Omega/\mathrm{h}$. Hence, the addition of electrolyte is useful to mitigate the increase of the internal resistance and helpful to extend the operative life of the cell operating as electrolyzer.

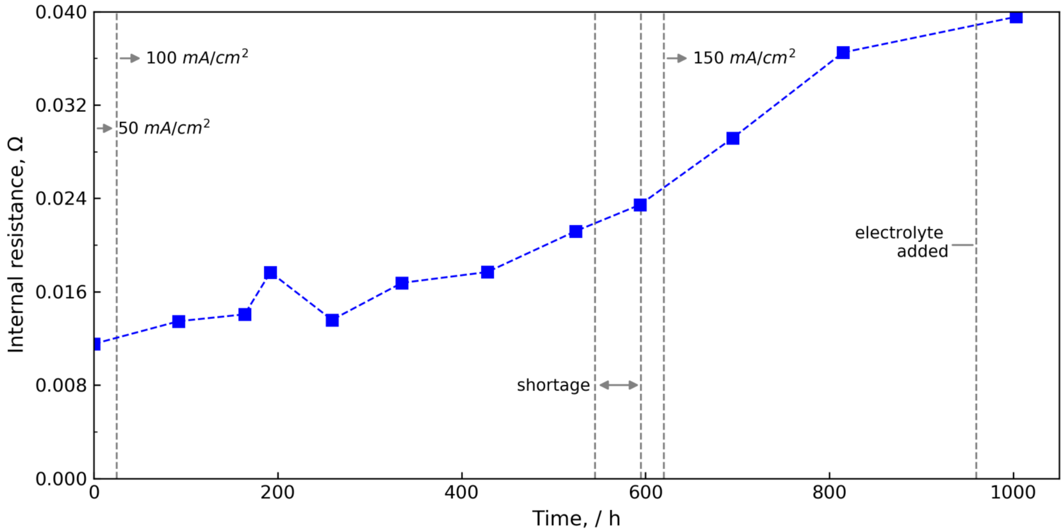

Figure 5.44. Internal resistance evolution during the long-term test.

Besides, it was observed that when fluctuations rise, the open circuit voltage decreased [24]. Figure 5.45 shows the i-V curves during the long-term test, it can be observed a gradual degradation of the cell, i.e., an increase of the cell voltage as well as an OCV drop.

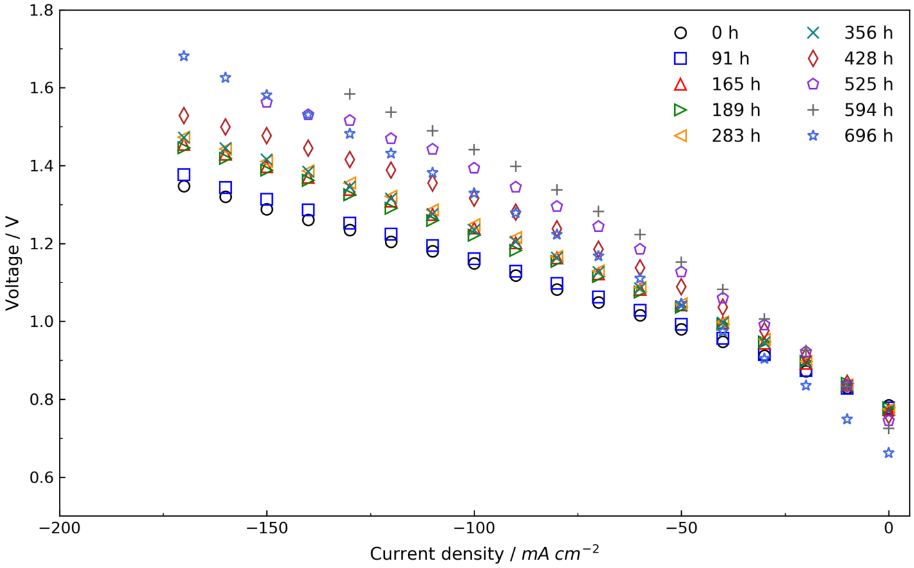

Figure 5.45. Polarization curves evolution of the MCEC during the long-term test.

Additionally, Figure 5.46 shows the voltage evolution of the different load conditions tested during the long-term test. The voltage under load condition tends to grow up, contrary to OCV that tends to diminish. The OCV decreased 47 mV during the first 620 h.

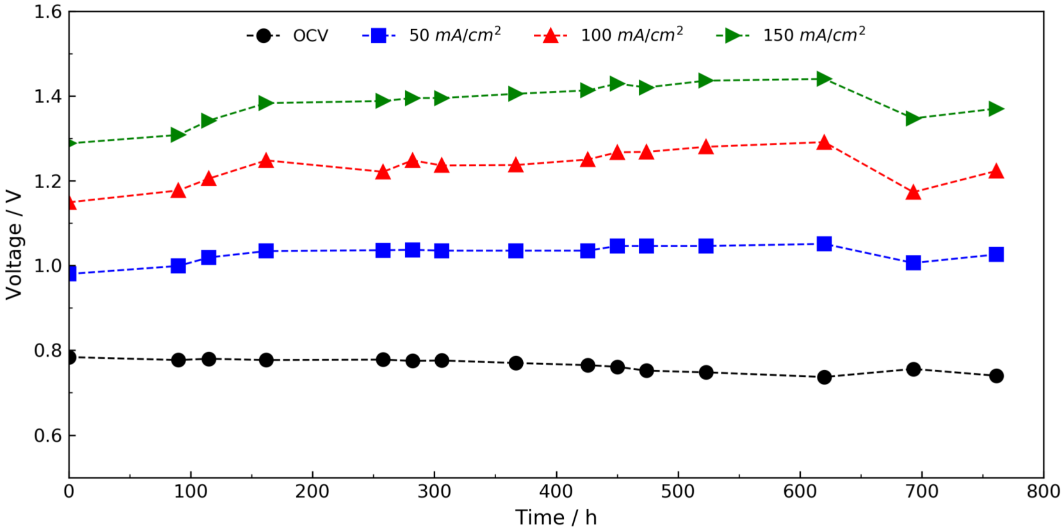

Figure 5.46. Trend in MCEC voltage at OCV, 50 mA/cm^2, 100 mA/cm^2 and 150 mA/cm^2 during the long-term test.

Figure 5.47 shows an experimental and numerical comparison of the composition flowing out the fuel electrode at -100 mA/cm^2 at the beginning of the long-term test where there is no evidence of any degradation. In general, there is a good agreement between the experimental and numerical values. The highest difference is present in the water and nitrogen as in Figure 5.41, where the error is attributed to the measurement procedure.

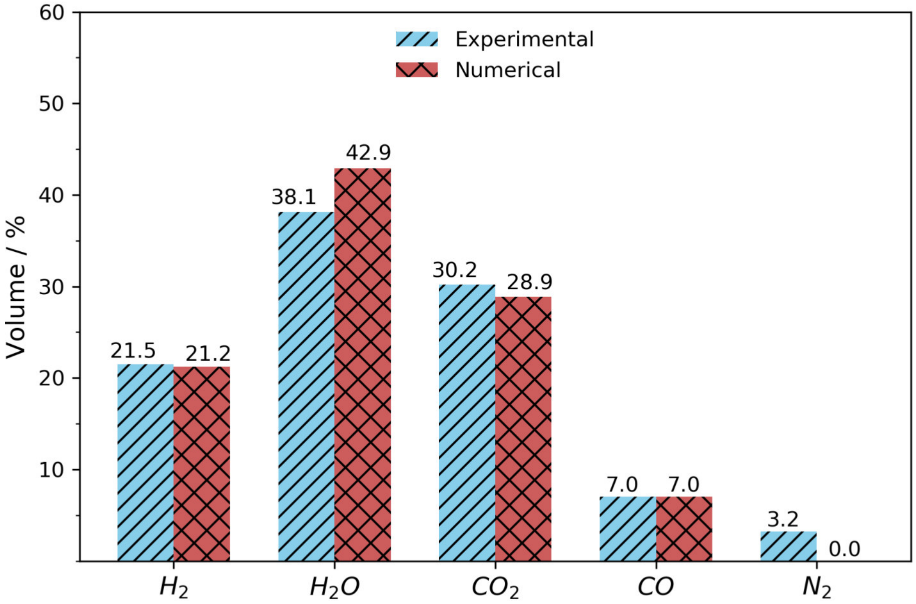

Figure 5.47. Experimental and numerical comparison of the composition flowing out the fuel electrode at -100 mA/cm^2.

6

Conclusions

6.1. Conclusions

A numerical and experimental comparison of a molten carbonate single cell has been presented in this work. Three experimental sets were carried out, the first one to validate an electrochemical model, the second one to analyze the cell working in reversible mode and the third one to validate the performance of the cell operating only as electrolyzer in a long-term test. It is the first time that a single molten carbonate cell is tested in reversible mode, i.e., fuel cell mode and electrolysis mode. Previous to this study, only works with button cells have been presented. The advantage to test single cells compared with button cells, is that single cells give a performance closer to reality due to the diffusion, heat transfer, and electrochemical phenomena that are subject to three-dimensional effects. Besides, an increase in size could cause the intensification of surface phenomena like corrosion. In general, single cells give valuable information before progressing to a prototype or industrial stage.

The first experimental campaign was carried out in order to compare the performance of the single cell operating in fuel cell mode and get data to compare numerically five zero-dimensional models used to determine the voltage losses. The parameters analyzed were the content of hydrogen in the fuel electrode, the content of carbon dioxide in the oxygen electrode and the cell temperature.

The second experimental campaign consisted in evaluating the effect of changes in composition in both electrodes, electrodes flow rate and temperature when the cell operates in reversible mode. Moreover, electrolyte refilling was carried out at the end of the experimental campaign pursuing to diminish the internal resistance. The main findings related to the experimental campaign are summarized as follows:

- In electrolysis mode the cell shows a lower polarization resistance because higher presence of hydrogen helps to decrease the overpotentials in this mode of operation, this fact can be interesting with the aim to explore new applications of this kind of cells.

- Decreasing the cell temperature increases the polarization losses in both modes, causing a lower performance.
- As in molten carbonate fuel cell, there is a limiting current density in electrolysis mode that provokes a fast increase of the overpotentials.
- Related with fuel electrode gas composition effect, it was shown that in electrolysis mode, carbon dioxide reacts with the forming hydrogen through the water gas shift reaction to produce carbon monoxide and water. The water formed through this reaction can react with remaining carbon dioxide and forming hydrogen.
- Molten Carbonate Electrolysis Cell can operate in lean hydrogen gases, contrary to Molten Carbonate Fuel Cell that requires a rich hydrogen gas to get an optimum operation, because the production of hydrogen helps to decrease the polarization overpotentials.
- Concerning the oxygen electrode gas composition effect, lower contents of carbon dioxide and oxygen cause an increase in the polarization losses in both operating modes. The most significant is the ratio between oxygen and carbon dioxide, $p_{\mathrm{O_2}}/p_{\mathrm{CO_2}}$: higher content of carbon dioxide or lower $p_{\mathrm{O_2}}/p_{\mathrm{CO_2}}$ ratio can facilitate nickel oxide dissolution in the electrode, then gradually nickel short circuiting. Hence, it is recommended to operate the molten carbonate cell with high $p_{\mathrm{O_2}}/p_{\mathrm{CO_2}}$ ratio. It is suggested to operate the electrolysis cell using a $p_{\mathrm{O_2}}/p_{\mathrm{CO_2}}$ ratio of 4, corresponding to a mixture of air with 5 % of carbon dioxide. The supplied gases to the oxygen electrode serve to remove the formed gases, thus, this proposed mixture has the objective to reduce to the minimum the carbon dioxide required in the oxygen electrode, as well as to avoid undesired overpotentials. Moreover, it is better to use the carbon dioxide in the fuel electrode to produce hydrogen or carbon monoxide instead of using it in the oxygen electrode to sweep gases.
- The cell presented a significant level of degradation in electrolysis mode, something that also was present in button cells.
- The electrolyte refilling helped to decrease the internal resistance of the cell, however, an excess of electrolyte supplied caused corrosion in the current collectors.

The third experimental campaign was carried out in order to understand better the performance of a single Molten Carbonate Electrolysis Cell operating in a long-term test using a composition trying to simulate a real condition. The results indicate that the voltage tend to increase gradually with time, as expected, however, some fluctuations in the voltage appears during the test, which were increasing also with time. Besides, EIS measurements helped to measure the increase in the internal resistance along the experimental campaign. The fluctuations in the voltage, as well as the increase in the internal resistance are mainly attributed to a loss of electrolyte. A fuel shortage in the middle of the experimental campaign caused a cell degradation increase, which was a few mitigated with electrolyte refilling. Furthermore, the voltage increase rate was measured in a period before the fuel shortage and after the cell stabilization; the voltage increase was 0.043 mV/h, which seems to indicate that voltage increase is inversely proportional to the size of the cell.

Regarding the numerical work, five zero-dimensional models were evaluated using the experimental data of the first experimental campaign. The models were compared with the experimental results at the reference condition, then Model 5 [73] was selected and fitted with the fuel cell experimental data. Once the model was fitted in fuel cell mode, it was compared with data of the second experimental campaign where the cell operates in electrolysis mode. In order to improve the fitting in electrolysis mode, some equations presented in section 4.3.1, were added to enhance the limiting current density prediction. Finally, the resulting model was used to get data as thermoneutral voltage, total amount of hydrogen produced, power utility, etc., that are difficult to get experimentally. The main results obtained from the experimental work are given below:

- The molten carbonate fuel cell models presented a high deviation from experimental data, but the best performing model was acceptable, and subsequently selected and fitted.
- It is the first time trying to predict the performance of molten carbonate electrolysis cell using a zero-dimensional model.
- The fitted model gives an acceptable correlation between the numerical and experimental data for all the runs in the fuel cell region.
- In electrolysis mode the fitted model gives a good agreement between the numerical and experimental data, predicting the tendency for all the cases. However, the error increases at higher current densities.

There are few research works related to molten carbonate electrolysis cells, however, this type of cell gives another option to the large-scale production of hydrogen or syngas, using carbon dioxide, which also represents an option for carbon capture and utilization applications.

Appendices

A

Nomenclature

Symbol	Units	Meaning
c_i^0	kmol	i^{th} component bulk concentration
c_i^*	kmol	i^{th} component catalyst layer concentration
D_{ij}	m^2/s	Binary diffusion coefficient
$D_{i,m}^{eff}$	m^2/s	i^{th} effective diffusion coefficient in the mixture
E^0	V	Standard voltage
$\mathbf{F}$	C/mol	Faraday constant, 96 485
$\bar{g}^0$	kJ/kmol	Standard specific Gibbs free energy variation for a reaction
h	kJ/kg	Specific enthalpy
I	A	Current
j	mA/cm^2	Current density
K_{eq}	Dimensionless	Chemical equilibriumEquilibrium constant
$\dot{m}$	kg/s	Mass flow rate
M	kg/kmol	Molar mass
$\dot{n}$	mol/s	Molar flow rate
n_e	Dimensionless	Number of electrons involved in the electrochemical reactions.
p	Pa	Pressure
p_{ref}	Pa	Reference atmospheric pressure
p_i	Pa	Partial pressure of the i^{th} component
P	Pa	constant for Model 5 equation
$\dot{Q}$	W	Heat transfer rate
$\dot{Q}_j$	W	Heat transfer rate associated to the ohmic heating
$\dot{Q}_{net}$	W	Net heat transfer rate
$\dot{Q}_{rxn}$	W	Heat transfer rate involved in the reaction

R	$\Omega\,\mathrm{cm}^2$	Area specific resistance
$\mathbf{R}$	kJ/(kmol K)	Universal ideal gas constant, 8.314
s	kJ/(kg K)	Specific entropy
S	kg/s	Mass source term
T	K	Temperature
V	V	Voltage
$\dot{W}$	W	Power
y	Dimensionless	Molar fraction

Greeks

Symbol	Units	Meaning
δ	m	Diffusion length
ε	Dimensionless	Porosity
η_{th}	%	Thermal efficiency
$\dot{\sigma}$	W/K	Entropy production
τ	Dimensionless	Tortuosity
υ	Dimensionless	Stoichiomnetric coefficient of the ith chemical component

Subscripts

Symbol	Meaning
act	Activation overpotential
$conc$	Concentration overpotential
CV	Control volume
$diff$	Diffusion
e	Exit
ele	Global electrochemical reaction
eq	Equilibrium condition
f	Formation
fe	Fuel electrode
i	Specie i
in	Inlet
L	Limiting point

m	Modeled
$Nernst$	Nernst voltage
oe	Oxygen electrode
ohm	Ohmic overpotential
ref	Reference condition
$RWGS$	Reversed water gas-shift reaction
SR	Steam reforming reaction
WGS	Water gas-shift reaction

Superscripts

Symbol	Meaning
e	Exit
eff	Effective
in	Inlet
r	Reacting
0	Bulk concentration
$*$	Concentration in the catalyst layer

B

Reversible Molten Carbonate Fuel Cell Code

B.1. Main program

```python
import numpy as np
import time
from scipy import constants,exp
import cantera as ct
from RMFC_functions import j_points,MCC_n_fe_OCV, MCFC_fe_WGS,E_0,E_OCV,VN_mean
from RMFC_functions import n_fuel_r,fe_reactions, fe_out,j_lim,V_ohmic
from RMFC_functions import V_act_oe,V_act_fe,V_conc ,thermal_prop
from RMFC_functions import n_th_I,n_th_II,E_th, n_real,interpolation
import matplotlib.pyplot as plt
import pandas as pd

# To start time measurement
start_time=time.process_time()

# Molar mass for every component, kg/kmol
MM_CO=28.0101
MM_CO2=44.0098
MM_CH4=16.04
MM_H2=2.0158799999999997
MM_H2O=18.015268000000003
MM_O2=31.9988
MM_N2=28.01348

MM_fe=np.array([[MM_CO],
                [MM_CO2],
                [MM_CH4],
                [MM_H2],
                [MM_H2O],
                [MM_N2]])
MM_oe=np.array([[MM_CO2],
                [MM_H2O],
                [MM_O2],
                [MM_N2]])

# ==============================================================
# DEFINING THE TOTAL NUMBER OF CURRENT DENSITY POINTS

j_min=-200
j_max=200
DeltaJ=1
j=j_points(j_min,j_max,DeltaJ)

# ==============================================================
# DEFINING OPERATIONAL CONDITIONS
# ==============================================================
Ts=273.15+20      #Temperature of the fluids leaving the reservoirs in European standard reference condition, K
Ps=101325         #Pressure of the fluids leaving the reservoirs in European standard reference condition, Pa

Tref=273.15+25  # Defining the reference conditions for the thermodynamic properties

T_op=650          # Temperature of operation, C

#---------------------------------------------------------------
# ENTERING THE FUEL ELECTRODE

# Mixture's composition expressed in the European standard, sccm

Vs_fe=330*1
Vs_CO_fe_i=Vs_fe*0
Vs_CO2_fe_i=Vs_fe*0.56
Vs_CH4_fe_i=Vs_fe*0.0
Vs_H2_fe_i=Vs_fe*0.05
Vs_H2O_fe_i=Vs_fe*0.39
Vs_N2_fe_i=Vs_fe*0.0
Vs_fe_i_comp=np.array([[Vs_CO_fe_i],
                       [Vs_CO2_fe_i],
                       [Vs_CH4_fe_i],
                       [Vs_H2_fe_i],
                       [Vs_H2O_fe_i],
                       [Vs_N2_fe_i]])

fe_comp=np.array([['CO'],
                  ['CO2'],
                  ['CH4'],
                  ['H2'],
                  ['H2O'],
                  ['N2']])

P_fe_i=101325        # Inlet pressure, Pa
T_fe_i=273.15+T_op   # Inlet temperature, K

#---------------------------------------------------------------
# ENTERING THE OXYGEN ELECTRODE
# Mixture's composition expressed in the European standard, sccm
```

```
Vs_oe=330*2
Vs_CO2_oe_i=Vs_oe*0.05
Vs_H2O_oe_i=Vs_oe*0
Vs_N2_oe_i=Vs_oe*0.75
Vs_O2_oe_i=Vs_oe*0.20
Vs_oe_i_comp=np.array([[Vs_CO2_oe_i],
                       [Vs_H2O_oe_i],
                       [Vs_N2_oe_i],
                       [Vs_O2_oe_i]])

oe_comp=np.array([['CO2'],
                  ['H2O'],
                  ['N2'],
                  ['O2']])

P_oe_i=101325       # Inlet pressure, Pa
T_oe_i=273.15+T_op  # Inlet temperature, K

# ============================================================
# CALCULATING INLET CONDITIONS
# ============================================================
# Ideal gas constant, kJ*kmol^-1 * K^-1
Ru=constants.value(R'molar gas constant')

# Convertion mL/min -> m3/s
UC1=(1e-6)/60
# Convertion Pa->kPa, J->kJ
UC2=1e-3
# Convertion cm^2 -> m^2
UC3=10000
# Convertion atm -> Pa
UC4=101325
#-------------------------------------------------------------
# ENTERING THE FUEL ELECTRODE

Vs_fe_i=np.sum(Vs_fe_i_comp)                          # Total flow rate
y_fe_i_comp=Vs_fe_i_comp/Vs_fe_i                      # Molar fraction by component
MM_fe_i=np.sum(y_fe_i_comp*MM_fe)                     # Total molar mass
n_fe_i_comp=(Vs_fe_i_comp*UC1*Ps*UC2)/(Ru*Ts)         # Molar flow rate by component
n_fe_i=np.sum(n_fe_i_comp)                            # Total molar flow rate
m_fe_i=n_fe_i*MM_fe_i                                 # Total mass flow rate
m_fe_i_comp=n_fe_i_comp*MM_fe                         # Mass flow rate by component
x_fe_i_comp=m_fe_i_comp/m_fe_i                        # Mass fraction by componenet
P_fe_i_comp=y_fe_i_comp*P_fe_i
#-------------------------------------------------------------
# ENTERING THE OXYGEN ELECTRODE

Vs_oe_i=np.sum(Vs_oe_i_comp)                          # Total flow rate
y_oe_i_comp=Vs_oe_i_comp/Vs_oe_i                      # Molar fraction by component
MM_oe_i=np.sum(y_oe_i_comp*MM_oe)                     # Total molar mass
n_oe_i_comp=(Vs_oe_i_comp*UC1*Ps*UC2)/(Ru*Ts)         # Molar flow rate by component
n_oe_i=np.sum(n_oe_i_comp)                            # Total molar flow rate
m_oe_i=n_oe_i*MM_oe_i                                 # Total mass flow rate
m_oe_i_comp=n_oe_i_comp*MM_oe                         # Mass flow rate by component
x_oe_i_comp=m_oe_i_comp/m_oe_i                        # Mass fraction by componenet
P_oe_i_comp=y_oe_i_comp*P_oe_i

# ============================================================
# CALCULATING THE OPEN CIRCUIT VOLTAGE (OCV)
# ============================================================

#-------------------------------------------------------------
# FUEL CONSUMPTION
n_e=2                                  # Electrons involved in the reaction
I_OCV=0                                # OCV current
F=constants.value(F'Faraday constant')  # Faraday constant, C/mol
Fuel_reac_OCV=I_OCV/(n_e*F*1000)        # Fuel reacting in OCV, kmol/s

#-------------------------------------------------------------
# OUTLET CONDITON
 T_fe_o=273.15+T_op                  # Outlet temperature at fuel electrode, K
 P_fe_o=P_fe_i                       # Outlet pressure at fuel electrode, Pa
 T_oe_o=273.15+T_op                  # outlet temperature at oxygen electrode, K
 P_oe_o=P_oe_i                       # Outlet pressure at oxygen electrode, Pa

# ------ FUEL ELECTRODE REACTIONS ------
# Water gas shift, CO + H2O -> CO2 + H2
# Water reduction, H2O + CO2 +2e- <-> H2 + CO3(2-)

# Entahlpies of formation, kJ/kmol
hf_CO=-110530
hf_CO2=-393520
hf_CH4=-74850
hf_H2Og=-241820
hf_H2=0
hf_O2=0
hf_N2=0

 hf_fe=np.array([[hf_CO],
                 [hf_CO2],
                 [hf_CH4],
                 [hf_H2],
                 [hf_H2Og],
                 [hf_N2]])
 hf_oe=np.array([[hf_CO2],
                 [hf_H2Og],
                 [hf_O2],
                 [hf_N2]])

 Tm_cell=np.mean([T_fe_i,T_fe_o,T_oe_i,T_oe_o])  # Mean MCC temperature
 Pm_cell=np.mean([P_fe_i,P_fe_o,P_oe_i,P_oe_o])  # Mean MCC temperature

gas= ct.Solution('gas_MCC.cti')           # Calling file of gases from cantera
#gas= ct.Solution('gri3.cti')           # Calling file of gases from cantera

CO_r = ct.Quantity(gas, constant='TP')  # Defining a quantity for CO at TP cte
CO2_r = ct.Quantity(gas, constant='TP') # Defining a quantity for CO2 at TP cte
CH4_r = ct.Quantity(gas, constant='TP') # Defining a quantity for CH4 at TP cte
H2O_r = ct.Quantity(gas, constant='TP') # Defining a quantity for H2O at TP cte
H2_r = ct.Quantity(gas, constant='TP')  # Defining a quantity for H2 at TP cte
O2_r = ct.Quantity(gas, constant='TP')  # Defining a quantity for O2 at TP cte

CO_r.TPX = Tm_cell, P_fe_i, 'CO:1'
CO2_r.TPX = Tm_cell, P_fe_i, 'CO2:1'
CH4_r.TPX = Tm_cell, P_fe_i, 'CH4:1'
H2O_r.TPX = Tm_cell, P_fe_i, 'H2O:1'
H2_r.TPX = Tm_cell, P_fe_i, 'H2:1'
O2_r.TPX = Tm_cell, P_fe_i, 'O2:1'

gCO_r=CO_r.gibbs_mole/1000       # Gibbs free energy, kJ/kmol
gCO2_r=CO2_r.gibbs_mole/1000
gCH4_r=CH4_r.gibbs_mole/1000
gH2O_r=H2O_r.gibbs_mole/1000
```

```python
gH2_r=H2_r.gibbs_mole/1000
gO2_r=O2_r.gibbs_mole/1000

# Gibbs free energy difference for water formation
DELTAG_H2O=gH2O_r-(gH2_r+0.5*gO2_r)

# Gibbs free energy difference for CO+0.5 O2 <->CO2
DELTAG_CO2=gCO2_r-(gCO_r+0.5*gO2_r)

# Gibbs free energy difference for water gas shift reaction
DELTAG_WGS=(gCO2_r+gH2_r)-(gCO_r+gH2O_r)

# Equilibrium constant for WGS
K_WGS=exp(-DELTAG_WGS/(Ru*Tm_cell))

# Calculating the amount of CO reacting
nCO_r_OCV=MCFC_fe_WGS(n_fe_i_comp,K_WGS,Fuel_reac_OCV,0)

# Fuel electrode outlet flow rate
n_fe_o_OCV_comp=MCC_n_fe_OCV(n_fe_i_comp,nCO_r_OCV,Fuel_reac_OCV)
n_fe_o_OCV=np.sum(n_fe_o_OCV_comp)

# Fuel electrode outlet composition
y_fe_o_OCV_comp=n_fe_o_OCV_comp/n_fe_o_OCV

# Oxygen electrode outlet flow rate
n_oe_o_OCV_comp=n_oe_i_comp
n_oe_o_OCV=np.sum(n_oe_o_OCV_comp)
y_oe_o_OCV_comp=y_oe_i_comp

# Gibbs free energy difference for H2+1/2 O2 -> H2O reaction
#DELTAG_H2O=gH2O_o-(gH2_o+0.5*gO2_o)
E0_H2=E_0(DELTAG_H2O,n_e)
E0_CO=E_0(DELTAG_CO2,n_e)
VN_H2=E_OCV(E0_H2,y_fe_o_OCV_comp,y_oe_o_OCV_comp,Pm_cell,Tm_cell,'MCFC')
VN_CO=E_OCV(E0_CO,y_fe_o_OCV_comp,y_oe_o_OCV_comp,Pm_cell,Tm_cell,'MCFC')
V_N=VN_mean(y_fe_o_OCV_comp,VN_H2,VN_CO)

# h[J/kmol], s[J/(kmol*K)], g [J/kmol]
h_fe_i,s_fe_i,g_fe_i=thermal_prop(V_N,T_fe_i,P_fe_i,y_fe_i_comp,'fe','MCFC')
h_oe_i,s_oe_i,g_oe_i=thermal_prop(V_N,T_oe_i,P_oe_i,y_oe_i_comp,'oe','MCFC')
E_in=n_fe_i*h_fe_i+n_fe_i*h_fe_i

# ======================================================
# CALCULATING THE OUTLET CONDITION AT ANY CURRENT DENSITY
# ======================================================

A_sys=80                        # Area of the system, cm2
I=(j/1000)*A_sys      # Current of the system, A

nH2_ox=np.zeros((len(I),1),float)
nH2O_red=np.zeros((len(I),1),float)
nCO_r=np.zeros((len(I),1),float)
n_fe_o_comp=np.zeros((len(I),len(n_fe_i_comp)),float)
n_fe_o=np.zeros((len(I),1),float)
n_oe_o_comp=np.zeros((len(I),len(n_oe_i_comp)),float)
n_oe_o=np.zeros((len(I),1),float)
y_fe_o_comp=np.zeros((len(I),len(n_fe_i_comp)),float)
Vs_fe_o_comp=np.zeros((len(I),len(n_fe_i_comp)),float)
Vs_fe_o=np.zeros((len(I),1),float)
MM_fe_o=np.zeros((len(I),1),float)
m_fe_o=np.zeros((len(I),1),float)
m_fe_o_comp=np.zeros((len(I),len(n_fe_i_comp)),float)
x_fe_o_comp=np.zeros((len(I),len(n_fe_i_comp)),float)
y_oe_o_comp=np.zeros((len(I),len(n_oe_i_comp)),float)
Vs_oe_o_comp=np.zeros((len(I),len(n_oe_i_comp)),float)
Vs_oe_o=np.zeros((len(I),1),float)
MM_oe_o=np.zeros((len(I),1),float)
m_oe_o=np.zeros((len(I),1),float)
m_oe_o_comp=np.zeros((len(I),len(n_oe_i_comp)),float)
x_oe_o_comp=np.zeros((len(I),len(n_oe_i_comp)),float)
P_fe_o_comp=np.zeros((len(I),len(n_fe_i_comp)),float)
Pm_fe_comp=np.zeros((len(I),len(n_fe_i_comp)),float)
ym_fe_comp=np.zeros((len(I),len(n_fe_i_comp)),float)
P_oe_o_comp=np.zeros((len(I),len(n_oe_i_comp)),float)
Pm_oe_comp=np.zeros((len(I),len(n_oe_i_comp)),float)
ym_oe_comp=np.zeros((len(I),len(n_oe_i_comp)),float)
j_lim_fe=np.zeros((len(I),5),float)
j_lim_oe=np.zeros((len(I),2),float)
V_ohm=np.zeros((len(I),1),float)
V_oe_act=np.zeros((len(I),1),float)
V_fe_act=np.zeros((len(I),1),float)
V_oe_con=np.zeros((len(I),1),float)
V_fe_con=np.zeros((len(I),1),float)
V=np.zeros((len(I),1),float)
h_fe_o=np.zeros((len(I),1),float)
s_fe_o=np.zeros((len(I),1),float)
g_fe_o=np.zeros((len(I),1),float)
h_oe_o=np.zeros((len(I),1),float)
s_oe_o=np.zeros((len(I),1),float)
g_oe_o=np.zeros((len(I),1),float)
W=np.zeros((len(I),1),float)
DELTAs_rxn=np.zeros((len(I),1),float)
DELTAh_rxn=np.zeros((len(I),1),float)
DELTAg_rxn=np.zeros((len(I),1),float)
Q_rxn=np.zeros((len(I),1),float)
Q_j=np.zeros((len(I),1),float)
Q_net=np.zeros((len(I),1),float)
eta_th_I=np.zeros((len(I),1),float)
eta_th_II=np.zeros((len(I),1),float)
E_out=np.zeros((len(I),1),float)
Q_loss=np.zeros((len(I),1),float)
n_WGS=np.zeros((len(I),1),float)

for k in np.arange(len(I)):
    nH2_ox[k],nH2O_red[k]=n_fuel_r(I[k],'MCFC')
    nCOr,nCO2r=fe_reactions(I[k],n_fe_i_comp,K_WGS,nH2_ox[k],nH2O_red[k],'MCFC')

    if I[k]<0:
        nCO_r[k]=-nCO2r
    elif I[k]>=0:
        nCO_r[k]=nCOr
    nCH4_r=0

    n_fe_o_comp[k,:],n_fe_o[k],n_oe_o_comp[k,:],n_oe_o[k]=fe_out(I[k],n_fe_i_comp,n_oe_i_comp,nH2_ox[k],nH2O_red[k],nCH4_r,nCO_r[k],'MCFC')

#--------------------------------------------------------------
    # FUEL ELECTRODE
    y_fe_o_comp[k,:]=n_fe_o_comp[k,:]/n_fe_o[k]                        # Molar fraction by component, -
    Vs_fe_o_comp[k,:]=(n_fe_o_comp[k,:]*Ru*Ts)/(UC1*Ps*UC2) # Molar flow rate by component, sccm
    Vs_fe_o[k]=np.sum(Vs_fe_o_comp[k,:])                                   # Total flow rate, sccm
    MM_fe_o[k]=np.matmul(y_fe_o_comp[k,:],MM_fe)                          # Total molar mass, kg/kmol
```

```
    m_fe_o[k]=n_fe_o[k]*MM_fe_o[k]                         # Total mass flow rate, kg/s
    m_fe_o_comp[k]=np.multiply(n_fe_o_comp[k,:],np.transpose(MM_fe)) # Mass flow rate by component, kg/s
    x_fe_o_comp[k,:]=m_fe_o_comp[k,:]/m_fe_o[k]             # Mass fraction by component, -
    P_fe_o_comp[k,:]=y_fe_o_comp[k,:]*P_fe_o                # Outlet pressure by component, Pa
    Pm_fe_comp[k,:]=(np.transpose(P_fe_i_comp)+P_fe_o_comp[k,:])/2 # Mean pressure by component, Pa
    ym_fe_comp[k,:]=(np.transpose(y_fe_i_comp)+y_fe_o_comp[k,:])/2 # Mean molar fraction, -

    # OXYGEN ELECTRODE
    y_oe_o_comp[k,:]=n_oe_o_comp[k,:]/n_oe_o[k]             # Molar fraction by component, -
    Vs_oe_o_comp[k,:]=(n_oe_o_comp[k,:]*Ru*Ts)/(UC1*Ps*UC2) # Molar flow rate by component, sccm
    Vs_oe_o[k]=np.sum(Vs_oe_o_comp[k,:])                    # Total flow rate by componenet, sccm
    MM_oe_o[k]=np.matmul(y_oe_o_comp[k,:],MM_oe)            # Total molar mass, kg/kmol
    m_oe_o[k]=n_oe_o[k]*MM_oe_o[k]                         # Total mass flow rate, kg/s
    m_oe_o_comp[k]=np.multiply(n_oe_o_comp[k,:],np.transpose(MM_oe)) # Mass flow rate by componenet, kg/s
    x_oe_o_comp[k,:]=m_oe_o_comp[k,:]/m_oe_o[k]             # Mass fraction by component, -
    P_oe_o_comp[k,:]=y_oe_o_comp[k,:]*P_oe_o                # Outlet pressure by componenet, Pa
    Pm_oe_comp[k,:]=(np.transpose(P_oe_i_comp)+P_oe_o_comp[k,:])/2 # Mean pressure by component, Pa
    ym_oe_comp[k,:]=(np.transpose(y_oe_i_comp)+y_oe_o_comp[k,:])/2 # Mean molar fraction, -

#--------------------------------------------------------------------
    # CALCULATING THE LIMITING CURRENT DENSITIES

    # FUEL ELECTRODE
    mpd_fe=2.7e-6                 # Mean pore diameter, m
    epsilon_fe=0.519              # Porosity
    tau_fe=2                      # Tortuosity
    L_fe=0.7e-3                   # Thikness, m

    j_lim_fe[k,:]=j_lim(Tm_cell,P_fe_i,P_fe_o_comp[k,:],y_fe_i_comp,epsilon_fe,tau_fe,L_fe,'fe','MCFC')

    # OXYGEN ELECTRODE
    mpd_oe=7.2e-6                 # Mean pore diameter, m
    epsilon_oe=0.67               # Porosity
    tau_oe=3                      # Tortuosity
    L_oe=0.9e-3                   # Thickness, m

    j_lim_oe[k,:]=j_lim(Tm_cell,P_oe_i,P_oe_o_comp[k,:],y_oe_i_comp,epsilon_oe,tau_oe,L_oe,'oe','MCFC')

#--------------------------------------------------------------------
    # CALCULATING THE VOLTAGE LOSSES
    V_ohm[k]=V_ohmic(I[k],Tm_cell,A_sys,y_fe_o_comp[k,:],y_oe_o_comp[k,:],j_lim_fe[k,:],j_lim_oe[k,:],'MCFC')
    V_oe_act[k]=V_act_oe(I[k],Tm_cell,P_oe_i,A_sys,y_fe_o_comp[k,:],y_oe_o_comp[k,:],ym_oe_comp[k,:],j_lim_fe[k,:],j_lim_oe[k,:],'MCFC')
    V_fe_act[k]=V_act_fe(I[k],Tm_cell,P_oe_i,A_sys,y_fe_o_comp[k,:],y_oe_o_comp[k,:],ym_fe_comp[k,:],j_lim_fe[k,:],j_lim_oe[k,:],'MCFC')
    V_fe_con[k],V_oe_con[k]=V_conc(I[k],Tm_cell,A_sys,y_fe_o_comp[k,:],y_oe_o_comp[k,:],j_lim_fe[k,:],j_lim_oe[k,:],'MCFC')
    V[k]=V_N-(V_ohm[k]+V_oe_act[k]+V_fe_act[k]+V_oe_con[k]+V_fe_con[k])

#--------------------------------------------------------------------
    # THERMAL ANALYSIS
    # h[J/kmol], s[J/(kmol*K)], g [J/kmol]
    h_fe_o[k],s_fe_o[k],g_fe_o[k]=thermal_prop(V[k],T_fe_o,P_fe_o,y_fe_o_comp[k,:],'fe','MCFC')
    h_oe_o[k],s_oe_o[k],g_oe_o[k]=thermal_prop(V[k],T_oe_o,P_oe_o,y_oe_o_comp[k,:],'oe','MCFC')

    W[k]=I[k]*V[k] # POWER (W) INVOLVED IN THE CELL
    # ENTROPY CHANGE RELATED TO THE REACTION, W
    DELTAs_rxn[k]=((n_oe_o[k]*s_oe_o[k]+n_fe_o[k]*s_fe_o[k])-(n_oe_i*s_oe_i+n_fe_i*s_fe_i)) # W/K
    # ENTHALPY CHANGE RELATED TO THE REACTION, W
    DELTAh_rxn[k]=((n_oe_o[k]*h_oe_o[k]+n_fe_o[k]*h_fe_o[k])-(n_oe_i*h_oe_i+n_fe_i*h_fe_i)) # W
    # GIBBS FREE ENERGY CHANGE RELATED TO THE REACTION, W
    DELTAg_rxn[k]=DELTAh_rxn[k]-T_fe_o*DELTAs_rxn[k]
    # HEAT RELATED TO THE REACTION, W
    Q_rxn[k]=T_fe_o*DELTAs_rxn[k]
   # HEAT RELATED TO THE ELECTRIC HEATING, W
    Q_j[k]=-I[k]*(V_N-V[k])
    # TOTAL HEAT RELATED TO THE PROCESSES IN THE CELL, W
    Q_net[k]=Q_rxn[k]+Q_j[k]
    # Thermal efficiency by first law, %
    eta_th_I[k]=n_th_I(I[k],V[k],W[k],DELTAh_rxn[k])
    # Thermal efficiency by second law, %
    eta_th_II[k]=n_th_II(I[k],V_N,V[k])
    # Energy flow rate at the outlet of the system, W
    E_out[k]=n_fe_o[k]*h_fe_o[k]+n_oe_o[k]*h_oe_o[k]+W[k]-Q_net[k]
    # Heat transfer rate to maintain the temperature constant
    Q_loss[k]=E_out[k]-E_in

    n_WGS[k]=n_real(V[k],nCO_r[k])

V_th,j_th=E_th(I,A_sys,V,Q_net)
m_fe_o_comp_th=interpolation(j,m_fe_o_comp,j_th)
Vs_fe_o_comp_th=interpolation(j,Vs_fe_o_comp,j_th)
W_th=interpolation(j,W,j_th)
y_fe_o_comp_th=interpolation(j,y_fe_o_comp,j_th)
m_H2_th=m_fe_o_comp_th[3]-m_fe_i_comp[3]
Vs_H2_th=Vs_fe_o_comp_th[3]-Vs_fe_i_comp[3]
Uf_CO2_th=((Vs_fe_i_comp[1]-Vs_fe_o_comp_th[1])/Vs_fe_i_comp[1])*100
Uf_H2O_th=((Vs_fe_i_comp[4]-Vs_fe_o_comp_th[4])/Vs_fe_i_comp[4])*100
W_u_m_th=W_th/(m_H2_th*3600*1000)
W_u_V_th=(W_th*100**3)/(Vs_H2_th*60*1000)
print('V_th: ',V_th, 'V')
print('j_th: ',j_th, 'mA/cm^2')
print('composition: ',y_fe_o_comp_th*100,'%')
print('Hydrogen production: ',m_H2_th, 'kg/s')
print('Hydrogen production: ',Vs_H2_th, 'sscm')
print('Power consumption: ',W_th, 'W')
print('Electricity utility: ',W_u_m_th,'kWh/kg')
print('Electricity utility: ',W_u_V_th,'kWh/m^3')
```

```
print('Utilization factor of CO2: ',Uf_CO2_th,'%')
print('Utilization factor of H2O: ',Uf_H2O_th,'%')
# ============================================================
# DRAWING SOME PLOTS
# Create a figure of size nxm inches, 100 dots per inche
fig1=plt.figure(figsize=(8,4),dpi=100)

# Create a new subplot from a grid of 1x1
ax=fig1.add_subplot(1,1,1)

marker_size=6
linewidth=2
plt.plot(j,V, linewidth=linewidth, linestyle="--", label='Fitted M5',marker='',color='b', fillstyle="full",markerfacecolor='black', markersize=marker_size,zorder=1)

xstep1=40       # Define the axis step
xmin1=j_min
xmax1=j_max

ystep1=0.1
ymin1=0.5
ymax1=1.5001

# setting limits and thicks for x-axis and y-axis
plt.xlim(xmin1,xmax1)       #set the x-axis limit
plt.xticks(np.arange(xmin1,xmax1,xstep1),fontsize=10) # set x-axis major ticks
ax.set_xticks(np.arange(xmin1,xmax1,xstep1/2),minor=True) # set x-axis minor ticks
ax.tick_params(which='major',direction='in') # put inside major ticks
ax.tick_params(which='minor',direction='in') # put inside minor ticks

plt.ylim(ymin1,ymax1)
plt.yticks(np.arange(ymin1,ymax1,ystep1),fontsize=10)
ax.set_yticks(np.arange(ymin1,ymax1,ystep1/2),minor=True)
ax.tick_params(which='major',direction='in')
ax.tick_params(which='minor',direction='in')

# setting label on x-axis and y-axis
plt.ylabel('Voltaje / $V$',fontsize=11)
plt.xlabel('Current density / $mA \cdot cm^{-2}$', fontsize=11)

# Setting the grid
plt.grid(True,which='major',linestyle='',color='lightgray')

# Adding specifications

plt.vlines(0,0,2,color='k',linestyles='dashed', linewidth=1.0) # Drawing the vertical line

# To show a legend
plt.legend(frameon=True,fontsize=8,facecolor='white',framealpha=1,edgecolor='white',loc='best')

plt.tight_layout(pad=0.1)
plt.savefig('Fig_reference_I-V.png',dpi=300)

# ============================================================

# Create a Pandas dataframe from some data.
df = pd.DataFrame({'j': [],
                   'V': [],
                   'Q_j': [],
                   'Q_rxn': [],
                   'Q_net': [],
                   'eta_th_I': [],
                   'eta_th_II': [],
                   'n_WGS': [],
                   'V_ohm': [],
                   'V_fe_act': [],
                   'V_oe_act': [],
                   'V_fe_con': [],
                  'V_oe_con': [],
                   })
for i in range(len(I)):
    df = df.append({'j': np.asscalar(j[i]),
                   'V': np.asscalar(V[i]),
                   'Q_j': np.asscalar(Q_j[i]),
                   'Q_rxn': np.asscalar(Q_rxn[i]),
                   'Q_net': np.asscalar(Q_net[i]),
                   'eta_th_I': np.asscalar(eta_th_I[i]),
                   'eta_th_II': np.asscalar(eta_th_II[i]),
                   'n_WGS': np.asscalar(n_WGS[i]),
                   'V_ohm': np.asscalar(V_ohm[i]),
                    'V_fe_act': np.asscalar(V_fe_act[i]),
                    'V_oe_act': np.asscalar(V_oe_act[i]),
                    'V_fe_con': np.asscalar(V_fe_con[i]),
                    'V_oe_con': np.asscalar(V_oe_con[i]),
                    }
                    , ignore_index=True)
# Create a Pandas Excel writer using XlsxWriter as the engine.
writer=pd.ExcelWriter('results.xlsx', engine='xlsxwriter')
# Convert the dataframe to an XlsxWriter Excel object.
df.to_excel(writer, sheet_name='MCFC-R')
# Close the Pandas Excel writer and output the Excel file.
writer.save()
# ============================================================

end_time=time.process_time()
time_taken=end_time-start_time
print('time taken= ','%.4f'%time_taken, 's')
```

B.2. Secondary functions

```python
import numpy as np
from scipy import constants,exp,log
import cantera as ct

# Molar mass for every component, kg/kmol
MM_CO=28.0101
MM_CO2=44.0098
MM_CH4=16.04
MM_H2=2.0158799999999997
MM_H2O=18.015268000000003
MM_O2=31.9988
MM_N2=28.01348

MM_fe=np.array([[MM_CO],
                [MM_CO2],
                [MM_CH4],
                [MM_H2],
                [MM_H2O],
                [MM_N2]])
MM_oe=np.array([[MM_CO2],
                [MM_H2O],
                [MM_O2],
                [MM_N2]])

# Ideal gas constant, kJ*kmol^-1 * K^-1
Ru=constants.value(R'molar gas constant')
#Faraday constant, C/mol
F=constants.value(F'Faraday constant')

# Convertion mL/min -> m3/s
UC1=(1e-6)/60
# Convertion Pa->kPa, J->kJ
UC2=1e-3
# Convertion cm^2 -> m^2
UC3=10000
# Convertion atm -> Pa
UC4=101325

# Linear interpolation function between two properties
def interpolation(prop1,prop2,value_prop1):
    # Scan for one propertie matching with one value
    for i in range(len(prop1)):
        if prop1[i]==value_prop1:
            value_prop2=prop2[i]
            break
    else:
        # Scan for the lower properties value
        for i in range(len(prop1)):
            if prop1[i]>value_prop1:
                a1=prop2[i-1]
                b1=prop1[i-1]
                break
        # Scan for the upper properties value
        for i in range(len(prop1)):
            if value_prop1<prop1[i]:
                a2=prop2[i]
                b2=prop1[i]
                break
        # Perform the linear interpolation
        value_prop2=a1+(a2-a1)*(value_prop1-b1)/(b2-b1)
    # Return the value of propertie 2 interpolated
    return value_prop2

def j_points(j_min,j_max,Deltaj):
    """This function calculates the current density matrix to be used in the solution. """
    Nj=int((j_max-j_min)/Deltaj+1)
    j=np.zeros((Nj,1),float)
    for i in range(0,Nj):
        if i==0:
            j[i]=j_min
        else:
            j[i]=j[i-1]+Deltaj
    return j

def MCFC_fe_WGS(n_fe_i_comp,K_WGS,nH2_r,nCO_ox):
    """This function calculates the amount of carbon monoxide reacting in the
    fuel electrode considering the simultaneous oxidation of hydrogen and
    carbon monoxide."""
    nCO_r=0
    nCO_fe_i=n_fe_i_comp[0]
    nCO2_fe_i=n_fe_i_comp[1]
    nH2_fe_i=n_fe_i_comp[3]
    nH2O_fe_i=n_fe_i_comp[4]

    # method for calculate the amount of carbon monoxide reacting in the WGS
    error_nCO_r=1
    error_stop=1e-20
    it=0
    it_stop=100
    while abs(error_nCO_r)>=error_stop and it<=it_stop:
        f=(nH2_fe_i-nH2_r+nCO_r)*(nCO2_fe_i+nH2_r+nCO_r+2*nCO_ox)-\
            K_WGS*(nCO_fe_i-nCO_r-nCO_ox)*(nH2O_fe_i+nH2_r-nCO_r)
        df=(nCO2_fe_i+nH2_fe_i+2*nCO_r+2*nCO_ox)+\
            K_WGS*(nH2O_fe_i+nCO_fe_i+nH2_r-2*nCO_r-nCO_ox)
        error_nCO_r=f/df
        nCO_r=nCO_r-error_nCO_r
        it+=1
    return nCO_r

def MCC_n_fe_OCV(n_fe_i,nCO_r,H2_r):
    """This function calculates the molar flow rate in the fuel electrode of a
    MCC at OCV considering that only occurs the WGS."""
    n_fe_o=np.zeros((len(n_fe_i),1),float)
    n_fe_o[0]=n_fe_i[0]-nCO_r
    n_fe_o[1]=n_fe_i[1]+nCO_r+H2_r
    n_fe_o[2]=n_fe_i[2]
    n_fe_o[3]=n_fe_i[3]-H2_r+nCO_r
    n_fe_o[4]=n_fe_i[4]+H2_r-nCO_r
    n_fe_o[5]=n_fe_o[5]
    return n_fe_o

def E_0(DELTAG,n_e):
    """This function calculates the reversible voltage given the difference of gibbs
    free energy of the reactions and the electrons involved."""
    return -DELTAG/(n_e*F)

def E_OCV(E0,y_fe_o,y_oe_o,P_cell,T_cell,cell):
    """This function calculates the OCV depending of the reactions ocurring
    in the cell."""
    Pref=101325
    yCO2_fe_o_OCV=y_fe_o[1]
    yH2_fe_o_OCV=y_fe_o[3]
    yH2O_fe_o_OCV=y_fe_o[4]

    yCO2_oe_o_OCV=y_oe_o[0]
    yO2_oe_o_OCV=y_oe_o[3]
    if cell == 'MCFC':
        n_e=2
        V_Nernst=E0-((Ru*T_cell)/(n_e*F))*(log((yH2O_fe_o_OCV*(P_cell/Pref)**(0.5))/(yH2_fe_o_OCV*yO2_oe_o_OCV**(1/2)))+log(yCO2_fe_o_OCV/yCO2_oe_o_OCV))
```

```python
    return V_Nernst

def VN_mean(y_fe_o,VN_H2O,VN_CO2):
    """This function calculates the mean Nernst voltage considering the average
    of the water oxidation and the carbon monoxide oxidation occurring at the time"""
    yCO2_fe=y_fe_o[1]
    yH2O_fe=y_fe_o[1]
    V_N=(1/(yCO2_fe+yH2O_fe))*(yH2O_fe*VN_H2O+yCO2_fe*VN_CO2)
    return V_N

def n_fuel_r(I,cell):
    """This function calculates the fuel reacting depending the operative mode. """
    if cell == 'MCC' or cell == 'MCFC' or cell == 'MCEC':
        n_e=2
        # Calculating the molar flow of the reactant, kmol/s
        if I>0:
            n_r=I/(n_e*F*1000)
            nH2_r=n_r
            nH2O_r=0
        elif I<0:
            n_r=-I/(n_e*F*1000)
            nH2_r=0
            nH2O_r=n_r
        elif I==0:
            n_r=0
            nH2_r=0
            nH2O_r=0
    return nH2_r,nH2O_r

def fe_reactions(I,n_fe_i,K_WGS,nH2_r,nH2O_r,cell):
    """This function calculates the amount of reactants in secondary reactions
    like water gas shift and steam reforming."""
    if cell == 'MCC' or cell == 'MCFC' or cell == 'MCEC':
        nCO_fe_i=n_fe_i[0]
        nCO2_fe_i=n_fe_i[1]
        nH2_fe_i=n_fe_i[3]
        nH2O_fe_i=n_fe_i[4]
        nCO_ox=0
        nCO2_red=0
        if I>=0:
            nCO_r=0
            nCO2_r=0
            for i in range(0,20):
                f=(nH2_fe_i-nH2_r+nCO_r)*(nCO2_fe_i+nH2_r+nCO_r+2*nCO_ox)- \
                    K_WGS*(nCO_fe_i-nCO_r-nCO_ox)*(nH2O_fe_i+nH2_r-nCO_r)
                df=(nCO2_fe_i+nH2_fe_i+2*nCO_r+2*nCO_ox)+ \
                    K_WGS*(nH2O_fe_i+nCO_fe_i+nH2_r-2*nCO_r-nCO_ox)
                nCO_r=nCO_r-f/df
        elif I<0:
            nCO_r=0
            nCO2_r=0
            for i in range(0,20):
                f=(nCO_fe_i+nCO2_r+nCO2_red)*(nH2O_fe_i-nH2O_r+nCO2_r)- \
                    (1/K_WGS)*(nH2_fe_i+nH2O_r-nCO2_r)*(nCO2_fe_i-nH2O_r-nCO2_r-2*nCO2_red)
                df=(nH2O_fe_i+nCO_fe_i-nH2O_r+2*nCO2_r+nCO2_red)+\
                    (1/K_WGS)*(nCO2_fe_i+nH2_fe_i-2*nCO2_r-2*nCO2_red)
                nCO2_r=nCO2_r-f/df
    return nCO_r,nCO2_r

def fe_out(I,n_fe_i,n_oe_i,nH2_r,nH2O_r,nCH4_r,nCO_r,cell):
    """This function performs the mole balance for every componenet in the
    electrodes depending of the amount of reactans."""
    if cell == 'MCC' or cell == 'MCFC' or cell == 'MCEC':
        nCO_fe_i=n_fe_i[0]
        nCO2_fe_i=n_fe_i[1]
        nCH4_fe_i=n_fe_i[2]
        nH2_fe_i=n_fe_i[3]
        nH2O_fe_i=n_fe_i[4]
        nN2_fe_i=n_fe_i[5]
        nCO_ox=0
        nCO2_red=0

        nCO2_oe_i=n_oe_i[0]
        nH2O_oe_i=n_oe_i[1]
        nN2_oe_i=n_oe_i[2]
        nO2_oe_i=n_oe_i[3]
        if I>=0:
            nCO_fe_o=nCO_fe_i-nCO_r-nCO_ox
            nCO2_fe_o=nCO2_fe_i+nH2_r+nCO_r+2*nCO_ox
            nCH4_fe_o=nCH4_fe_i-nCH4_r
            nH2_fe_o=nH2_fe_i-nH2_r+nCO_r
            nH2O_fe_o=nH2O_fe_i+nH2_r-nCO_r
            nN2_fe_o=nN2_fe_i
            n_fe_o=np.sum(n_fe_i)+nH2_r+nCO_ox

            nCO2_oe_o=nCO2_oe_i-nH2_r-nCO_ox
            nH2O_oe_o=nH2O_oe_i
            nN2_oe_o=nN2_oe_i
            nO2_oe_o=nO2_oe_i-0.5*nH2_r-0.5*nCO_ox
            n_oe_o=nCO2_oe_o+nH2O_oe_o+nN2_oe_o+nO2_oe_o
        elif I<0:
            nCO_fe_o=nCO_fe_i-nCO_r+nCO2_red
            nCO2_fe_o=nCO2_fe_i-nH2O_r+nCO_r-2*nCO2_red
            nCH4_fe_o=nCH4_fe_i-nCH4_r
            nH2_fe_o=nH2_fe_i+nH2O_r+nCO_r
            nH2O_fe_o=nH2O_fe_i-nH2O_r-nCO_r
            nN2_fe_o=nN2_fe_i
            n_fe_o=np.sum(n_fe_i)-nH2O_r+nCO2_red

            nCO2_oe_o=nCO2_oe_i+nH2O_r+nCO2_red
            nH2O_oe_o=nH2O_oe_i
            nN2_oe_o=nN2_oe_i
            nO2_oe_o=nO2_oe_i+0.5*nH2O_r+0.5*nCO2_red
            n_oe_o=nCO2_oe_o+nH2O_oe_o+nN2_oe_o+nO2_oe_o
        n_fe_comp=np.array([nCO_fe_o,nCO2_fe_o,nCH4_fe_o,nH2_fe_o,nH2O_fe_o,nN2_fe_o])
        n_oe_comp=np.array([nCO2_oe_o,nH2O_oe_o,nN2_oe_o,nO2_oe_o])
    return n_fe_comp.reshape(1,len(n_fe_i)),n_fe_o,n_oe_comp.reshape(1,len(n_oe_i)),n_oe_o

def j_lim(Tm,P_in,P_out,y_in,epsilon,tau,thickness,electrode,cell):
    """This functions determines the limiting current density for the components
    for any electrode."""
    # Fuller diffusion volume, m^3/mol
    nu_H2=6.12
    nu_H2O=13.1
    nu_CO2=26.7
    nu_CO=18
    nu_N2=18.5
    nu_O2=16.3
    nu_CH4=25.14

    if cell == 'MCC' or cell == 'MCFC' or cell == 'MCEC':
        if electrode=='fe' or electrode == 'fuel electrode':
            yCO_fe_i=y_in[0]
            yCO2_fe_i=y_in[1]
```

```
        yCH4_fe_i=y_in[2]
        yH2_fe_i=y_in[3]
        yH2O_fe_i=y_in[4]
        yN2_fe_i=y_in[5]
        n_e=2
        PCO_fe_o=P_out[0]
        PCO2_fe_o=P_out[1]
        PCH4_fe_o=P_out[2]
        PH2_fe_o=P_out[3]
        PH2O_fe_o=P_out[4]

        # ========================================
        # Binary diffusion coefficient, m^2/s
        D_H2_H2O=10*((0.001*Tm**1.75)*((MM_H2+MM_H2O)/(MM_H2*MM_H2O))**(0.5))/(((nu_H2**(1/3)+nu_H2O**(1/3))**(2))*(P_in))
        D_H2_CO2=10*((0.001*Tm**1.75)*((MM_H2+MM_CO2)/(MM_H2*MM_CO2))**(0.5))/(((nu_H2**(1/3)+nu_CO2**(1/3))**(2))*(P_in))
        D_H2_CO=10*((0.001*Tm**1.75)*((MM_H2+MM_CO)/(MM_H2*MM_CO))**(0.5))/(((nu_H2**(1/3)+nu_CO**(1/3))**(2))*(P_in))
        D_H2_N2=10*((0.001*Tm**1.75)*((MM_H2+MM_N2)/(MM_H2*MM_N2))**(0.5))/(((nu_H2**(1/3)+nu_N2**(1/3))**(2))*(P_in))
        D_H2_CH4=10*((0.001*Tm**1.75)*((MM_H2+MM_CH4)/(MM_H2*MM_CH4))**(0.5))/(((nu_H2**(1/3)+nu_CH4**(1/3))**(2))*(P_in))

        D_H2O_CO2=10*((0.001*Tm**1.75)*((MM_H2O+MM_CO2)/(MM_H2O*MM_CO2))**(0.5))/(((nu_H2O**(1/3)+nu_CO2**(1/3))**(2))*(P_in))
        D_H2O_CO=10*((0.001*Tm**1.75)*((MM_H2O+MM_CO)/(MM_H2O*MM_CO))**(0.5))/(((nu_H2O**(1/3)+nu_CO**(1/3))**(2))*(P_in))
        D_H2O_N2=10*((0.001*Tm**1.75)*((MM_H2O+MM_N2)/(MM_H2O*MM_N2))**(0.5))/(((nu_H2O**(1/3)+nu_N2**(1/3))**(2))*(P_in))
        D_H2O_CH4=10*((0.001*Tm**1.75)*((MM_H2O+MM_CH4)/(MM_H2O*MM_CH4))**(0.5))/(((nu_H2O**(1/3)+nu_CH4**(1/3))**(2))*(P_in))

        D_CO2_CO=10*((0.001*Tm**1.75)*((MM_CO2+MM_CO)/(MM_CO2*MM_CO))**(0.5))/(((nu_CO2**(1/3)+nu_CO**(1/3))**(2))*(P_in))
        D_CO2_N2=10*((0.001*Tm**1.75)*((MM_CO2+MM_N2)/(MM_CO2*MM_N2))**(0.5))/(((nu_CO2**(1/3)+nu_N2**(1/3))**(2))*(P_in))
        D_CO2_CH4=10*((0.001*Tm**1.75)*((MM_CO2+MM_CH4)/(MM_CO2*MM_CH4))**(0.5))/(((nu_CO2**(1/3)+nu_CH4**(1/3))**(2))*(P_in))

        D_CO_N2=10*((0.001*Tm**1.75)*((MM_CO+MM_N2)/(MM_CO*MM_N2))**(0.5))/(((nu_CO**(1/3)+nu_N2**(1/3))**(2))*(P_in))
        D_CO_CH4=10*((0.001*Tm**1.75)*((MM_CO+MM_CH4)/(MM_CO*MM_CH4))**(0.5))/(((nu_CO**(1/3)+nu_CH4**(1/3))**(2))*(P_in))

        # ========================================
        # Effective i-specie diffusion coefficient, m^2/s
        D_eff_CO_fe=(epsilon/tau)*((1-yCO_fe_i)/(yH2_fe_i/D_H2_CO+yH2O_fe_i/D_H2O_CO+yCO2_fe_i/D_CO2_CO+yN2_fe_i/D_CO_N2+yCH4_fe_i/D_CO_CH4))
        D_eff_CO2_fe=(epsilon/tau)*((1-yCO2_fe_i)/(yH2O_fe_i/D_H2O_CO2+yH2_fe_i/D_H2_CO2+yCO_fe_i/D_CO2_CO+yN2_fe_i/D_CO2_N2+yCH4_fe_i/D_CO2_CH4))
        D_eff_CH4_fe=(epsilon/tau)*((1-yCO2_fe_i)/(yH2O_fe_i/D_H2O_CO2+yH2_fe_i/D_H2_CO2+yCO_fe_i/D_CO2_CO+yN2_fe_i/D_CO2_N2+yCH4_fe_i/D_CO2_CH4))
        D_eff_H2_fe=(epsilon/tau)*((1-yH2_fe_i)/(yH2O_fe_i/D_H2_H2O+yCO2_fe_i/D_H2_CO2+yCO_fe_i/D_H2_CO+yN2_fe_i/D_H2_N2+yCH4_fe_i/D_H2_CH4))
        D_eff_H2O_fe=(epsilon/tau)*((1-yH2O_fe_i)/(yH2_fe_i/D_H2_H2O+yCO2_fe_i/D_H2O_CO2+yCO_fe_i/D_H2O_CO+yN2_fe_i/D_H2O_N2+yCH4_fe_i/D_H2O_CH4))

        # ========================================
        # Limiting current density for diffusion of i-specie through the fuel electrode, mA/cm^2
        j_cell_L_CO_fe=((n_e*F*D_eff_CO_fe)/(Ru*Tm*thickness))*PCO_fe_o/10
        j_cell_L_CO2_fe=((n_e*F*D_eff_CO2_fe)/(Ru*Tm*thickness))*PCO2_fe_o/10
        j_cell_L_CH4_fe=((n_e*F*D_eff_CH4_fe)/(Ru*Tm*thickness))*PCH4_fe_o/10
        j_cell_L_H2_fe=((n_e*F*D_eff_H2_fe)/(Ru*Tm*thickness))*PH2_fe_o/10
        j_cell_L_H2O_fe=((n_e*F*D_eff_H2O_fe)/(Ru*Tm*thickness))*PH2O_fe_o/10

        j_lim_comp=np.transpose(np.array([j_cell_L_CO_fe,j_cell_L_CO2_fe,j_cell_L_CH4_fe,j_cell_L_H2_fe,j_cell_L_H2O_fe]))
    if electrode=='oe' or electrode == 'oxygen electrode':
        yCO2_oe_i=y_in[0]
        yN2_oe_i=y_in[2]
        yO2_oe_i=y_in[3]
        n_e=2
        PCO2_oe_o=P_out[0]
        PO2_oe_o=P_out[3]
        # Binary diffusion coefficient, m^2/s

        D_O2_CO2=10*((0.001*Tm**1.75)*((MM_O2+MM_CO2)/(MM_O2*MM_CO2))**(0.5))/(((nu_O2**(1/3)+nu_CO2**(1/3))**(2))*(P_in))
        D_O2_N2=10*((0.001*Tm**1.75)*((MM_O2+MM_N2)/(MM_O2*MM_N2))**(0.5))/(((nu_O2**(1/3)+nu_N2**(1/3))**(2))*(P_in))
        D_CO2_N2=10*((0.001*Tm**1.75)*((MM_CO2+MM_N2)/(MM_CO2*MM_N2))**(0.5))/(((nu_CO2**(1/3)+nu_N2**(1/3))**(2))*(P_in))

        # ========================================
        # Effective i-specie diffusion factor, m^2/s
        D_eff_O2_oe=(epsilon/tau)*((1-yO2_oe_i)/(yCO2_oe_i/D_O2_CO2+yN2_oe_i/D_O2_N2))
        D_eff_CO2_oe=(epsilon/tau)*((1-yCO2_oe_i)/(yO2_oe_i/D_O2_CO2+yN2_oe_i/D_CO2_N2))
        # ========================================
        # Limiting current density for diffusion of i-specie through the oxygen electrode, mA/cm^2
        j_cell_L_CO2_oe=((n_e*F*D_eff_CO2_oe)/(Ru*Tm*thickness))*PCO2_oe_o/10
```

```
            j_cell_L_O2_oe=((2*n_e*F*D_eff_O2_oe)/(Ru*Tm*thickness))*PO2_oe_o/10
            j_lim_comp=np.transpose(np.array([j_cell_L_CO2_oe,j_cell_L_O2_oe]))

    return j_lim_comp

def V_ohmic(I,Tm,Area,y_fe_o_comp,y_oe_o_comp,j_lim_fe,j_lim_oe,cell):
    """This function determines the ohmic voltage losses in the cell. """
    j_cell_L_CO2_fe=j_lim_fe[1]
    j_cell_L_H2_fe=j_lim_fe[3]
    j_cell_L_H2O_fe=j_lim_fe[4]
    j_cell_L_CO2_oe=j_lim_oe[0]
    j_cell_L_O2_oe=j_lim_oe[1]
    yCO_fe_o=y_fe_o_comp[0]
    yCO2_fe_o=y_fe_o_comp[1]
    yH2_fe_o=y_fe_o_comp[3]
    yH2O_fe_o=y_fe_o_comp[4]
    yCO2_oe_o=y_oe_o_comp[0]
    yO2_oe_o=y_oe_o_comp[3]
    j=(I/Area)*1000
    if cell == 'MCC' or cell == 'MCFC' or cell == 'MCEC':
        if I>=0:
            if (j_cell_L_CO2_oe>=abs(j)) and (j_cell_L_O2_oe>=abs(j)) and \
                (j_cell_L_H2_fe>=abs(j)) and (j_cell_L_H2O_fe>=abs(j)) and \
                (j_cell_L_CO2_fe>=abs(j)) and (yH2_fe_o>=0) and \
                (yCO2_oe_o>=0) and (yO2_oe_o>=0):
                # ------ OHMIC LOSSES ------
                P1=0.016461/UC3
                P2=3054 # K
                R_ohm=P1*exp(P2/Tm)
                V_ohm=(R_ohm/(Area/UC3))*I
            else:
                V_ohm='NaN'
        if I<0:
            if ((abs(j_cell_L_H2_fe) and abs(j_cell_L_H2O_fe) and \
                    abs(j_cell_L_CO2_fe)) >=abs(j)) and (yCO2_fe_o>0 \
                    and yCO_fe_o>0 and yH2O_fe_o>0):
                P1=0.016461/UC3
                P2=3054 # K
                R_ohm=P1*exp(P2/Tm)
                V_ohm=(R_ohm/(Area/UC3))*I
            else:
                V_ohm='NaN'
    return V_ohm

def V_act_oe(I,Tm,P,Area,y_fe_o_comp,y_oe_o_comp,ym_oe,j_lim_fe,j_lim_oe,cell):
    """This function determines the voltage losses in the oxygen electrode. """
    j_cell_L_CO2_fe=j_lim_fe[1]
    j_cell_L_H2_fe=j_lim_fe[3]
    j_cell_L_H2O_fe=j_lim_fe[4]
    j_cell_L_CO2_oe=j_lim_oe[0]
    j_cell_L_O2_oe=j_lim_oe[1]
    yCO_fe_o=y_fe_o_comp[0]
    yCO2_fe_o=y_fe_o_comp[1]
    yH2_fe_o=y_fe_o_comp[3]
    yH2O_fe_o=y_fe_o_comp[4]
    yCO2_oe_o=y_oe_o_comp[0]
    yO2_oe_o=y_oe_o_comp[3]
    ymCO2_oe=ym_oe[0]
    ymH2O_oe=ym_oe[1]
    ymO2_oe=ym_oe[3]
    j=(I/Area)*1000
    if cell == 'MCC' or cell == 'MCFC' or cell == 'MCEC':
        if I>=0:
            if (j_cell_L_CO2_oe>=abs(j)) and (j_cell_L_O2_oe>=abs(j)) and \
                (j_cell_L_H2_fe>=abs(j)) and (j_cell_L_H2O_fe>=abs(j)) and \
                (j_cell_L_CO2_fe>=abs(j)) and (yH2_fe_o>=0) and \
                (yCO2_oe_o>=0) and (yO2_oe_o>=0):
                P3=4.891771179935e-6/UC3
                P4=2743
                upsilon=0.16
                R_oe_CO2_H2O=(P3*Tm*exp(P4/Tm))/((P/UC4)*\
                              log((1-(1.5/(1+upsilon))*(ymCO2_oe+\
                                   upsilon*ymH2O_oe))**(-1)))
                P5=9.0366282384814e-9/UC3
                P6=10036 # K
                R_oe_O2_CO2=P5*Tm*exp(P6/Tm)*((P/UC4)**(-0.25))*\
                            (ymO2_oe**(-0.75))*(ymCO2_oe**(0.5))
                R_oe=R_oe_CO2_H2O+R_oe_O2_CO2
                V_oe=(R_oe/(Area/UC3))*I
            else:
                V_oe='NaN'
        if I<0:
            if ((abs(j_cell_L_H2_fe) and abs(j_cell_L_H2O_fe) and \
                    abs(j_cell_L_CO2_fe)) >=abs(j)) and (yCO2_fe_o>0 \
                    and yCO_fe_o>0 and yH2O_fe_o>0):
                P3=4.891771179935e-6/UC3
                P4=2743
                upsilon=0.16
                R_oe_CO2_H2O=(P3*Tm*exp(P4/Tm))/((P/UC4)*\
                              log((1-(1.5/(1+upsilon))*(ymCO2_oe+\
                                   upsilon*ymH2O_oe))**(-1)))

                P5=9.0366282384814e-9/UC3
                P6=10036 # K
                R_oe_O2_CO2=P5*Tm*exp(P6/Tm)*((P/UC4)**(-0.25))*\
                            (ymO2_oe**(-0.75))*(ymCO2_oe**(0.5))
                R_oe=R_oe_CO2_H2O+R_oe_O2_CO2
                V_oe=(R_oe/(Area/UC3))*I
            else:
                V_oe='NaN'
    return V_oe

def V_act_fe(I,Tm,P,Area,y_fe_o_comp,y_oe_o_comp,ym_fe,j_lim_fe,j_lim_oe,cell):
    """This function determines the activation voltage losses in the fuel electrode. """
    j_cell_L_CO2_fe=j_lim_fe[1]
    j_cell_L_H2_fe=j_lim_fe[3]
    j_cell_L_H2O_fe=j_lim_fe[4]
    j_cell_L_CO2_oe=j_lim_oe[0]
    j_cell_L_O2_oe=j_lim_oe[1]
    yCO_fe_o=y_fe_o_comp[0]
    yCO2_fe_o=y_fe_o_comp[1]
    yH2_fe_o=y_fe_o_comp[3]
    yH2O_fe_o=y_fe_o_comp[4]
    yCO2_oe_o=y_oe_o_comp[0]
    yO2_oe_o=y_oe_o_comp[3]
    ymH2_fe=ym_fe[3]
    j=(I/Area)*1000
    if cell == 'MCC' or cell == 'MCFC' or cell == 'MCEC':
        if I>=0:
            if (j_cell_L_CO2_oe>=abs(j)) and (j_cell_L_O2_oe>=abs(j)) and \
                (j_cell_L_H2_fe>=abs(j)) and (j_cell_L_H2O_fe>=abs(j)) and \
```

```
                (j_cell_L_CO2_fe>=abs(j)) and (yH2_fe_o>=0) and \
                (yCO2_oe_o>=0) and (yO2_oe_o>=0):
                P7=4.68267140160721e-9/UC3
                P8=9362
                R_fe=(P7*Tm*exp(P8/Tm))/((P/UC4)*log(1+ymH2_fe))
                V_fe=(R_fe/(Area/UC3))*I
            else:
                V_fe='NaN'
        if I<0:
            if ((abs(j_cell_L_H2_fe) and abs(j_cell_L_H2O_fe) and \
                    abs(j_cell_L_CO2_fe)) >=abs(j)) and (yCO2_fe_o>0 \
                    and yCO_fe_o>0 and yH2O_fe_o>0):
                P7=4.68267140160721e-9/UC3
                P8=9362
                R_fe=(P7*Tm*exp(P8/Tm))/((P/UC4)*log(1+ymH2_fe))
                V_fe=(R_fe/(Area/UC3))*I
            else:
                V_fe='NaN'
    return V_fe

def V_conc(I,Tm,Area,y_fe_o_comp,y_oe_o_comp,j_lim_fe,j_lim_oe,cell):
    """This function determines the concentration voltage losses in the fuel electrode. """
    j_cell_L_CO2_fe=j_lim_fe[1]
    j_cell_L_H2_fe=j_lim_fe[3]
    j_cell_L_H2O_fe=j_lim_fe[4]
    j_cell_L_CO2_oe=j_lim_oe[0]
    j_cell_L_O2_oe=j_lim_oe[1]
    yCO_fe_o=y_fe_o_comp[0]
    yCO2_fe_o=y_fe_o_comp[1]
    yH2_fe_o=y_fe_o_comp[3]
    yH2O_fe_o=y_fe_o_comp[4]
    yCO2_oe_o=y_oe_o_comp[0]
    yO2_oe_o=y_oe_o_comp[3]
    j=(I/Area)*1000
    if cell == 'MCC' or cell == 'MCFC' or cell == 'MCEC':
        n_e=2
        if I>=0:
            if (j_cell_L_CO2_oe>=abs(j)) and (j_cell_L_O2_oe>=abs(j)) and \
                (j_cell_L_H2_fe>=abs(j)) and (j_cell_L_H2O_fe>=abs(j)) and \
                (j_cell_L_CO2_fe>=abs(j)) and (yH2_fe_o>=0) and \
                (yCO2_oe_o>=0) and (yO2_oe_o>=0):
                Vconc_fe=((Ru*Tm)/(n_e*F))*log((j_cell_L_H2_fe/(j_cell_L_H2_fe-j))*\
                         ((j_cell_L_H2O_fe-j)/j_cell_L_H2O_fe)*\
                         ((j_cell_L_CO2_fe-j)/j_cell_L_CO2_fe))

                Vconc_oe=((Ru*Tm)/(n_e*F))*log(((j_cell_L_O2_oe/(j_cell_L_O2_oe-j))**(1/2))*\
                          (j_cell_L_CO2_oe/(j_cell_L_CO2_oe-j)))
            else:
                Vconc_fe='NaN'
                Vconc_oe='NaN'
        if I<0:
            if ((abs(j_cell_L_H2_fe) and abs(j_cell_L_H2O_fe) and \
                    abs(j_cell_L_CO2_fe)) >=abs(j)) and (yCO2_fe_o>0 \
                    and yCO_fe_o>0 and yH2O_fe_o>0):
                Vconc_fe=-((Ru*Tm)/(n_e*F))*log(((abs(j_cell_L_H2_fe)-abs(j))/\
                            abs(j_cell_L_H2_fe))*(abs(j_cell_L_H2O_fe)/\
                            (abs(j_cell_L_H2O_fe)-abs(j)))*\
                            (abs(j_cell_L_CO2_fe)/(abs(j_cell_L_CO2_fe)-abs(j))))
                Vconc_oe=-((Ru*Tm)/(n_e*F))*log((((abs(j_cell_L_O2_oe)-abs(j))/(abs(j_cell_L_O2_oe)))**(1/2))*\
                            ((abs(j_cell_L_CO2_oe)-abs(j))/abs(j_cell_L_CO2_oe)))
            else:
                Vconc_fe='NaN'
                Vconc_oe='NaN'
    return Vconc_fe,Vconc_oe

def thermal_prop(V,T,P,y_o_comp,electrode,cell):
    """This function determines the enthalpy, entropy and gibbs free energy
    of the flow in molar basis."""
    gas= ct.Solution('gas_MCC.cti')          # Calling file of gases from cantera
    if cell == 'MCC' or cell == 'MCFC' or cell == 'MCEC':
        if electrode == 'fe' or electrode == 'fuel electrode':
            if np.isnan(V) != np.isnan(np.nan):
                comp='CO:'+(str(y_o_comp[0]).replace('[','')).replace(']','')+\
                        ' CO2:'+(str(y_o_comp[1]).replace('[','')).replace(']','')+\
                        ' CH4:'+(str(y_o_comp[2]).replace('[','')).replace(']','')+\
                        ' H2:'+(str(y_o_comp[3]).replace('[','')).replace(']','')+\
                        ' H2O:'+(str(y_o_comp[4]).replace('[','')).replace(']','')+\
                        ' N2:'+(str(y_o_comp[5]).replace('[','')).replace(']','')
                elec = ct.Quantity(gas, constant='TP')  # Defining a quantity for CO at TP cte
                elec.TPX = T, P, comp
                h_elec=elec.enthalpy_mole  # Gibbs free energy, J/kmol
                s_elec=elec.entropy_mole  # Gibbs free energy, J/kmol K
                g_elec=elec.gibbs_mole  # Gibbs free energy, J/kmol
            else:
                h_elec='NaN'
                s_elec='NaN'
                g_elec='NaN'
        if electrode == 'oe' or electrode == 'oxygen electrode':
            if np.isnan(V) != np.isnan(np.nan):
                comp='CO2:'+(str(y_o_comp[0]).replace('[','')).replace(']','')+\
                        ' H2O:'+(str(y_o_comp[1]).replace('[','')).replace(']','')+\
                        ' O2:'+(str(y_o_comp[2]).replace('[','')).replace(']','')+\
                        ' N2:'+(str(y_o_comp[3]).replace('[','')).replace(']','')
                elec = ct.Quantity(gas, constant='
```

```
                    TP')  # Defining a quantity for CO at TP cte
                elec.TPX = T, P, comp
                h_elec=elec.enthalpy_mole  # Gibbs free energy, J/kmol
                s_elec=elec.entropy_mole  # Gibbs free energy, J/kmol K
                g_elec=elec.gibbs_mole  # Gibbs free energy, J/kmol
            else:
                h_elec='NaN'
                s_elec='NaN'
                g_elec='NaN'
    return h_elec,s_elec,g_elec

def n_th_I(I,V,W,DELTAh_rxn):
    """This function returns the thermal efficiency by first law."""
    if I>=0:
        if np.isnan(V) != np.isnan(np.nan):
            if I==0:
                eta_th_I='NaN'
            else:
                eta_th_I=(W/abs(DELTAh_rxn))*100
        else:
            eta_th_I='NaN'
    if I<0:
        if np.isnan(V) != np.isnan(np.nan):
            if I==0:
                eta_th_I='NaN'
            else:
                eta_th_I=(DELTAh_rxn/abs(W))*100
        else:
            eta_th_I='NaN'
    return eta_th_I

def n_th_II(I,V_N,V):
    """This function returns the thermal efficiency by second law."""
    if I>=0:
        if np.isnan(V) != np.isnan(np.nan):
            eta_th_II=(V/V_N)*100
        else:
            eta_th_II='NaN'
    if I<0:
        if np.isnan(V) != np.isnan(np.nan):
            eta_th_II=(V_N/V)*100
        else:
            eta_th_II='NaN'
    return eta_th_II

def E_th(I,Area,V,Q_net):
    j=(I/Area)*1000
    j_th=interpolation(Q_net,j,0)
    if np.isnan(j_th) == np.isnan(np.nan):
        V_th='There is no thermoneutral voltage in this region.'
    if np.isnan(j_th) != np.isnan(np.nan):
        V_th=interpolation(j,V,j_th)
    return V_th,j_th

def n_real(V,n):
    if np.isnan(V) == np.isnan(np.nan):
        n_r='NaN'
    if np.isnan(V) != np.isnan(np.nan):
        n_r=n
    return n_r
```

C

List of publications

Academic production from August 2015 to August 2019.

Publications

I. Juan Pedro Perez-Trujillo, Francisco Elizalde-Blancas, Massimiliano Della Pietra, and Stephen J. McPhail. *"A numerical and experimental comparison of a single reversible molten carbonate cell operating in fuel cell mode and electrolysis mode"*. Applied Energy 226 (2018):1037-1055. https://doi.org/10.1016/j.apenergy.2018.05.121

II. Andi Mehmeti, Juan Pedro Perez-Trujillo, Francisco Elizalde-Blancas, Athanasios Angelis-Dimakis, and Stephen J. McPhail. *"Exergetic, environmental and economic sustainability assessment of stationary Molten Carbonate Fuel Cells"*. Energy Conversion and Management 168 (2018): 276-287. https://doi.org/10.1016/j.enconman.2018.04.095

III. M. Della Pietra, M. Santarelli, S. Stendardo, S. McPhail, Juan Pedro Perez-Trujillo, and Francisco Elizalde-Blancas. *"Integration of a calcium looping process (CaL) to molten carbonate fuel cells (MCFCs), as carbon concentration system: First findings"*. Journal of CO2 Utilization 25 (2018): 14-21. https://doi.org/10.1016/j.jcou.2018.03.002

IV. Juan Pedro Perez-Trujillo, Gregory J. Kowalski, and Francisco Elizalde-Blancas. *"Transient analysis of a compressed air energy storage system"*. MATTER: International Journal of Science and Technology 3, no. 2 (2017). https://dx.doi.org/10.20319/mijst.2017.32.145164

Communications

I. MS11. 11th International symposium on Molten Salts. Chemistry and Technology. *"Experimental investigation of a long-term test of a molten carbonate electrolysis single cell"*. Orleans, France. May 2019.

II. EFC17. European Fuel Cell Technology & Applications. Piero Lunghi Conference. *"Reverse operation of a single molten carbonate fuel cell: Numerical and experimental comparison"*. Naples, Italy. December 2017.

III. 18th International Conference on Researches in Science & Technology (ICRST). *"Transient analysis of a compressed air energy storage system"*. Rome, Italy. June 2017.

Bibliography

[1] R. Quadrelli and S. Peterson, "The energy–climate challenge: Recent trends in CO_2 emissions from fuel combustion," *Energy Policy*, vol. 35, no. 11, pp. 5938–5952, 2007. https://doi.org/10.1016/j.enpol.2007.07.001.

[2] CO2.earth, 2019. https://www.co2.earth/.

[3] N. Oceanic and A. A. N. N. C. for Environmental Information (NCEI), May 2019. https://www.ncdc.noaa.gov.

[4] R. Djalante, "Key assessments from the ipcc special report on global warming of 1.5° c and the implications for the sendai framework for disaster risk reduction," *Progress in Disaster Science*, vol. 1, p. 100001, 2019. https://doi.org/10.1016/j.pdisas.2019.100001.

[5] H. Mauna Loa Observatory, May 2019. http://scrippsco2.ucsd.edu/data/atmospheric_co2/mlo.

[6] C. B. Field and K. J. Mach, "Rightsizing carbon dioxide removal," *Science*, vol. 356, no. 6339, pp. 706–707, 2017. https://doi.org/10.1126/science.aam9726.

[7] J. E. Szulejko, P. Kumar, A. Deep, and K.-H. Kim, "Global warming projections to 2100 using simple CO2 greenhouse gas modeling and comments on CO2 climate sensitivity factor," *Atmospheric Pollution Research*, vol. 8, no. 1, pp. 136–140, 2017.

[8] C. interactive. Tools for a thriving future., May 2019. https://www.climateinteractive.org/programs/scoreboard/scoreboard-science-and-data/.

[9] X. Zhang, S. H. Chan, H. K. Ho, S.-C. Tan, M. Li, G. Li, J. Li, and Z. Feng, "Towards a smart energy network: The roles of fuel/electrolysis cells and technological perspectives," *International Journal of Hydrogen Energy*, vol. 40, no. 21, pp. 6866–6919, 2015. https://doi.org/10.1016/j.ijhydene.2015.03.133.

[10] J. D. Figueroa, T. Fout, S. Plasynski, H. McIlvried, and R. D. Srivastava, "Advances in CO_2 capture technology – the US Department of Energy's Carbon Sequestration Program," *International Journal of Greenhouse Gas Control*, vol. 2, no. 1, pp. 9–20, 2008. https://doi.org/10.1016/S1750-5836(07)00094-1.

[11] V. Gutknecht, S. Ó. Snæbjörnsdóttir, B. Sigfússon, E. S. Aradóttir, and L. Charles, "Creating a carbon dioxide removal solution by combining rapid mineralization of CO_2 with direct air capture," *Energy Procedia*, vol. 146, pp. 129–134, 2018. https://doi.org/10.1016/j.egypro.2018.07.017.

[12] M. Samavati, M. Santarelli, A. Martin, and V. Nemanova, "Thermodynamic and economy analysis of solid oxide electrolyser system for syngas production," *Energy*, vol. 122, pp. 37–49, 2017. https://doi.org/10.1016/j.energy.2017.01.067.

[13] X. Zhang, C. Bauer, C. L. Mutel, and K. Volkart, "Life cycle assessment of power-to-gas: Approaches, system variations and their environmental implications," *Applied Energy*, vol. 190, pp. 326–338, 2017. https://doi.org/10.1016/j.apenergy.2016.12.098.

[14] N. H. Behling, *Fuel cells: current technology challenges and future research needs.* Newnes, 2012.

[15] Office of Energy efficiency & renewable energy, May 2019. https://www.energy.gov/eere/fuelcells/comparison-fuel-cell-technologies.

[16] R. O'hayre, S.-W. Cha, F. B. Prinz, and W. Colella, *Fuel cell fundamentals.* John Wiley & Sons, 2016.

[17] S. Srinivasan, *Fuel cells: from fundamentals to applications.* Springer Science & Business media, 2006.

[18] V. S. Bagotsky, A. M. Skundin, and Y. M. Volfkovich, *Electrochemical power sources: batteries, fuel cells, and supercapacitors.* John Wiley & Sons, 2015.

[19] J. R. Selman and C.-C. Chen, "Scientific and technical maturity of molten carbonate technology," *International Journal of Hydrogen Energy*, vol. 37, no. 24, pp. 19280–19288, 2012. https://doi.org/10.1016/j.ijhydene.2012.06.016.

[20] M. Farooque, "The carbonate fuel cell – concept to reality," *Wiley Interdisciplinary Reviews: Energy and Environment*, vol. 4, no. 2, pp. 178–188, 2014. https://doi.org/10.1002/wene.124.

[21] B. Zhu, *Corrosion of current cullector materials in the molten carbonate fuel cell.* PhD thesis, Kemiteknik, 2000. urn:nbn:se:kth:diva-3031.

[22] S. Frangini, "Corrosion of structural materials in molten carbonate fuel cells: an overview," *High temperature corrosion in molten salts. Trans Tech Publications Ltd, Clausthal*, pp. 135–154, 2003.

[23] S. Randström, C. Lagergren, and P. Capobianco, "Corrosion of anode current collectors in molten carbonate fuel cells," *Journal of Power Sources*, vol. 160, no. 2, pp. 782–788, 2006. https://doi.org/10.1016/j.jpowsour.2006.04.069.

[24] H. Morita, M. Kawase, Y. Mugikura, and K. Asano, "Degradation mechanism of molten carbonate fuel cell based on long-term performance: long-term operation by using bench-scale cell and post-test analysis of the cell," *Journal of Power Sources*, vol. 195, no. 20, pp. 6988–6996, 2010. https://doi.org/10.1016/j.jpowsour.2010.04.084.

[25] M. Aneke and M. Wang, "Energy storage technologies and real life applications–a state of the art review," *Applied Energy*, vol. 179, pp. 350–377, 2016. https://doi.org/10.1016/j.apenergy.2016.06.097.

[26] M. Beaudin, H. Zareipour, A. Schellenberglabe, and W. Rosehart, "Energy storage for mitigating the variability of renewable electricity sources: An updated review," *Energy for Sustainable Development*, vol. 14, no. 4, pp. 302–314, 2010. https://doi.org/10.1016/j.esd.2010.09.007.

[27] M. Robinius, T. Raje, S. Nykamp, T. Rott, M. Müller, T. Grube, B. Katzenbach, S. Küppers, and D. Stolten, "Power-to-gas: Electrolyzers as an alternative to network expansion–an example from a distribution system operator," *Applied Energy*, vol. 210, pp. 182–197, 2018. https://doi.org/10.1016/j.apenergy.2017.10.117.

[28] B. Bensmann, R. Hanke-Rauschenbach, G. Müller-Syring, M. Henel, and K. Sundmacher, "Optimal configuration and pressure levels of electrolyzer plants in context of power-to-gas applications," *Applied Energy*, vol. 167, pp. 107–124, 2016. https://doi.org/10.1016/j.apenergy.2016.01.038.

[29] S. Marini, P. Salvi, P. Nelli, R. Pesenti, M. Villa, M. Berrettoni, G. Zangari, and Y. Kiros, "Advanced alkaline water electrolysis," *Electrochimica Acta*, vol. 82, pp. 384–391, 2012. https://doi.org/10.1016/j.electacta.2012.05.011.

[30] M. Carmo, D. L. Fritz, J. Mergel, and D. Stolten, "A comprehensive review on PEM water electrolysis," *International Journal of Hydrogen Energy*, vol. 38, no. 12, pp. 4901–4934, 2013. https://doi.org/10.1016/j.ijhydene.2013.01.151.

[31] L. Bertuccioli, A. Chan, D. Hart, F. Lehner, B. Madden, and E. Standen, "Study on development of water electrolysis in the EU," *Final report in fuel cells and hydrogen joint undertaking*, 2014.

[32] V. Menon, V. M. Janardhanan, and O. Deutschmann, "A mathematical model to analyze solid oxide electrolyzer cells (soecs) for hydrogen production," *Chemical Engineering Science*, vol. 110, pp. 83–93, 2014. https://doi.org/10.1016/j.ces.2013.10.025.

[33] D. Klotz, A. Leonide, A. Weber, and E. Ivers-Tiffée, "Electrochemical model for SOFC and SOEC mode predicting performance and efficiency," *International Journal of Hydrogen Energy*, vol. 39, no. 35, pp. 20844–20849, 2014. https://doi.org/10.1016/j.ijhydene.2014.08.139.

[34] A. Leonide, Y. Apel, and E. Ivers-Tiffee, "SOFC modeling and parameter identification by means of impedance spectroscopy," *ECS Transactions*, vol. 19, no. 20, pp. 81–109, 2009. https://doi.org/10.1149/1.3247567.

[35] D. Ferrero, A. Lanzini, P. Leone, and M. Santarelli, "Reversible operation of solid oxide cells under electrolysis and fuel cell modes: Experimental study and model validation," *Chemical Engineering Journal*, vol. 274, pp. 143–155, 2015. https://doi.org/10.1016/j.cej.2015.03.096.

[36] P. Kazempoor and R. Braun, "Hydrogen and synthetic fuel production using high temperature solid oxide electrolysis cells (SOECs)," *International Journal of Hydrogen Energy*, vol. 40, no. 9, pp. 3599–3612, 2015. https://doi.org/10.1016/j.ijhydene.2014.12.126.

[37] Y. Luo, X.-y. Wu, Y. Shi, A. F. Ghoniem, and N. Cai, "Exergy analysis of an integrated solid oxide electrolysis cell-methanation reactor for renewable energy storage," *Applied Energy*, vol. 215, pp. 371–383, 2018. https://doi.org/10.1016/j.apenergy.2018.02.022.

[38] M. T. Mehran, S.-B. Yu, D.-Y. Lee, J.-E. Hong, S.-B. Lee, S.-J. Park, R.-H. Song, and T.-H. Lim, "Production of syngas from H_2O/CO_2 by high-pressure coelectrolysis in tubular solid oxide cells," *Applied Energy*, vol. 212, pp. 759–770, 2018. https://doi.org/10.1016/j.apenergy.2017.12.078.

[39] S. Campanari, G. Manzolini, and P. Chiesa, "Using MCFC for high efficiency CO_2 capture from natural gas combined cycles: comparison of internal and external reforming," *Applied Energy*, vol. 112, pp. 772–783, 2013. https://doi.org/10.1016/j.apenergy.2013.01.045.

[40] L. Caprile, B. Passalacqua, and A. Torazza, "Carbon capture: Energy wasting technologies or the MCFCs challenge?," *International Journal of Hydrogen Energy*, vol. 36, no. 16, pp. 10269–10277, 2011. https://doi.org/10.1016/j.ijhydene.2010.10.028.

[41] M. Della Pietra, M. Santarelli, S. Stendardo, S. McPhail, J. P. Perez-Trujillo, and F. Elizalde-Blancas, "Integration of a calcium looping process (CaL) to molten carbonate fuel cells (MCFCs), as carbon concentration system: First findings," *Journal of CO2 Utilization*, vol. 25, pp. 14–21, 2018. https://doi.org/10.1016/j.jcou.2018.03.002.

[42] L. Hu, I. Rexed, G. Lindbergh, and C. Lagergren, "Electrochemical performance of Reversible Molten Carbonate Fuel Cells," *International Journal of Hydrogen Energy*, vol. 39, pp. 12323–12329, August 2014. https://doi.org/10.1016/j.ijhydene.2014.02.144.

[43] L. Hu, G. Lindbergh, and C. Lagergren, "Electrode kinetics of the Ni porous electrode for hydrogen production in a Molten Carbonate Electrolysis Cell (MCEC)," *Journal of The Electrochemical Society*, vol. 162, no. 9, pp. F1020–F1028, 2015. https://doi.org/10.1149/2.0491509jes.

[44] L. Hu, G. Lindbergh, and C. Lagergren, "Electrode kinetics of the NiO porous electrode for oxygen production in the Molten Carbonate Electrolysis Cell (MCEC)," *Faraday Discussions*, vol. 182, pp. 493–509, 2015. https://doi.org/10.1039/C5FD00011D.

[45] L. Hu, G. Lindbergh, and C. Lagergren, "Operating the nickel electrode with hydrogen-lean gases in the Molten Carbonate Electrolysis Cell (MCEC)," *International Journal of Hydrogen Energy*, vol. 41, no. 41, pp. 18692–18698, 2016. https://doi.org/10.1016/j.ijhydene.2016.06.037.

[46] L. Hu, G. Lindbergh, and C. Lagergren, "Performance and Durability of the Molten Carbonate Electrolysis Cell and the Reversible Molten Carbonate Fuel Cell," *The Journal of Physical Chemistry C*, vol. 120, no. 25, pp. 13427–13433, 2016. https://doi.org/10.1021/acs.jpcc.6b04417.

[47] P. Tomczyk, "MCFC versus other fuel cells – Characteristics, technologies and prospects," *Journal of Power Sources*, vol. 160, no. 2, pp. 858–862, 2006. https://doi.org/10.1016/j.jpowsour.2006.04.071.

[48] W. Sangarunlert, S. Suhchai, and A. Nathakaranakule, "Molten carbonate fuel cell (MCFC) characteristics, technologies and economic analysis," *International Journal of Renewable Energy*, vol. 3, no. 2, pp. 39–48, 2008.

[49] M. Cassir and C. Belhomme, "Technological applications of molten salts: the case of the molten carbonate fuel cell," *Plasmas & Ions*, vol. 2, no. 1, pp. 3–15, 1999. https://doi.org/10.1016/S1288-3255(99)80006-9.

[50] L. Hu, *Molten Carbonate Fuel Cells for Electrolysis*. PhD thesis, KTH Royal Institute of Technology, 2016. http://www.diva-portal.org/smash/get/diva2:920605/FULLTEXT01.pdf.

[51] T. Watanabe, "Molten carbonate fuel cells," in *Handbook of Climate Change Mitigation* (W.-Y. Chen, J. Seiner, T. Suzuki, and M. Lackner, eds.), pp. 1729–1754, Springer, 2012. https://doi.org/10.1007/978-1-4419-7991-9_45.

[52] S. McPhail, E. Simonetti, A. Moreno, and R. Bove, "Molten carbonate fuel cells," in *Materials for Fuel Cells*, pp. 248–279, Elsevier, 2008. https://doi.org/10.1533/9781845694838.248.

[53] C.-G. Lee, "Overpotential Behavior of Carbon Monoxide Fuel in a Molten Carbonate Fuel Cell," *Fuel Cells*, vol. 12, no. 4, pp. 550–556, 2012. https://doi.org/10.1002/fuce.201100149.

[54] G. Lindbergh, M. Olivry, and M. Sparr, "Experimental investigation of the porous nickel anode in the molten carbonate fuel cell," *Journal of The Electrochemical Society*, vol. 148, no. 5, pp. A411–A417, 2001. https://doi.org/10.1149/1.1359195.

[55] M. J. Moran and H. N. Shapiro, *Fundamentals of Engineering Thermodynamics*. John Wiley & Sons, Inc., 5th ed., 2004.

[56] M. D. Lukas, K. Y. Lee, and H. Ghezel-Ayagh, "Development of a stack simulation model for control study on direct reforming molten carbonate fuel cell power plant," *IEEE Transactions on Energy Conversion*, vol. 14, no. 4, pp. 1651–1657, 1999. https://doi.org/10.1109/60.815119.

[57] T. Watanabe, “Development of Molten Carbonate Fuel Cells in Japan and at CRIEPI–Application of Li/Na electrolyte–,” *Fuel Cells*, vol. 1, no. 2, pp. 97–103, 2001. https://doi.org/10.1002/1615-6854(200107)1:2⟨97::AID-FUCE97⟩3.0.CO;2-P.

[58] H. Morita, Y. Mugikura, Y. Izaki, T. Watanabe, and T. Abe, “Model of cathode reaction resistance in molten carbonate fuel cells,” *Journal of The Electrochemical Society*, vol. 145, no. 5, pp. 1511–1517, 1998. https://doi.org/10.1149/1.1838512.

[59] H. Morita, M. Komoda, Y. Mugikura, Y. Izaki, T. Watanabe, Y. Masuda, and T. Matsuyama, “Performance analysis of molten carbonate fuel cell using a Li/Na electrolyte,” *Journal of Power Sources*, vol. 112, no. 2, pp. 509–518, 2002. https://doi.org/10.1016/S0378-7753(02)00468-8.

[60] F. Yoshiba, N. Ono, Y. Izaki, T. Watanabe, and T. Abe, “Numerical analyses of the internal conditions of a molten carbonate fuel cell stack: comparison of stack performances for various gas flow types,” *Journal of Power Sources*, vol. 71, no. 1, pp. 328–336, 1998. https://doi.org/10.1016/S0378-7753(97)02727-4.

[61] F. Yoshiba, H. Morita, M. Yoshikawa, Y. Mugikura, Y. Izaki, T. Watanabe, M. Komoda, Y. Masuda, and N. Zaima, “Improvement of electricity generating performance and life expectancy of MCFC stack by applying Li/Na carbonate electrolyte: Test results and analysis of 0.44 m^2/10 kW-and 1.03 m^2/10 kW-class stack,” *Journal of Power Sources*, vol. 128, no. 2, pp. 152–164, 2004. https://doi.org/10.1016/j.jpowsour.2003.10.011.

[62] F. Yoshiba, “Kawagoe 300 kW Class MCFC/TCG Compact System: Thermal Efficiency and Endurance Test Results,” *Journal of Fuel Cell Science and Technology*, vol. 5, no. 2, p. 021010, 2008. https://doi.org/10.1115/1.2784281.

[63] C. Yuh and J. Selman, “The Polarization of Molten Carbonate Fuel Cell Electrodes I. Analysis of Steady-State Polarization Data,” *Journal of the Electrochemical Society*, vol. 138, no. 12, pp. 3642–3648, 1991. https://doi.org/10.1149/1.2085473.

[64] A. Baronci, G. Messina, S. J. McPhail, and A. Moreno, “Numerical investigation of a MCFC (Molten Carbonate Fuel Cell) system hybridized with a supercritical CO_2 Brayton cycle and compared with a bottoming Organic Rankine Cycle,” *Energy*, vol. 93, pp. 1063–1073, 2015. https://doi.org/10.1016/j.energy.2015.07.082.

[65] J. M. de Escalona, D. Sánchez, R. Chacartegui, and T. Sánchez, “A step-by-step methodology to construct a model of performance of molten carbonate fuel cells with internal reforming,” *International Journal of Hydrogen Energy*, vol. 36, no. 24, pp. 15739–15751, 2011. https://doi.org/10.1016/j.ijhydene.2011.08.094.

[66] Z. Ma, R. Venkataraman, and M. Farooque, “Fuel cells. molten carbonate fuel cells - modeling,” *Reference Module in Chemistry, Molecular Sciences and Chemical Engineering*, pp. 519–532, 2009. https://doi.org/10.1016/B978-044452745-5.00272-0.

[67] B. Bosio, P. Costamagna, and F. Parodi, “Modeling and experimentation of molten carbonate fuel cell reactors in a scale-up process,” *Chemical Engineering Science*, vol. 54, no. 13-14, pp. 2907–2916, 1999. https://doi.org/10.1016/S0009-2509(98)00414-X.

[68] E. Arato, B. Bosio, P. Costa, and F. Parodi, “Preliminary experimental and theoretical analysis of limit performance of Molten Carbonate Fuel Cells,” *Journal of Power Sources*, vol. 102, no. 1, pp. 74–81, 2001. https://doi.org/10.1016/S0378-7753(01)00797-2.

[69] B. Bosio, E. Arato, and P. Costa, “Concentration Polarisation in Heterogeneous Electrochemical Reactions: A Consistent Kinetic Evaluation and Its Application to Molten Carbonate Fuel Cells,” *Journal of Power Sources*, vol. 115, no. 2, pp. 189–193, 2003. https://doi.org/10.1016/S0378-7753(02)00729-2.

[70] J. Milewski, M. Wołowicz, A. Miller, and R. Bernat, “A reduced order model of molten carbonate fuel cell: A proposal,” *International Journal of Hydrogen Energy*, vol. 38, no. 26, pp. 11565–11575, 2013. https://doi.org/10.1016/j.ijhydene.2013.06.002.

[71] B. Bosio, N. Di Giulio, S. Nam, and A. Moreno, “An effective semi-empiric model for MCFC kinetics: Theoretical development and experimental parameters identification,” *International Journal of Hydrogen Energy*, vol. 39, no. 23, pp. 12273–12284, 2014. https://doi.org/10.1016/j.ijhydene.2014.04.119.

[72] E. Audasso, B. Bosio, and S. Nam, “Extension of an effective MCFC kinetic model to a wider range of operating conditions,” *International Journal of Hydrogen Energy*, vol. 41, no. 12, pp. 5571–5581, 2016. https://doi.org/10.1016/j.ijhydene.2015.10.152.

[73] E. Arato, E. Audasso, L. Barelli, B. Bosio, and G. Discepoli, “Kinetic modelling of Molten Carbonate Fuel Cells: Effects of cathode water and electrode materials,” *Journal of Power Sources*, vol. 330, pp. 18–27, 2016. https://doi.org/10.1016/j.jpowsour.2016.08.123.

[74] E. Audasso, L. Barelli, G. Bidini, B. Bosio, and G. Discepoli, “Molten carbonate fuel cell performance analysis varying cathode operating conditions for carbon capture applications,” *Journal of Power Sources*, vol. 348, pp. 118–129, 2017. https://doi.org/10.1016/j.jpowsour.2017.02.081.

[75] D. P. Massimiliano, *An innovative application for Molten Carbonate Fuel Cell (MCFC)*. PhD thesis, Universita’ degli studi di Perugia, 2015.

[76] C.-G. Lee, B.-S. Kang, H.-K. Seo, and H.-C. Lim, “Effect of gas-phase transport in molten carbonate fuel cell,” *Journal of Electroanalytical Chemistry*, vol. 540, pp. 169–188, 2003. https://doi.org/10.1016/S0022-0728(02)01304-9.

[77] C.-W. Lee, M. Lee, M.-J. Lee, S.-C. Chang, S.-P. Yoon, H. C. Ham, and J. Han, “Effect of the flow directions on a 100 cm^2 MCFC single cell with internal flow channels,” *International Journal of Hydrogen Energy*, vol. 41, no. 41, pp. 18747–18760, 2016. https://doi.org/10.1016/j.ijhydene.2016.03.188.

[78] J. P. Perez-Trujillo, F. Elizalde-Blancas, M. Della Pietra, and S. J. McPhail, "A numerical and experimental comparison of a single reversible molten carbonate cell operating in fuel cell mode and electrolysis mode," *Applied Energy*, vol. 226, pp. 1037–1055, 2018. https://doi.org/10.1016/j.apenergy.2018.05.121.

[79] S. Chan, H. Ho, and Y. Tian, "Modelling of simple hybrid solid oxide fuel cell and gas turbine power plant," *Journal of Power Sources*, vol. 109, no. 1, pp. 111–120, 2002. https://doi.org/10.1016/S0378-7753(02)00051-4.

[80] A. F. Massardo and F. Lubelli, "Internal Reforming Solid Oxide Fuel Cell-Gas Turbine Combined Cycles (IRSOFC-GT): Part A – Cell Model and Cycle Thermodynamic Analysis," *Journal of Engineering for Gas Turbines and Power*, vol. 122, pp. 27–35, 2000. https://doi.org/10.1115/98-GT-577.

[81] M. Ramandi, P. Berg, and I. Dincer, "Three-dimensional modeling of polarization characteristics in molten carbonate fuel cells using peroxide and superoxide mechanisms," *Journal of Power Sources*, vol. 218, pp. 192–203, 2012. https://doi.org/10.1016/j.jpowsour.2012.06.062.

[82] Z. Ma, S. Blanchet, R. Venkataraman, G. Iaccarino, and P. Moin, "Mathematical modeling of an internal-reforming, carbonate fuel cell stack," in *ASME 2004 2nd International Conference on Fuel Cell Science, Engineering and Technology*, pp. 311–318, American Society of Mechanical Engineers, 2004. https://doi.org/10.1115/FUELCELL2004-2486.

[83] A. Mirahmadi and H. Akbari, "Numerical modeling of planar molten carbonate fuel cells," *Journal of Fuel Cell Science and Technology*, vol. 8, no. 6, p. 061007, 2011. https://doi.org/10.1115/1.4004502.

[84] D. Fairbanks and C. Wilke, "Diffusion coefficients in multicomponent gas mixtures," *Industrial & Engineering Chemistry*, vol. 42, no. 3, pp. 471–475, 1950. https://doi.org/10.1021/ie50483a022.

[85] E. L. Cussler, *Diffusion: mass transfer in fluid systems*. Cambridge university press, 2009.

[86] Ö. Aydin and H. Nakajima, "Concentration Gradient of Reactants Extending from Reaction Sites Inward Inlet Periphery of Fuel Cells," *Journal of The Electrochemical Society*, vol. 165, no. 5, pp. F365–F374, 2018. https://doi.org/10.1149/2.0871805jes.

[87] K. Wark, *Advanced thermodynamics for engineers*. McGraw-Hill, 1995.

[88] A. Bejan, *Entropy generation through heat and fluid flow*. Wiley, 1982.

[89] A. Rao, J. Maclay, and S. Samuelsen, "Efficiency of electrochemical systems," *Journal of Power Sources*, vol. 134, no. 2, pp. 181–184, 2004. https://doi.org/10.1016/j.jpowsour.2004.02.028.

[90] J. Udagawa, P. Aguiar, and N. Brandon, "Hydrogen production through steam electrolysis: Model-based steady state performance of a cathode-supported intermediate temperature solid

oxide electrolysis cell," *Journal of Power Sources*, vol. 166, no. 1, pp. 127–136, 2007. https://doi.org/10.1016/j.jpowsour.2006.12.081.

[91] S. Grigoriev, V. Porembsky, and V. Fateev, "Pure hydrogen production by pem electrolysis for hydrogen energy," *International Journal of Hydrogen Energy*, vol. 31, no. 2, pp. 171–175, 2006. https://doi.org/10.1016/j.ijhydene.2005.04.038.

[92] J. Huijsmans, G. Kraaij, R. Makkus, G. Rietveld, E. Sitters, and H. T. J. Reijers, "An analysis of endurance issues for mcfc," *Journal of Power Sources*, vol. 86, no. 1-2, pp. 117–121, 2000. https://doi.org/10.1016/S0378-7753(99)00448-6.

[93] F. Santoni, M. Della Pietra, D. Pumiglia, C. B. Muñoz, S. McPhail, V. Cigolotti, S. Nam, M. Kang, and S. Yoon, "Accurate in-operando study of molten carbonate fuel cell degradation processes-part i: Physiochemical processes individuation," *Electrochimica Acta*, vol. 291, pp. 343–352, 2018. https://doi.org/10.1016/j.electacta.2018.08.100.

Salamanca, Gto., a 11 de Septiembre del 2019.

M. en I. HERIBERTO GUTIÉRREZ MARTIN
JEFE DE LA UNIDAD DE ADMINISTRACIÓN ESCOLAR
PRESENTE.-

Por medio de la presente, se otorga autorización para proceder a los trámites de impresión, empastado de tesis y titulación al alumno(a) Juan Pedro Pérez Trujillo del ***Programa de Doctorado en*** Ingeniería Mecánica y cuyo número de ***NUA*** es: 412630 del cual soy director. El título de la tesis es: "Experimental and numerical study of molten carbonate fuel cells working in reversible mode".

Hago constar que he revisado dicho trabajo y he tenido comunicación con los sinodales asignados para la revisión de la tesis, por lo que no hay impedimento alguno para fijar la fecha de examen de titulación.

ATENTAMENTE

Francisco Elizalde Blancas
NOMBRE Y FIRMA
DIRECTOR DE TESIS
SECRETARIO

STEPHEN J. MCPHAIL
NOMBRE Y FIRMA
DIRECTOR DE TESIS

María del Rosario Galindo González
NOMBRE Y FIRMA
PRESIDENTE

MASSIMILIANO DELLA PIETRA
NOMBRE Y FIRMA
VOCAL

Sergio Cano Andrade
NOMBRE Y FIRMA
VOCAL

Dr. Alejandro Alatorre Ordaz
NOMBRE Y FIRMA
VOCAL